MECHANISTIC INSIGHTS INTO STRUCTURE-PROPERTY RELATIONSHIPS OF

DOPED METAL OXIDE NANOCRYSTALS PRODUCED FROM

A CONTINUOUS GROWTH SYNTHESIS

by

BRANDON MICHAEL CROCKETT

A DISSERTATION

Presented to the Department of Chemistry and Biochemistry
and the Graduate School of the University of Oregon
in partial fulfillment of the requirements
for the degree of
Doctor of Philosophy

March 2019

DISSERTATION APPROVAL PAGE

Student: Brandon Michael Crockett

Title: Mechanistic insights into structure-property relationships of doped metal oxide nanocrystals produced from a continuous growth synthesis.

This dissertation has been accepted and approved in partial fulfillment of the requirements for the Doctor of Philosophy degree in the Department of Chemistry and Biochemistry by:

| | |
|---|---|
| Victoria J. De Rose | Chairperson |
| Darren W. Johnson | Advisor |
| James E. Hutchison | Advisor |
| Catherine J. Page | Core Member |
| James M. Watkins | Institutional Representative |

and

| | |
|---|---|
| Janet Woodruff-Borden | Vice Provost and Dean of the Graduate School |

Original approval signatures are on file with the University of Oregon Graduate School.

Degree awarded March 2019

DISSERTATION ABSTRACT

Brandon Michael Crockett

Doctor of Philosophy

Department of Chemistry and Biochemistry

March 2019

Title:  Mechanistic Insights into Structure-Property Relationships of Doped Metal Oxide Nanocrystals Produced from a Continuous Growth Synthesis

Colloidal metal oxide nanocrystals have tremendous potential to solve some of the world's biggest problems in energy storage and harvesting, medicine, catalysis, electronics, and information technology. Colloidal metal oxide nanocrystals display unique size- and structure-dependent properties that differ from the bulk materials. The incorporation and utilization of these nanomaterials into modern technology hinges upon chemists' abilities to synthesize the nanomaterials with atomic-level precision and control over size, morphology, composition, and surface chemistry. To this end, advances in synthetic development hold the keys to providing high-performance nanomaterials to solve global problems.

This dissertation focuses on new synthetic approaches to producing doped-metal oxide nanocrystals, using a continuous growth synthesis. The synthesis allows for nanocrystals to be grown layer-by-layer at nearly the atomic level, much akin to atomic layer deposition in solid state chemistry and living polymerizations in polymer chemistry. This layer-by-layer growth allows for metal oxide nanocrystals to be synthesized with angstrom-level control over size, composition, and distribution of dopant atoms. This level of structural control has produced significant advancements in the investigations of

structure/property relationships. With $In_2O_3$ as a model system, in this dissertation nanocrystals are shown to exhibit composition-dependent optical properties, size-dependent electrical properties, and dopant distribution-dependent plasmonic properties.

This dissertation begins with a brief introduction outlining current challenges chemists face in synthesizing metal oxide nanocrystals. The advances in continuous growth synthesis developed in the Hutchison laboratory are then discussed. Additionally, the technological relevance of $In_2O_3$ (the focus material of this dissertation) is highlighted. The following chapters demonstrate new investigations only made possible through the continuous growth synthesis. First, improvements in nanocrystal composition is demonstrated, through the doping of $In_2O_3$ nanocrystals with a variety of transition metal dopant atoms, and the dopant atom incorporations are shown to be stoichiometric, and the dopants are homogenously distributed. Next, nanometer-level control over Sn-doped $In_2O_3$ is demonstrated, in order to relate thin film resistivity to nanocrystal diameter. Finally, control over radial distribution of dopants is demonstrated in Sn-doped $In_2O_3$ and highlights the striking influence the dopant distributions exhibit on the plasmonic properties of the nanocrystals.

This dissertation contains previously published and unpublished co-authored material.

CURRICULUM VITAE

NAME OF AUTHOR:  Brandon Michael Crockett

GRADUATE AND UNDERGRADUATE SCHOOLS ATTENDED:

University of Oregon, Eugene, OR
Western Washington University, Bellingham, WA

DEGREES AWARDED:

Doctor of Philosophy, Chemistry, 2019, University of Oregon
Master of Science, Chemistry, 2013, University of Oregon
Bachelor of Science, Chemistry, 2012, Western Washington University

AREAS OF SPECIAL INTEREST:

Materials Science
Inorganic Chemistry
Colloidal Nanocrystal Synthesis
	Metal Oxide Nanocrystal Synthesis
Plasmonic Nanocrystals
Nanomaterial Characterization
	Surface Characterization
Green Chemistry

PROFESSIONAL EXPERIENCE:

Graduate Research Assistant, Department of Chemistry, University of Oregon, 2013-2019

Graduate Research Extern, Cabot Microelectronics, Aurora, IL, 2017-2018

Graduate Teaching Assistant, Department of Chemistry, University of Oregon, 2013-2015

Research and Development Intern, SolarWorldUSA, Hillsboro, OR, 2012-2013

Undergraduate Research Assistant, Department of Chemistry, Western Washington University 2010-2012

GRANTS, AWARDS, AND HONORS:

American Chemical Society National Meeting Travel Award Recipient, 2018

University Innovation Fellow, National Science Foundation, Stanford, 2016

Science Communication Fellow, Oregon Museum of Science and Industry, 2014

Transitional Research Fellow, Center for Sustainable Materials Chemistry, 2013

PUBLICATIONS:

Crockett, B. M.; Jansons, A. W.; Koskela; K. M.; Johnson, D. W.; Hutchison, J. E. "*Radial Dopant Placement for Tuning Plasmonic Properties in Metal Oxide Nanocrystals*" *ACS Nano*, **2017**, *11* (8) 7719-7728.

Jansons, A. W.; Koskela, K. M.; Crockett, B. M.; Hutchison, J. E. *"Transition Metal-Doped Metal Oxide Nanocrystals: Efficient Substitutional Doping through a Continuous Growth Process*" *Chem. Mater.* **2017**, *29* (19) 8167-8176**.**

Carnes, M. E.; Knutson, C. C.; Nadarajah, A.; Jackson, M. Jr.; Oliveri, A. F.; Norelli, K. M.; Crockett, B. M.; Bauers, S. R.; Moreno-Luna, H. A.; Taber, B. N.; Pacheco, D. J.; Olson, J. Z.; Brevick, K. R.; Sheehan, C. E.; Johnson, D. W.; Boettcher, S. W. "*Electrochemical Synthesis of flat-[$Ga_{13-x}In_x(\mu_3\text{-}OH)_6(\mu\text{-}OH)_{18}(H_2O)_{24}(NO_3)_{15}$] Clusters as Aqueous Precursors for Solution-Processed Semiconductors*" *J. Mater. Chem. C.* **2014,** *2*, 8492.

ACKNOWLEDGMENTS

First, I would like to give thanks to my advisors, Dr. Darren Johnson and Dr. Jim Hutchison, for the wonderful opportunity to study under their guidance, the opportunity to learn in their laboratories, and for the mentorship to develop me into the scientist and person I have become. The breadth of chemistry, science, and life lessons learned from these two cannot be overstated. The passion they bring to their labs, the chemistry community, and attention to their students' growth is unparalleled, and it shows through the fantastic people and scientists that have come out of the labs. I'm thankful for the experience, and while many students have been blessed with wonderful mentors, few are blessed with two so exceptional.

I would like to thank my thesis committee – Dr. Vickie De Rose, Dr. Cathy Page, and Dr. James Watkins – for their guidance and critical feedback through my graduate school career. I would like to thank the rest of the chemistry and physical science faculty for keeping such personable peers and maintaining a quality of excellence and professionalism in their respective departments. I would also like to thank the Chemistry front office staff for all their help and support, they deserve more credit than can be said for all the hard work and science the department accomplishes, we would not be able to function without you. I would like to give a special thanks to Janet Macha for all her help, hard work, and support in planning, facilitating, and helping make everyone's lives a little easier every day.

I have had the honor to work with amazing scientists, co-authors, and friends, some of whom are acknowledged in throughout this dissertation, but I would like to acknowledge them here as well. I have worked closely with graduate students Brantly Fulton, Susan Cooper, Kenyon Plummer, Meredith Sharps, and Dr. Adam Jansons, who are all exemplary scientists, and also wonderful friends. I had the pleasure of working with wonderful undergraduate students, Kris Koskela and Makenna Pennel.

I would like to thank the previous members in the Hutchlab and DWJlab for their friendship and support, and providing the foundation for the labs as they are today – Dr. Ed Elliot, Dr. Zach Kennedy, Dr. Bev Smith, Dr. Brandi Baldock, Dr. Samantha Young, Dr. Blake Tresca, Dr. Kara Sherman, Dr. Kris Vonegut, Dr. Kurtis Fairley, Dr. Mary Collins, Dr. Milton Jackson, Dr. Maisha Kamunde-Devonish, Dr. David Marsh, and Dr.

To the chemistry graduate students at the U of O: there are dozens of students who have assisted me, mentored me, and had after lab beers with me over the years. It is their dedication, personalities, and friendships that make the U of O stand above in making the environment wholesome and good place to be. Thank you all.

I would like to thank my parents, Suzanne and Michael, for always being there with their unconditional love and support. I would have never made it this far without you. I would like to thank my partner, Lana, for all of her help, support, friendship, and love. She is always there for me after a hard day, and lifts me up when I am feeling down. I love you and I am always thankful for you, your love, your support, your partnership in our life's adventures and all of the adventures yet to come. I truly wouldn't be here without you.

TABLE OF CONTENTS

LIST OF FIGURES

Figure                                                            Page

LIST OF TABLES

CHAPTER I

INTRODUCTION

I am the primary and sole author to the writing of this chapter.

**Dissertation Introduction**

Over the last several decades, colloidal metal oxide nanocrystals have been proven valuable and impactful in countless transformative technologies, including, energy harvesting and storage,[1,2] catalysis,[3,4] and electronics.[5–7] Nanocrystals utilities are derived from their size- and structure-dependent properties that arise when material dimensions are constricted on the nano-scale, and their incorporation into modern technology has been made possible due to tremendous synthetic advances. As chemists develop new synthetic methods for increasing nanocrystal material quality, purity, complexity, and novelty, greater access of nanomaterials is afforded to the scientific and engineering communities. Synthetic advancement elevates the fundamental understanding of how nano-scale structure imparts material properties that differ from the bulk material, yields insight into inorganic material formation and growth processes at the atomic-level, and helps identify new applications and utilization for nanotechnology.

However, in order for nanocrystals to be properly utilized in advanced applications, chemists face several challenges related to synthesis:

1) Dimensional control – nanocrystals display size and shape dependent properties, many of which are affected by angstrom-level changes in dimension.

Nanocrystal size and shape are determined by a plethora of factors including temperature, solvent interactions, ligand-surface interactions, and surface reaction rates, and the interplay between these factors are often non-trivial and unintuitive.

2) Compositional control – nanocrystals gain extrinsic properties when impurities are deliberately incorporated into the host lattice, and theses impurities can take the form of dopants and defects. Deliberate addition of impurities is challenging, as the formation chemistry between the host and impurity atoms must be balanced to prevent phase segregation or impurity exclusion.

3) Control over the growth processes – nanocrystal size, morphology, surface chemistry, and composition are all determined during the growth phase of nanocrystal formation, therefore absolute control over the growth phase is the foundation over which control over nano-scale properties is built. Nanocrystals must be constructed akin to organic molecules, atom-by-atom with exclusive selectivity over atomic positioning in order to fully control the material properties.

These challenges present a tall order for chemists; we must discover how to simultaneously control dimension, composition, and most importantly, the chemistry that dictates the growth processes these materials undergo. Development of new methods to allow for intentional and intuitive construction of size, atomic composition, structure, and surface chemistry will allow new transformative studies to be made on structure-property relationships.

This dissertation will explore how a continuous addition synthesis to nanocrystal growth can begin to solve these challenges. The Hutchison group has made many breakthroughs in metal oxide nanocrystal synthesis following the discovery of the continuous addition approach in 2014,[8] allowing for unprecedented size and composition control and customization. The synthetic approach uses concepts borrowed from living polymerization and atomic layer deposition, where materials are built one atomic layer at a time. In this fashion, nanocrystals can be grown to a near infinite combination of size, structure, and composition,[9–13] and the approach is adaptable to many binary and tertiary metal oxides. This dissertation will focus on utilizing this synthetic approach to investigate new structure-property relationships, using metal-doped $In_2O_3$ as a model system. The rest of Chapter I gives an overview of: traditional approaches and synthetic challenges to producing metal oxide nanocrystals, the synthetic approach developed in our laboratory that allows for new breakthroughs in controlling nanocrystal growth, the material properties and technological importance of $In_2O_3$ (the material of focus for this dissertation) and overviews for the remaining chapters in the dissertation.

**Current Synthetic Approaches and Challenges for Metal Oxide Nanocrystals**

Metal oxide nanocrystals have been synthesized and studied for decades now, with hundreds of example synthetic approaches to produce nearly every possible oxide from the Periodic Table.[2,14,15] The material properties of metal oxide nanocrystals depends not only the material identity, but also upon structure,[7,16] composition,[5,17] size,[9,18] morphology,[19–21] and surface chemistry;[22,23] these additional factors are collective products of the chemistry and reaction conditions used to synthesize the nanocrystals. Therefore, in order to

manipulate nano-scale properties through structural control, it is imperative that the nanocrystal formation chemistry be well-understood, controllable, and predictable.

Despite decades of research on nanocrystal synthesis and reaction chemistry, it is still impossible to predict synthesis outcomes by simply examining the reaction mixtures and conditions, and it is not yet possible to apply principles such as retrosynthetic analysis to inform new pathways to synthetic targets. To understand the complexity of predicting the reaction products formed during a metal oxide nanocrystal synthesis, one only needs to examine the diversity of reaction mixtures. Metal oxide nanocrystals are generally synthesized[15,24,25] through high temperature reactions involving a variety of metal salt molecular precursors (such as halides, carboxylates, and acetylacetonates) along with various high boiling long-chain organic compounds (including alcohols, ketones, amines, and carboxylic acids). The reaction mixtures contain multiple components, complicating mechanistic studies, and makes it challenging to derive predictive growth behavior from experimental observations.

Reactions to produce the metal-oxygen bonds during nanocrystal formation and growth proceed through a variety of pathways including, esterification, alkyl halide elimination, ester elimination, and ether elimination.[15,25,26] These reactions are often happening simultaneously during the reaction, and have different chemical sensitivities to slight variations in synthetic protocols. These variations result in changes in nanocrystal size, composition, structure, and morphology, but the correlation between synthetic variations and changes in the nanocrystal structure are generally non-intuitive and unpredictable. Using currently established reaction pathways to deliberately control and tune nanocrystal structure is at best laborious, and at worst impossible. Full understanding

of the nanocrystal formation and growth processes requires simultaneous consideration of all aspects of the reactions occurring, including pre-nucleation reactions, nucleation, nanocrystal surface reactions during growth, and ligand-solvent interactions to maintain colloidal stability.

Metal oxide nanocrystals are often doped with impurity atoms to impart new properties and functionalities. Doped metal oxide nanocrystals have been investigated for their dopant-induced catalytic,[3,4,27] electronic,[6,28] and magnetic[9,29,30] properties. The doping of semiconductor materials is essential to the modern microelectronics industry, and is one of the fundamental approaches to altering the materials' physical and electronic structures.[31,32] However, the inclusion of dopant atoms further complicates the reaction chemistries of nanocrystal formation and growth. Nanocrystals were once considered "undopable[33]" as they were rife with phase segregation[34] and "self-purification,[35,36]" or the exclusion of impurities during crystal formation and growth.

There have been many examples of successful strategies for doping metal oxide nanocrystals[11,16,37–39], though they are often non-stoichiometric (the composition of the starting material does not trend with the resulting nanocrystal composition) and there are many instances of surface segregation. Additionally, adding dopant impurities to the reaction will influence the precursor conversion rates, nucleation, morphology, surface energies, and the resulting nanocrystal size,[35] requiring a careful balance to be struck between the reactivities of the dopant and host atoms to ameliorate reaction complications. With all of the chemical challenges presented in designing and synthesizing nanocrystalline oxide materials with intended structure, composition, and properties, it is a wonder they are successfully produced at all. There is a great need in the nanocrystal community for

reaction chemistries that are reliable, intuitive, and predictable so that the nanocrystal formation processes can be exploited to obtain materials with intended structure, composition and material properties.

**Continuous Addition Synthesis of Metal Oxide Nanocrystals Through Metal-Catalyzed Esterification.**

In 2014, our laboratory discovered[8] a new way to synthesize metal oxide nanocrystals through a simple esterification pathway between metal oleate salts and alcohol solvent, and the synthetic approach was found to be widely applicable to many metal oxide systems, including doped nanocrystals and hetero core/shell structures. The synthesis utilizes metal oleate precursor, slowly added into oleyl alcohol solvent at 230 °C, where the metal catalyzes esterification between the oleate ligands the alcohol solvent to produce condensable $M-OH_x$ species. These $M-OH_x$ species will condense to form M-O-M bonds and thus initiate nanocrystal formation. Interestingly, it was found that the nanocrystals themselves contain these reactive M-OHx species on their surfaces,[10] and these reactive sites are what drive further growth with the solution phase $M-OH_x$ species.

This approach was foundational in many ways: the reaction chemistry proceeds through a single chemical pathway, a wide variety of oxide materials can be readily produced with minimal changes to synthetic conditions, the reactive metal precursor is introduced slowly (~ 10-20 mL/h) and controllable, which allows for fine control over the nanocrystal growth phase, and the nanocrystal surfaces remain chemically active while in the reaction. Since the initial report,[8] more in depth studies have been performed on $In_2O_3$[10] and $Fe_2O_3/Fe_3O_4$.[9] Importantly it was confirmed that the syntheses proceeds through a

6

living growth mechanism,[12] much like living polymerizations, where the nanocrystals retain their reactive surfaces, and upon additional metal oleate precursor introduction the nanocrystals will continue to grow seemingly indefinitely. This aspect of the reaction allows for nanocrystal size to be tuned by adjusting the amount of metal precursor that is introduced into the reaction.

However, questions still remained regarding the compatibility of this new chemistry with regards to dopant incorporation, growth resolution, what new core/shell structures are available, and what size-dependent studies are now made possible. The work in this Dissertation focuses on $In_2O_3$ nanocrystals, and new structure-property relationships made possible through these synthetic advances, to answer many of these questions. $In_2O_3$ was chosen for study as the model system for a variety of reasons: the growth behavior of $In_2O_3$ was the best understood in the continuous addition synthesis, the $In^{3+}$ metal in the precursor does not undergo any redox changes during the reaction, and $In_2O_3$ has great technological importance as a transparent conductor[40] and plasmonic[41] material.

**$In_2O_3$ as a Transparent Conducting Oxide**

Transparent conducting oxides (TCOs) represent a special class of inorganic materials that exhibit both optical transparency and high electronic conductivity. These attributes make TCOs vital as thin film electrode materials for many modern electronic devices such as flat panel displays, touch screens, solar cells, and energy efficient windows.[40,42–46] TCO materials gain their unique optoelectronic properties through significant degeneracy in a wide band gap (2-4 eV) semiconductor. The degeneracy is generally achieved through the introduction of aliovalent dopant atoms into the

semiconductor lattice. The primary example of this is Sn-doped $In_2O_3$ (ITO), which dominates the TCO market with a 93% share.[47,48] As the $In_2O_3$ oxide lattice is doped with $Sn^{4+}$ atoms, the resulting change in net charge within the crystal lattice is neutralized by excess electrons which populate the material's conduction band. The defect model generally applied to this process includes interstitial oxygen incorporation along with the substitutional $Sn^{4+}$ incorporation.[49] This leads to the formation of a $2Sn_{In}O_i$ complex (where Sn substitutes for In). Under reducing conditions during or after lattice formation, the complex degrades as

$$2(2Sn_{In}O_i) \rightarrow O_2(g) + 4Sn_{In} + 4e^-$$
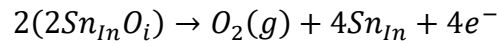
and 2 electrons per reduced complex are released into the $In_2O_3$ conduction band.

Currently, commercially-used ITO thin films are produced via vacuum sputtering deposition, which yields the best combination of electrical and optical properties of high conductivity ($\sim 10^{-4}$ $\Omega$-cm) and high optical transparency ($> 95\%$),[50,51] respectively. However, there is significant economic motivation to replace vacuum deposition processes with solution-processing in order to reduce material waste[42,52] and improve system compatibility with emerging soft-electronics such as organic electronics, perovskite solar cells, and flexible substrates.[53–57] Colloidal ITO nanocrystals are a prime candidate for solution processed TCO's, as they are readily adaptable to industrial solution processes, have low impurity contamination compared to their molecular TCO precursor counterparts, and are fully crystalline upon deposition. The use of ITO nanocrystals as solution-cast thin film precursors is discussed in greater detail in Chapter III.

**Plasmonic Metal Oxide Nanocrystals**

Doped metal oxide nanocrystals, such as ITO, can exhibit plasmonic properties much like metallic nanocrystals. Plasmonic nanocrystals have use in a variety of applications including spectroscopy,[58,59] sensing,[60–62] and biomedical agents.[19,63] Plasmonic materials are generally thought of as noble metal nanocrystals (such as Au or Ag), however when metal oxide nanocrystals are doped to sufficiently high levels they will exhibit a plasmon resonance, albeit at lower energies than their noble metal counterparts. The energy of the plasmon resonance is directly proportional to the free electron concentration of the material, given by Equation 1:

$$\omega_p = \sqrt{\frac{N_e e^2}{m^* \varepsilon_o}} \tag{1}$$

where $\omega_p$ is the bulk plasma frequency, $Ne$ is the free carrier concentration, $e$ is the elementary charge, $m^*$ is the effective mass, and $\varepsilon_o$ is the permittivity of free space. The plasmon resonance arises from the free electrons in the metal oxide's conduction band introduced from the dopant atoms, $e.g.$, Sn-doped $In_2O_3$. Metal oxide nanocrystals are especially intriguing as plasmonic materials because their properties can be readily tuned through composition, unlike the noble metal materials whose electron concentrations and plasmon energies are fixed. As a consequence, the optical utility of plasmonic metal nanocrystals is limited to 300 – 1000 nm, whereas the plasmon in metal oxide nanocrystals can be readily tuned from 500 – 25000 nm. This breadth of optical utility for plasmonic metal oxide nanocrystals is unrivaled, and yields a wide range of potential applications from medicine to telecommunications.

However, in order to integrate plasmonic oxide materials into modern technologies, synthetic control must be improved. As discussed earlier in the Chapter, the dopant atoms are often difficult to incorporate into the host lattice, and surface segregation may be much more common than previously acknowledged.[64] The plasmonic properties of metal oxide nanocrystals have been shown to depend upon the distribution of dopants within the nanocrystals, and this dependency can have an even greater influence the properties than composition alone. Prior to the report by Jansons *et al*,[10] there was no known way to synthetically control dopant distribution at the sub-nanometer level. This level of structural control over a nanocrystal composition is required in order to better design plasmonic nanomaterials, and in order to gain a more complete fundamental understanding of structural effects on plasmonic material properties. Chapter 4 discusses in greater detail the impacts of dopant distributions on the plasmonic properties of metal oxide nanocrystals, as well as new synthetic approaches to designing nanocrystal compositions at the sub-nanometer level.

**Dissertation Overview**

Chapter II demonstrates unprecedented control over the composition of doped metal oxide nanocrystals, made possible by a slow, continuous injection approach. We show incorporation of several first row transition metal dopants into an $In_2O_3$ matrix, and the dopant concentration can be controlled simply by adjusting the precursor metal ratio. The resulting nanocrystal compositions are in agreement with the precursor composition, most of the dopant atoms incorporate with > 90% efficacy, and the distribution of dopant atoms is homogeneous throughout the nanocrystals. This synthetic approach allows the

production of doped nanocrystals with custom, well-defined composition and size. This level of structural control is essential to developing the fundamental relationships between composition, structure, and properties of nanocrystals. Chapter II is reprinted from a published article in Chemistry of Materials (Jansons, A. W.; Koskela, K. M.; Crockett, B. M.; Hutchison, J. E. Transition Metal-Doped Metal Oxide Nanocrystals: Efficient Substitutional Doping Through a Continuous Growth Process. *Chem. Mater.* **2017**, *29* (19), 8167–8176.). Experiments were performed by Kristopher Koskela, Adam Jansons, and myself. All four co-authors wrote the paper.

Properties of Nanocrystals not only depend upon composition, but importantly depend upon size. Chapter III displays how nanocrystal size impacts thin film electrical properties, namely thin film resistivity. Using the continuous injection synthesis, a size ladder of Sn-doped $In_2O_3$ nanocrystals containing seven samples ranging from 5 to 21 nm in diameter is produced. The nanocrystals are shown to be solution-processable into thin films under mild conditions. The resulting thin film resistivities were measured, and the values decreased by an order of magnitude as nanocrystal size was increased from 5 to 21 nm. Traditional metal oxide nanocrystal syntheses were unable to produce the size ladder required to perform the study, and the study represents a significant advancement in metal oxide nanocrystal synthesis and should enable similar size-property relationships to be developed in other systems. Chapter III is reprinted from an article under review at Chemistry of Materials (Crocket, B. M.; Jansons, A. W.; Koskela, K. M.; Sharps, M. C.; Johnson, D. W.; Hutchison, J. E. Transition Metal-Doped Metal Oxide Nanocrystals: The influence of nanocrystal size on optoelectronic properties of thin, solution cast Sn-doped $In_2O_3$) Experiments were performed by Kristopher Koskela, Adam Jansons, Meredith

Sharps, and myself.  I wrote the manuscript in collaboration with Adam Jansons and James Hutchison.

Nanocrystal properties depend on composition, size, and structure, and the independent alteration of these attributes has been the ultimate frontier in nanoscience. Chapter IV demonstrates the combination of atomic-level control over composition with nanometer-level control over size, allowing for structural influences on exotic optical properties to be explored, particularly the localized surface plasmon resonance (LSPR). LSPRs arise in degenerately-doped semiconducting nanocrystals, where the dopant atoms yield free electrons. Generally, the LSPR in metal oxide nanocrystals is tuned through composition and the concentration of incorporated dopant atoms. Here we show that by combining the compositional control displayed in Chapter II, with the size control displayed in Chapter III, the radial position of dopant atoms came be precisely controlled within the nanocrystal. Using Sn-doped $In_2O_3$, the radial positions of the Sn atoms is shown to profoundly impact the LSPR properties including the LSPR energy, damping (proportional to linewidth), and the dopant activation (the number of electrons donated per tin dopant atom). This approach gives the community a new way to design plasmonic materials that decouples the properties from composition alone. Chapter VI is reprinted from a published article in ACS Nano (Crockett, B. M.; Jansons, A. W.; Koskela, K. M.; Johnson, D. W.; Hutchison, J. E. Radial Dopant Placement for Tuning Plasmonic Properties in Metal Oxide Nanocrystals. *ACS Nano* **2017**, *11* (8), 7719–7728). Experiments were performed by Adam Jansons, Kristopher Koskela, and myself. I wrote the manuscript in collaboration with Adam Jansons and James Hutchison.

Finally, Chapter V discusses conclusions and closing ideas regarding the continuous growth synthesis, and gives insight into future avenues of investigation and inquiry.

CHAPTER II


TRANSITION METAL-DOPED METAL OXIDE NANOCRYSTALS: EFFICIENT

SUBSTITUTIONAL DOPING THROUGH A CONTINUOUS GROWTH PROCESS


This chapter was previously published as Jansons, A. W.; Koskela, K. M.; Crockett, B. M.; Hutchison, J. E. Transition Metal-Doped Metal Oxide Nanocrystals: Efficient Substitutional Doping Through a Continuous Growth Process. *Chem. Mater.* **2017**, *29* (19), 8167–8176. Copyright 2017 American Chemical Society


## Introduction

The intentional introduction of defects into host structures is the foundation for useful properties that are utilized today in many important applications. This approach has long been used in bulk materials to alter the electronic, magnetic, and physical structure of semiconductors,[1,2] and is essential to the modern microelectronics industry. Similarly in nanocrystals, the introduction of defects through dopant incorporation imparts interesting properties that we are beginning to understand and harness in applications.[3–6] Exciting recent discoveries of magnetic,[7–12] luminescent,[13–21] catalytic,[22–24] and optoelectronic[25–31] properties of nanocrystals have been investigated as a result of nanocrystal doping. These properties can be further enhanced if advanced synthetic strategies are developed.[32,33]

While many synthetic approaches for the production of doped oxide nanocrystals have been established,[34–45] several challenges remain. Producing doped nanocrystals with precise control of nanocrystal size, composition, and internal structure remains a large

barrier to broader adoption and further technological advancement.[4] Doped nanocrystals are notorious for "self-purification," i.e., the exclusion of dopants from the host lattice— an argument that is often justified by considering the thermodynamics of impurity formation.[46,47] Thermodynamics are also cited when considering that dopant incorporation levels in nanocrystals have traditionally been well below the solid solubility limits found in bulk analogs and rarely contain > 10 atomic % dopant. The argument falls short however, when considering that kinetics rather than thermodynamics controls this process at the nanoscale.[48,49] It is widely believed that substitutional doping can only be obtained if dopants can find their way onto the surface of the nanocrystal for long enough that they become surrounded by host monomer overgrowth.[46,48,50,51] Thus, consideration of the nanocrystal surface chemistry—including size, shape, ligands, and functional groups— becomes extremely important for effective dopant incorporation.

In the many cases where kinetics controls the efficacy of dopant incorporation, considering both host and dopant precursor reactivity is critical for doped product formation.[50] If a balance between reaction rates is not met and the host precursor forms reactive monomer faster than dopant precursor, then dopant incorporation could be low or absent. Conversely, if dopant precursor formation kinetics are faster than the host, new crystal phases are produced that contain primarily the dopant element. Even if conditions are favorable for uniform doping at nucleation, dopant incorporation is known to be dependent on specific crystal facets and/or ligand environment,[49] which may not be constant as crystal growth continues. Therefore, the majority of doped-nanocrystal synthetic methods attempt to obtain this balance through careful, and often tedious, trial

and error selection of precursors and synthetic conditions in order to match precursor reactivity rates and subsequently form a substitutionally-doped nanocrystal.

Production of a doped structure, however, is not the final measure of success. Different synthetic methods can produce equivalent composition yet yield nanocrystals with undesirable variations in radial dopant locations. These small structural differences may drastically affect properties.[52,53] In addition, some synthetic methods give rise to large variations in the number of dopants per nanocrystal within an ensemble, beyond that predicted by Poisson statistics.[54] Here again, variations in composition can drastically influence the desired properties.[32] Besides composition and structure, control of nanocrystal size becomes an additional challenge because the properties of nanomaterials are size dependent. Synthetic approaches are usually developed to control size or produce a desired composition but generally not both. This is because the introduction of dopants disrupts the thermodynamics of nucleation,[54] making it difficult to control both dopant incorporation and size with desired precision.

Exploration of new synthetic approaches to doped nanocrystals to complement rapid-injection or thermal decomposition reactions may be valuable given the significant challenges in producing and controlling the composition, structure, and size. Rather than precipitation reactions, which trap dopants in a crystalline matrix, we hypothesized that the use of reactive surface functional groups could facilitate the incorporation of transition metal dopants into a host oxide lattice. An ideal synthetic method would allow the layer-by-layer growth of nanomaterials with precise control over the composition in each layer, thus allowing enhanced control over both overall nanocrystal composition and radial structure. Ideally, such a method would be amenable to a wide variety of dopants, and

would facilitate the predictable incorporation of dopants at levels near thermodynamically-predicted solid solubilities.

A number of authors have highlighted the need to carefully choose the right precursors (often a metal alkylcarboxylate) to effectively form the desired doped product.[40,50,55] Without the appropriate precursors, host and dopant precursors reactivities may not be sufficiently matched.  We thought that using a slower, layer-by-layer nanocrystal growth process would facilitate more even incorporation of dopant atoms while preventing coalescence or ripening.[56,57] Thus, carefully choosing metal precursors may not be necessary, and for this reason we chose to simply use metal oleates for both host and dopant precursors.  Further, the slow addition of precursor allows particle growth to occur with constant concentration of dopant in each added layer, ensuring that dopant atoms are homogeneously distributed radially throughout the structure.

Herein we report the synthesis of substitutionally doped Mn, Fe, Co, Cu, and Zn-doped $In_2O_3$ nanocrystals at 5, 10, and 20 atomic percent.  We find that dopant incorporation efficacy is nearly quantitative, which allows the logical preparation of highly-doped nanocrystaline structures.  With the exception of the Cu-doped nanocrystals, which we found to temporarily incorporate into the oxide lattice before surface segregation, the dopant cations are homogeneously-distributed throughout the nanocrystal without surface or core localization.  As a wide bandgap oxide, $In_2O_3$ allows ligand field transitions to be observed in visible energies, allowing one to probe the optical properties resulting from doping.  The observed electronic transitions of first row transition metal dopants in the $In_2O_3$ structure indicate that dopants lie in octahedral geometries, which is consistent with substitutional incorporation of the cations.  The slow, controlled growth of oxide

nanocrystals made possible by this synthetic method makes it possible to precisely control the internal nanocrystal structure and composition.

**Results and Discussion**

An alternative approach to traditional thermal decomposition reactions are the use of so called nonaqueous sol-gel reactions to synthesize doped oxide nanocrystals.[27,35,37,40,41,50,55,58,59] These reactions rely on predictable principles from organic chemistry to arrive at reactive monomer.[60] Using an esterification-based mechanism, we recently showed that a variety of binary oxide nanocrystals, including $In_2O_3$, $\gamma$-$Fe_2O_3$, $Mn_3O_4$, CoO, and ZnO, could be obtained through the slow addition of metal carboxylate into long-chain alcohol at elevated temperatures.[59] Particle growth is facilitated by the production of reactive metal hydroxyl groups, which subsequently condense with hydroxyls on the particle surface. Because the method relies on metal-catalyzed esterification and not thermal decomposition, we thought this approach could be used to precisely control dopant incorporation into oxide nanocrystals simply by tuning precursor molar ratios. Further, we hypothesized that we may be able to access dopant concentrations higher than those typically reported for semiconducting nanocrystals, owing to the kinetic control provided by the living growth process. If this growth process supports continuous growth by both matrix and dopant precursors, we would expect dopant incorporation efficacies near 100%, well beyond those typically found for the production of doped oxide nanocrystals.

Previous studies using the slow-addition of metal carboxylates into oleyl alcohol had shown that the method is amenable to the production of Sn-doped $In_2O_3$ (ITO) nanocrystals with very high dopant efficacies, and produced nanocrystal product in high

yield.[53,56,59]  Because Sn and In are similar in size and reactivity, synthesizing ITO with controlled composition was interesting, but not surprising.  We sought to investigate the incorporation of transition metal cations to determine how differing sizes of cations influence their incorporation into the oxide lattice..

Using $In_2O_3$ as a model oxide system, we synthesized Mn: $In_2O_3$, Fe: $In_2O_3$, Co: $In_2O_3$, Cu: $In_2O_3$, and Zn: $In_2O_3$ nanocrystals at nominal dopant concentrations of 5, 10, and 20 atomic %.  Indium oxide was chosen as an appropriate model system because of its importance as a transparent electrode,[61] its emergence as a model system for the study of unique optoelectronic properties including near-IR localized surface plasmon resonances (LSPRs),[62] and its role as a host material for dilute magnetic oxides.[63]   During synthesis, we kept the total metal content in the precursor at one mmol as a convenient point of comparison.  Synthesizing larger particle sizes with sub-nanometer precision and producing larger quantities of product is possible simply by adding more precursor.[53,56] The transition metal dopants used have a range in effective ionic radii from 69 pm (for octahedrally coordinated $Fe^{3+}$) to 88 pm (for $Zn^{2+}$),[64] allowing us to probe the influence of cation size on dopant incorporation efficacy.  The radius of $In^{3+}$ in the $In_2O_3$ host matrix is 94 pm.[64]

After the addition of the metal oleate precursor, nanocrystals were purified by multiple precipitations with an anti-solvent (ethanol) and collected by centrifugation.  No size selection processes were used.  Size, size dispersion, and shape were determined by small-angle X-ray scattering (SAXS) and transmission electron microscopy (TEM). Figure 2.1 displays TEM images of the doped nanocrystals at each dopant concentration. SAXS results (Table 2.1) corroborate nanocrystal size and size dispersion data from TEM.

Several anticipated outcomes become apparent from these data. First, the presence of a dopant cation influences the mean size of nanocrystal produced based upon the addition of one mmol of total metal (host + dopant) precursor. Compared to undoped $In_2O_3$ nanocrystals, the addition of dopant cations produce a smaller mean size of nanocrystals, with higher dopant concentration in the precursor leading to a further decrease in the mean size of the product. The influence of dopant cations on the driving force for homogeneous nucleation has been discussed,[54] and a similar trend in mean size with the presence of dopants has been observed.[65] As expected, more dopant cations on the surface of the nanocrystal leads to a slower initial growth rate of the initial formed nuclei allowing new nucleation to occur. Previous authors have similarly attributed the change in doped nanocrystal size to a thermodynamic barrier of growth onto doped nanocrystals because surface dopants modify the surface energy of the nanocrystal.[65,66] Eventually, with the accumulation of more monomer and now more nuclei in solution, growth can continue on the doped particles.

Increasing the dopant content in the precursor also increases the shape anisotropy of the formed nanocrystals, which is reflected in the polydispersity measurements by SAXS shown in Table 2.1. Since only metal oleates and oleyl alcohol are present in each of the reaction mixtures, we can confirm that shape changes are only due to the dopant cations and not additional coordinating reagents or changes in reaction conditions. Nanocrystal shape changes with dopant addition are well documented in literature,[27,41,50,67] and it is possible that dopants may alter the ligand-metal binding energies as well alter the surface energies of specific crystallographic facets, leading to anisotropic growth. Unraveling the precise mechanism with which the dopants lead to the varying morphologies is beyond the

scope of this work. However, it is worth pointing out that while some dopants, like Fe, seem to only slightly change the particle morphology, other dopants, like Mn and Co, drastically alter size and shape of the formed nanocrystals at higher concentration.
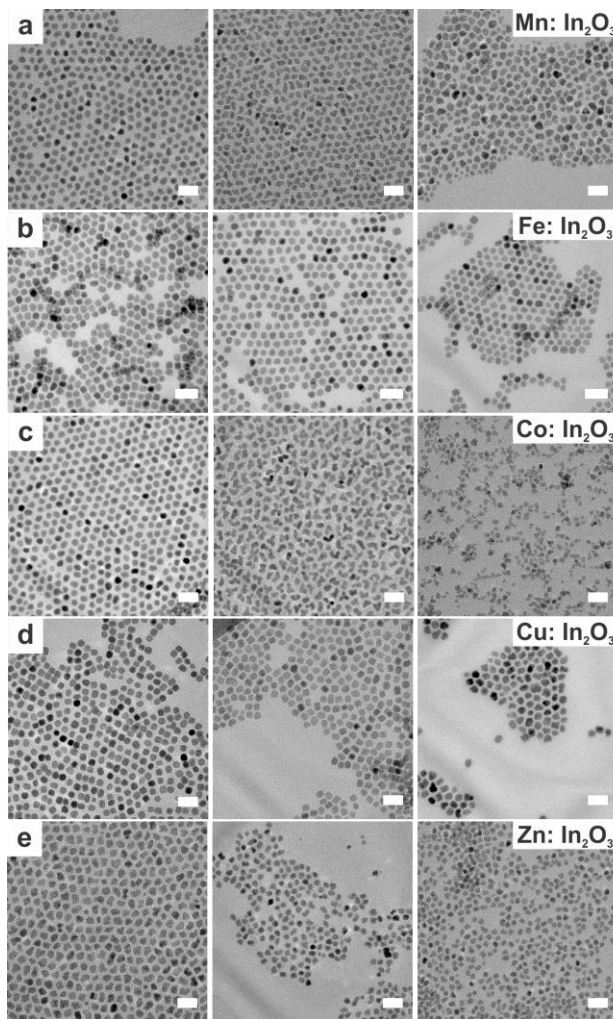


**Figure 2.1.** TEM images taken of doped $In_2O_3$ nanocrystals at varying molar dopant ratios. Scale bars are 20 nm. The nominal dopant percent in the precursor increases from left to right, 5% dopant on the left, 10% center, and 20% right. Panel **a**) displays Mn: $In_2O_3$, **b**) Fe: $In_2O_3$, **c**) Co: $In_2O_3$, **d**) Cu: $In_2O_3$, and **e**) Zn: $In_2O_3$

**Table 2.1.** Doped nanocrystal size and size dispersion from SAXS.

| Dopant | Nominal dopant % in precursor | Size (nm) | % Polydispersity |
|---|---|---|---|
| undoped In$_2$O$_3$ | 0 | 8.2 | 10.7 |
| Mn | 5 | 7.3 | 12.0 |
| Mn | 10 | 6.3 | 17.5 |
| Mn | 20 | 5.0 | 27.1 |
| Fe | 5 | 7.4 | 12.3 |
| Fe | 10 | 7.1 | 12.2 |
| Fe | 20 | 6.0 | 14.8 |
| Co | 5 | 7.2 | 10.1 |
| Co | 10 | 6.6 | 32.5 |
| Co | 20 | 4.8 | 41.5 |
| Cu | 5 | 7.9 | 9.9 |
| Cu | 10 | 7.9 | 10.6 |
| Cu | 20 | 7.2 | 14.5 |
| Zn | 5 | 7.5 | 16.1 |
| Zn | 10 | 6.1 | 14.1 |
| Zn | 20 | 5.8 | 14.6 |

The compositions of the nanocrystals were determined by inductively coupled plasma optical emission spectroscopy (ICP-OES). After purification, the nanocrystals were dissolved in nitric acid and diluted for elemental analysis. Table 2.2 compares the precise nominal dopant concentration in the added precursor with the dopant concentration found in the purified nanocrystals. As displayed, most dopants incorporate with > 90% efficacy, even at dopant concentrations as high as 20%. Interestingly, in many of the higher doped samples, efficacies surpass 100%, indicating that indium monomer is disproportionally excluded from the growing nanocrystals. For the Cu: In$_2$O$_3$ nanocrystals, the efficacy of incorporation of the dopant is much lower compared to the other dopants. We will discuss the copper samples separately later in this discussion.

**Table 2.2.** Dopant concentrations in purified nanocrystals compared to the precursor composition, and the resulting dopant incorporation efficacy.

| Dopant | Precise nominal dopant concentration (atomic %) | Nanocrystal dopant concentration (atomic %, ICP-OES)* | Dopant incorporation efficacy (%) |
|---|---|---|---|
| Mn | 4.9 | 4.8 | 98 |
| Mn | 9.8 | 9.0 | 92 |
| Mn | 20.2 | 21.3 | 105 |
| Fe | 5.1 | 4.9 | 96 |
| Fe | 9.9 | 9.1 | 92 |
| Fe | 19.8 | 20.4 | 103 |
| Co | 5.4 | 4.9 | 91 |
| Co | 10.4 | 10.1 | 97 |
| Co | 20.3 | 20.8 | 102 |
| Cu | 5.2 | 4.8 | 92 |
| Cu | 10.9 | 7.3 | 67 |
| Cu | 20.4 | 15.6 | 76 |
| Zn | 6.0 | 5.9 | 98 |
| Zn | 12.3 | 11.5 | 93 |
| Zn | 20.5 | 19.9 | 97 |

*Concentrations determined by ICP-OES have standard deviations of $\leq 0.05$ atomic %

We also utilized X-ray photoelectron spectroscopy (XPS) on selected doped samples to complement the measurements carried out with ICP-OES (see Figure A1 for example XPS spectra). XPS yields elemental information from the surface of the nanocrystals. At the binding energies investigated, XPS samples a depth of ~3 nm in $In_2O_3$.[68] This sampling depth does not take into account the organic ligand shell, but scattering of signal due to the organic ligands is less than the inorganic core. Using XPS, along with complementary elemental analysis by ICP-OES, allows one to probe the radial distribution of dopant atoms in the nanocrystal, which is a small yet extremely important detail that is often overlooked in the characterization of doped nanocrystals. We integrated the In $3d_{5/2}$ peaks and the transition metal dopant $2p_{3/2}$ peaks to assess the dopant concentration near the nanocrystal surface. The fact that the values for dopant concentration found near the surface (by XPS) match those found for bulk measurements

(by ICP-OES) (Table 2.3) suggests that dopants are homogeneously distributed throughout the nanocrystal, and not surface segregated. We could not obtain accurate elemental information by XPS from the Fe: $In_2O_3$ samples, as the Fe 2p peaks, which have the highest sensitivity factor, are buried by a large In 3p loss feature. The Fe 3p peaks do not have a sensitivity factor high enough to accurately quantify Fe content on the surface. In some cases where the nanocrystals are small (< 6 nm), it may be possible that XPS is sampling more than half the nanocrystal. In this case, the combination of ICP-OES and XPS might not appropriately assess the radial dopant position and both techniques would yield similar compositions. While this is a possibility for some of the nanocrystals investigated in Table 2.3, it is apparent from the data for the largest nanocrystals that dopants are not segregating at the surface or forming amorphous clusters on the surface, as this scenario would lead to stronger dopant signal.

**Table 2.3.** Comparison of dopant concentrations in the purified nanocrystals by ICP-OES and XPS.

| Dopant | Nominal dopant concentration (atomic %) | Dopant atomic % (ICP-OES) | Dopant atomic % (XPS)* |
|:---:|:---:|:---:|:---:|
| Mn | 9.8 | 9.0 | 9.6 |
| Co | 10.4 | 10.1 | 11.2 |
| Zn | 6.0 | 5.9 | 5.1 |
| Zn | 12.3 | 11.5 | 11.7 |
| Zn | 20.5 | 19.9 | 20.1 |

*Concentrations determined by XPS have a standard deviation of $\leq 0.2$ atomic %

In order to confirm that the dopant atoms are substitutionally incorporating into the $In_2O_3$ lattice, we studied structural changes of the nanocrystals with X-ray diffraction (XRD). For all dopant cations at all concentrations investigated we found no evidence of secondary phases or crystalline phases other than cubic bixbyite $In_2O_3$ (Figure 2.2). This finding contrasts with previous reports that identified the corundum-type crystal structure

for doped $In_2O_3$ nanocrystals at certain dopant concentrations or crystal sizes.[69,70] Further inspection of the XRD patterns in Figure 2.2 reveals small shifts and changes in intensity for the diffraction peaks as the dopant concentration is increased. These variations are most evident in the (222), (400), and (440) reflections. The influence on the other diffraction peaks are harder to discern given the broadening due to small crystallite size. Increased broadening at higher dopant concentrations is the result of smaller crystallite sizes, confirmed by SAXS and TEM data (Figure 2.1 & Table 2.1).

Using Rietveld analysis[71] (Figure A2), we extracted the cubic lattice constant $a$ for each of the doped nanocrystal samples. Figure 2.3 plots the extracted lattice constants as a function of dopant concentration found by ICP-OES. The lattice constant of the undoped $In_2O_3$ nanocrystals matches that of bulk $In_2O_3$, both 10.117 Å (JCPDS no. 06-0416). As displayed in Figure 2, the lattice constant decreases for all samples with incorporated dopant, and further decreases with additional dopant presence, as expected by Vegard's law.[72] Furthermore, the difference in slopes for each dopant qualitatively matches the expected trend when comparing octahedrally coordinated ionic radii of the specific cations used as precursors. From the literature,[64] we find the trend in octahedrally coordinated ionic radii of cations: $Fe^{3+}$ (69 pm) < $Co^{2+}$ (79 pm) < $Mn^{2+}$ (81 pm) < $Zn^{2+}$ (88 pm) < $In^{3+}$ (94 pm). It has previously been shown in oxide nanocrystals that a decreasing crystallite size leads to an increase in the crystalline lattice constant.[73] The fact that we observe a *decreased* lattice constant (Figure 2.3) despite the decreasing crystallite size for doped products (Figure 2.1 and Table 2.1) strongly suggests that the cations are substitutionally doping for $In^{3+}$ cations.

25
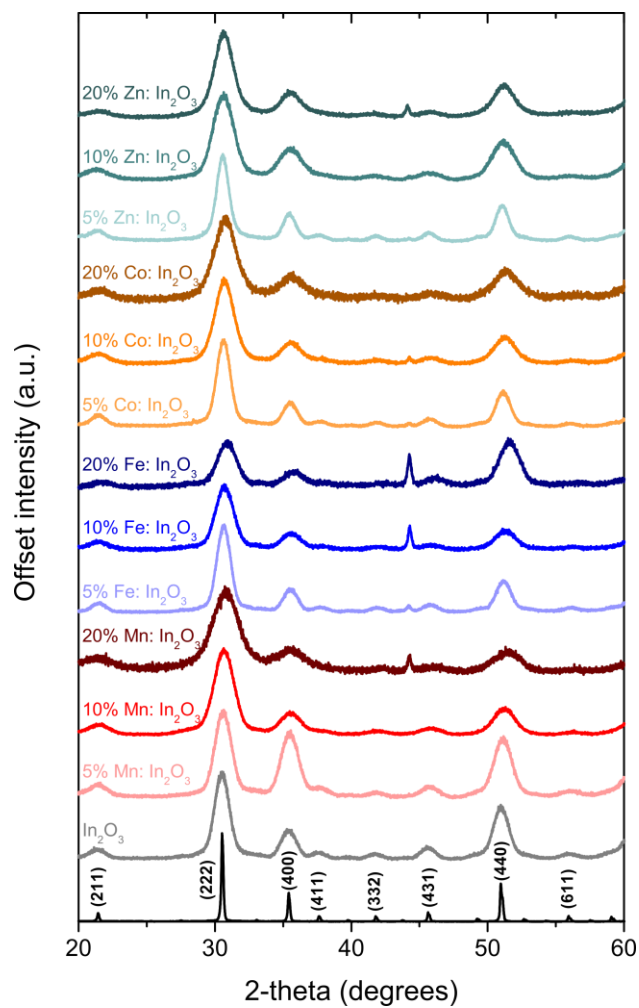
**Figure 2.2.** X-ray diffraction patterns of bulk (black, bottom trace), undoped (grey trace), and Mn, Fe, Co, and Zn doped indium oxide nanocrystals at 5, 10, and 20% dopant concentrations. The peak present at 43.5 $^{o}$ in some samples is due to the silicon substrate.
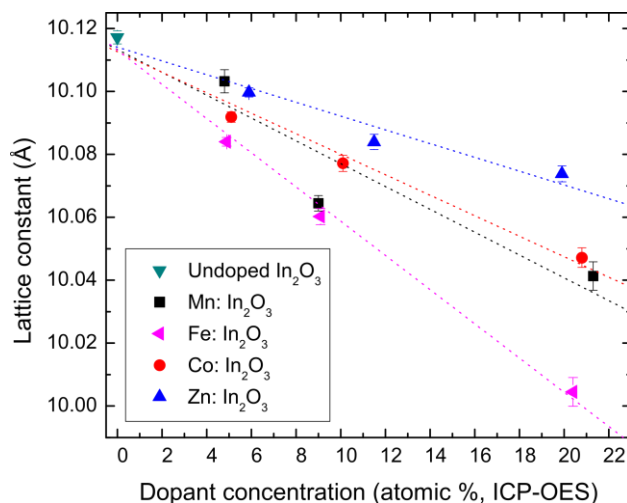
**Figure 2.3.** Lattice constants extracted through Reitveld analysis for doped and undoped nanocrystals plotted as a function of dopant concentration from ICP-OES. Predictable decreases in lattice constant as a function of increased dopant incorporation suggest substitutional doping in the oxide nanocrystals.

Further evidence of substitutional doping can be found from electronic absorption spectroscopy. Figure 2.4 displays the absorbance spectra for the 10% doped nanocrystals at two concentrations. Spectra collected at low concentration (~0.05 mg/mL) make it possible to observe the band-edge absorption. Spectra collected at higher concentration (~10 mg/mL) can be used to identify ligand field transitions of the octahedrally coordinated metal centers. In the bixbyite structure, $In^{3+}$ resides in two distinct six-coordinated sites within the lattice, the $b$ and $d$ sites.[39,70,74] Dopants with cation radii smaller than $In^{3+}$ are thought to reside in the distorted octahedral $d$ sites, with $C_2$ point group symmetry.[70,75] A solution of Mn: $In_2O_3$ nanocrystals suspended in hexanes at room temperature (Figure 2.4b) gives rise to a pink/red color, which, at first appearance, is characteristic of octahedrally coordinated $Mn^{2+}$ complexes.[76] However, it is more likely these transitions arise from spin-allowed $^5E_g \rightarrow {}^5T_{2g}$ transitions of $Mn^{3+}$, as previously reported and discussed from a

separate synthesis of Mn: $In_2O_3$ nanocrystals by Radovanovic *et al.*[70] The electronic spectra reported in their study qualitatively match the spectrum in Figure 2.4b. They assigned this transition to a $d^4$ ion in a rhombic environment (which, as they point out, is structurally similar to the $d$ site of a bixbyite lattice). In this environment, $T_{2g}$ and $E_g$ terms split further into A and B terms.[70,76] Given these considerations and previously discussed spectra,[70] we can assign the peaks at ~18,000 $cm^{-1}$, ~20,000 $cm^{-1}$, and ~22,000 $cm^{-1}$ to the $^5B_g \rightarrow \, ^5A_g$, $^5B_g \rightarrow \, ^5B_g$, and $^5B_g \rightarrow \, ^5A_g$ transitions, respectively. Figure 2.4f shows solutions of the 5, 10, and 20% Mn: $In_2O_3$ nanocrystals at the same concentration by mass (5 mg/mL), displaying the increasing intensity of the absorbance for the charge transfer and d-d transitions as the dopant concentration is increased.

Octahedrally coordinated $Fe^{3+}$ cations generally exhibit much weaker d-d transitions than other $d^5$ systems, and therefore are not expected to appear in the absorbance spectrum shown in Figure 2.4c.[76] A previously reported synthesis and characterization of Fe: $In_2O_3$ nanocrystals assigns a similar peak at ~21,000 $cm^{-1}$ to ligand-to-metal charge transfer transitions.[77] Elsewhere, Fe-doped $In_2O_3$ nanocrystals produced by a colloidal synthesis[78] were reported to have a color that qualitatively matches that of the solution in Figure 2.4b; however, no electronic absorbance data were reported. The absorbance spectrum of Co: $In_2O_3$ is displayed in Figure 2.4d. The broad absorption is similarly likely due to ligand-to-metal charge transfer. Comparing the spectrum in Figure 2.4d to previously reported $Co^{2+}$ pseudooctahedral complexes,[76] a possible $^4T_{1g} \rightarrow \, ^4T_{1g}(P)$ transition may be present at ~18,000 $cm^{-1}$. Co: $In_2O_3$ thin films showed similar absorption features, though their origin was not discussed.[79] As expected, undoped $In_2O_3$ (Figure 2.4a)

and Zn: $In_2O_3$ (Figure 2.4e) do not give rise to any d-d transitions in the visible region ($Zn^{2+}$ is a $d^{10}$ metal center).
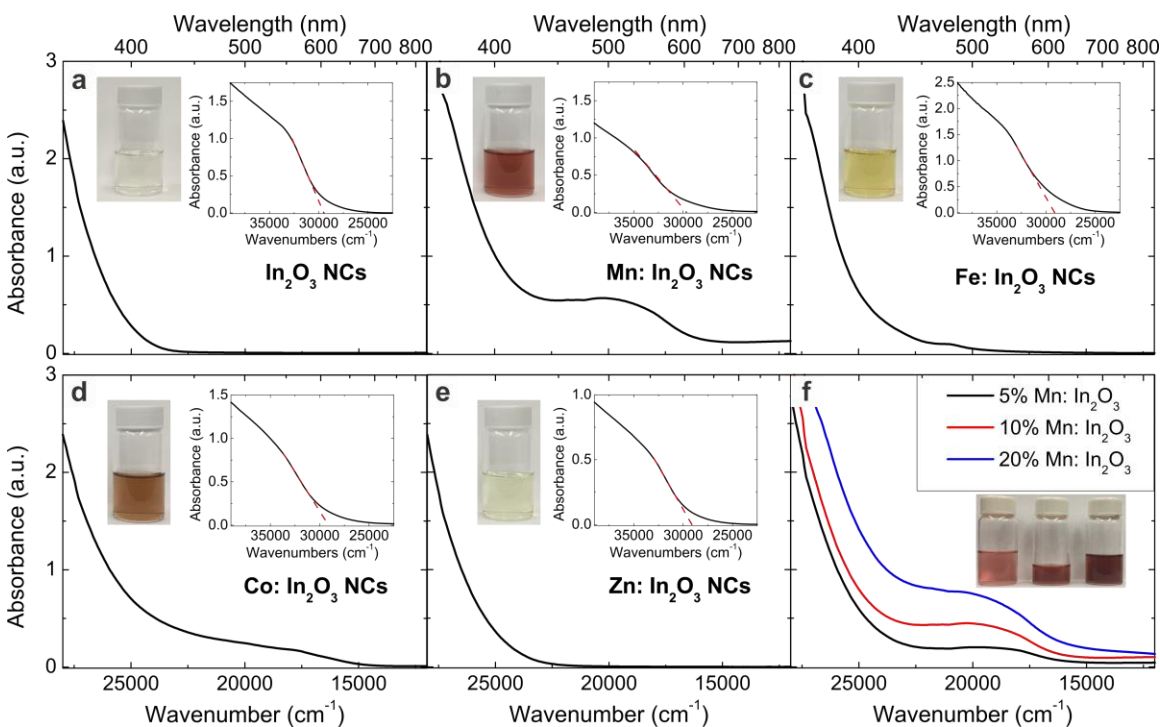


**Figure 2.4**. Electronic absorbance spectra collected on solutions of nanocrystals in hexanes at room temperature along with pictures of the solutions. Inset plots display spectra from dilute solutions (~0.05 mg/mL) of the nanocrystals that can be used to obtain band gap energy estimates. **a**) undoped $In_2O_3$ nanocrystals, **b**) Mn: $In_2O_3$, **c**) Fe: $In_2O_3$, **d**) Co: $In_2O_3$, and **e**) Zn: $In_2O_3$. **f**) absorbance spectra from solutions of 5, 10, and 20 atomic % doped Mn: $In_2O_3$ nanocrystals, all at constant concentration (5 mg/mL). The inset shows pictures of all three solutions, increasing in dopant concentration from left to right.

Band gap energies of doped and undoped $In_2O_3$ are estimated from absorption onsets from dilute solutions of nanocrystals shown in Figure 2.4. For undoped $In_2O_3$,

absorbance onset occurs at ~29,500 cm$^{-1}$, corresponding to a band gap ~ 3.66 eV. Bixbyite In$_2$O$_3$ is commonly reported as having a bandgap between 3.5-3.7 eV.[80] All doped samples display a slightly red-shifted absorbance onset of ~29,000 cm$^{-1}$ (~3.60 eV). The slight decrease in bandgap with doping has been attributed to donor states which arise within the band, likely from charge compensating oxygen vacancies.[79] The presence of dopant cations likely lowers the energy of vacancy formation.[81] A qualitative measure of oxygen vacancy content can be assessed by examining the near-infrared/infrared localized surface plasmon resonance (LSPR) absorbance of the nanocrystals, which arise in oxide nanocrystals due to free carriers formed via doping, or in this case, oxygen vacancies.[25,31,82,83] The peak of the LSPR is directly proportional to the free electron content of the nanocrystals.[84] IR spectra (Figure A3) of undoped In$_2$O$_3$ displays a weak LSPR absorbance ~1,400 cm$^{-1}$, while the doped samples display a broader, more intense absorption centered at energies > 4,000 cm$^{-1}$. The shift in the LSPR to higher energy indicates a higher free electron concentration in the doped samples, a direct result of the larger concentration of vacancy defects. Fitting of the O1s XPS spectra (Figure A1) for 5 and 20% Zn: In$_2$O$_3$ samples results in a more prominent peak at 529.7 eV, suggesting a higher degree of oxygen deficient/defective oxide sites that increase as the dopant concentration increases. Notably, these defects have been shown to enhance some favorable properties, including sensitivity to oxidizing or reducing gases when these materials are used as the active component in gas sensors.[85–87]

As shown in Figure 2.1, the synthetic method also produced Cu: In$_2$O$_3$ nanocrystals. Copper ions have traditionally been difficult to dope within intrinsically n-type oxides,[88,89] and indium oxide has recently been shown to be an effective diffusion barrier to copper.[90]

The fact that we were able to incorporate copper highlights the kinetic control possible with the slow addition method. After isolation of the Cu doped nanocrystals, however, we noticed some gradual changes in the properties of the material. Immediately after purification and dispersion of the synthesized nanocrystals in hexanes the color of the solution appeared dark red. One day after leaving the solution at room temperature, the solution color changed from red to a blue/grey, and gradually (over several days to ~ a week), changed to dark green (Figure 2.5a). The absorbance spectrum (Figure 2.5b) initially displayed a single absorbance band at ~17,530 cm$^{-1}$ that gradually shifts to lower energies as the solution color gradually turns green. Because the intensity of the peak in the spectra gradually decreases over time, a spectrum from a concentrated sample after two weeks is shown in the inset of Figure 2.5b, more clearly displaying the red-shifted peak at ~16,430 cm$^{-1}$. XRD patterns from the copper-doped samples (Figure 2.5c) display peaks consistent with the bixbyite $In_2O_3$ pattern. However, the peak intensities are irregular and accurate Rietveld refinements were difficult to obtain without significantly altering the occupancy of the unit cell. This is especially noticeable in the pattern two days after synthesis (Figure 2.5c, blue trace) that displays a (440) peak at 51° that is large relative to the (222) peak at 30°. A new pattern acquired on the same sample two weeks later shows expected relative intensities of the (222) and (440) peaks; however, refinements still resulted in a poor fit. From Braggs law, a qualitative understanding of the change in lattice constant can be found from the peak centers of the (222) and (440) peaks. Both peaks initially display peak centers shifted to higher 2-theta relative to undoped $In_2O_3$, consistent with a lattice contraction. Over time the peak centers shift to slightly smaller 2-theta, indicating a subsequent lattice expansion.

To account for the observed changes, we performed XPS on a sample immediately after synthesis and two days after synthesis.  As displayed in Figure 2.5d, the surface of the freshly made nanocrystal displays almost no copper present, while two days later copper appears on the nanocrystal surface.  No change in nanocrystal size or size dispersion was found via SAXS during this period.  Taken collectively, the data suggest that the electronic and structural changes are due to copper ions diffusing from the center of the crystal to the surface.  Copper is likely substitutionally doped for indium cations during synthesis, given the lattice contraction in the XRD pattern, though the irregularities in the pattern suggest that the unit cell is not contracting symmetrically.  Subsequent lattice expansion and appearance of copper in the XPS spectrum indicates that copper diffused through interstitial sites to the particle surface. Electronic absorbance spectra are consistent with a change in the coordination of the $Cu^{2+}$ ions,[91] though the precise coordination is very difficult to accurately identify.  $Cu^{2+}$ is well known to take many distorted octahedral coordinations, and it is often difficult to assign to a specific stereochemistry based on the absorption energy.[76,92]  To the best of our knowledge, very few reports of copper doped bixbyite structures have been published.[93]  Copper diffusion has long been studied in bulk semiconductors, much less, however, in oxide nanomaterials.
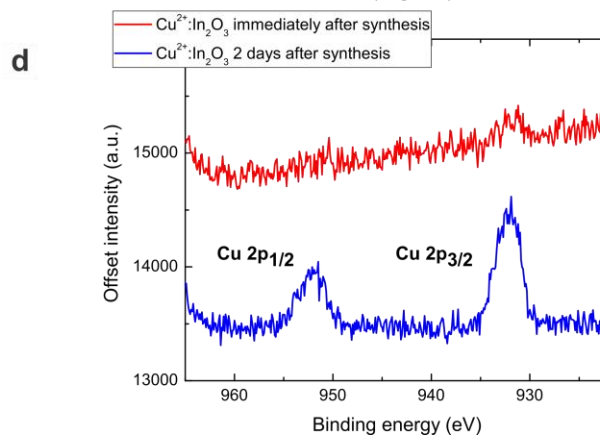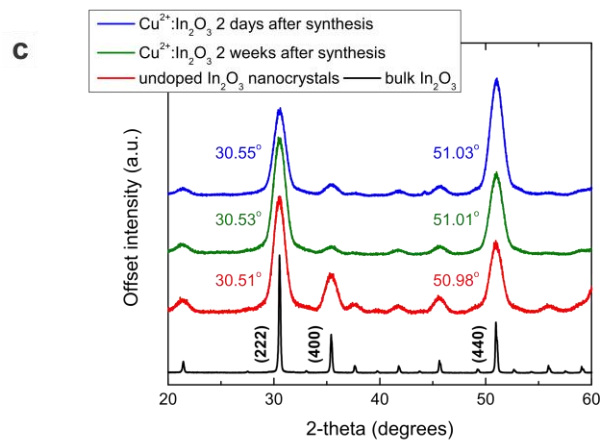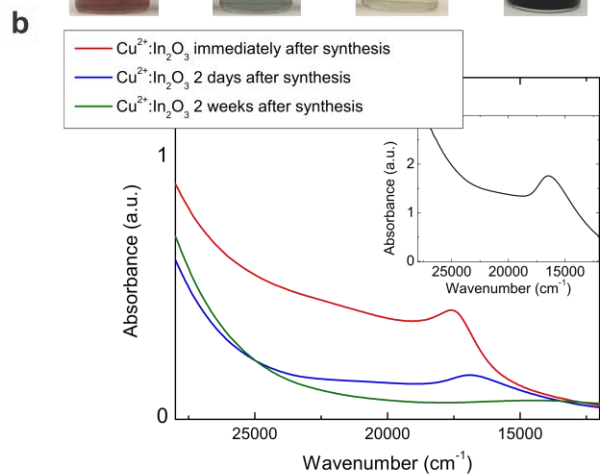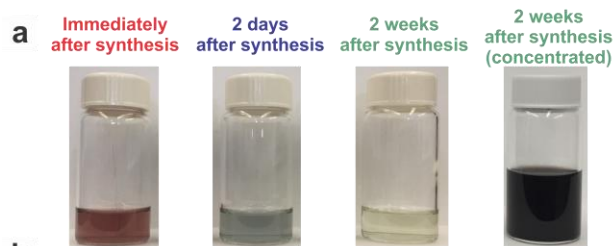
**Figure 2.5**. Characterization of Cu: $In_2O_3$ nanocrystals. **a**) Pictures of the purified nanocrystals dispersed in hexanes. From left to right, the nanocrystals the same day of synthesis, two days after synthesis, and two weeks after synthesis. The final vial shows a concentrated solution of the nanocrystals two weeks after synthesis. The optical absorbance spectra of these solutions are shown in **b**). Panel **c**) XRD spectra of the doped nanocrystals two days (blue) and two weeks (green) after synthesis. The spectra of bulk $In_2O_3$ and undoped $In_2O_3$ are shown for reference. **d**) XPS spectra of the Cu 2p region immediately (red) and two days (blue) after synthesis. The spectra indicate copper is diffusing towards the nanocrystal surface.

## Conclusion

Precise control of doped nanocrystal composition and structure is critical to the development and understanding of their important optical, magnetic, catalytic, and optoelectronic properties. Herein we synthesized substitutionally-doped Mn: $In_2O_3$, Fe: $In_2O_3$, Co: $In_2O_3$, Cu: $In_2O_3$, and Zn: $In_2O_3$ nanocrystals with dopant concentrations as high as 20%. Nanocrystal dopant concentration was controlled simply by the precursor feed ratio, allowing the logical preparation of compositions without the need for tedious trial and error. Dopant incorporation efficacy exceeded 90% for all dopants except for copper, which ranged from 67-92%, depending upon the feed ratio. Empirically selecting metal precursors was not necessary, and metal oleates of both host and dopant cations were used as metal precursors. This is made possible because the synthetic approach relies on the metal-catalyzed esterification of metal carboxylates, not thermal decomposition, and growth proceeds in a highly controlled, slow manner. The slow-growth approach allows

34

concentration of both host and dopant cation to be constant over time, ensuring that dopant cations are homogeneously distributed throughout the nanocrystal. That copper could be incorporated into the $In_2O_3$ lattice, despite its propensity to segregate to the nanocrystal surface, demonstrates the level of kinetic control of dopant incorporation offered by the living growth synthesis. Wide band-gap oxides, like $In_2O_3$, allow ligand-field transitions from dopant cations to be easily observed. We utilized these optical features, elemental composition analysis by ICP-OES and XPS, and XRD analysis, to confirm that dopants were substitutionally doping for $In^{3+}$ cations.

The slow-addition approach allows the layer-by-layer growth of nanocrystals, resulting in precise control of composition as crystal growth continues and enhanced size control of doped and undoped structures.[55] This opens up the possibility for the logical synthesis of graded nanostructures and the radial localization of dopants to specific locations within the nanocrystal. Additionally, co-doping or adding multiple dopants into the same nanocrystal, within the same or different radial location, open up a new range of property exploration and optimization. The synthetic approach should be amenable to other transition metal dopants (and matrix oxides), beyond those we report here, at large dopant concentrations and with high, near 100% efficacy. The ability to prepare highly-doped nanoscale structures without rigorous optimization will not only decrease the time and resources for the production of materials but also aid in understanding and utilizing properties found from new structures.

**Methods and Materials**

*Materials*

Indium(III) acetate (99.99%), manganese(II) acetate (98%), copper(II) acetate (98%), iron(III) acetylacetonate, zinc(II) acetate, oleic acid (90% technical grade), were purchased from Sigma Aldrich and used as received. Oleyl alcohol (80−85% technical grade) was purchased from Alfa Aesar and used as received. A flow meter Cole-Parmer (model 03216−10) was used to monitor nitrogen flow.

*Characterization of Transition-metal Doped Indium Oxide Nanocrystals:*

Small angle X-ray scattering (SAXS) analysis was done on a lab-scale SAXS (SAXSess, Anton Paar, Austria). The system was attached to an X-ray generator equipped with a X-ray tube (Cu Kα X-rays with wavelength $\lambda$ = 0.154 nm) operating at 40 kV and 50 mA. The raw data was processed with SAXSquant software (version 2.0), and scattering curves were averaged over 50 individual acquisitions for various acquisition times (.5-10s). Curve fitting was done using Irena macros for IGOR (V. 6.3).[94]

Transmission electron microscopy (TEM) images and electron diffraction patterns were collected on 400 mesh Cu grids (Ted Pella, Redding, CA) using a Tecnai Spirit TEM (FEI, Hillsboro, OR) operating at 120 kV. Samples were prepared by dipping the grid into a dilute solution of particles. Images were analyzed using ImageJ software.[95]

Elemental compositions of the nanocrystal cores were determined using a Teledyne Leeman Labs (Hudson, NH) Prodigy High Dispersion Inductively Coupled Plasma Optical Emission Spectrometer (ICP-OES). Nanocrystals were dried and digested in stock nitric acid for at least 48 hrs before being diluted for analysis. Surface composition by X-ray

photoelectron spectroscopy (XPS) was acquired using a Thermo Scientific ESCALAB 250 X-ray photoelectron spectrometer. Samples were prepared by drop-casting a hexane solution of nanocrystals on mica substrates.

X-ray diffraction (XRD) was carried out on a Rigaku Smartlab instrument using Bragg Brentano geometry and Cu Kα radiation. A step size of 0.01° and collection speed of 0.1 degrees/min was utilized over a range of 20-70 2θ. Rietveld refinement was conducted on the collected patterns using Fullprof Suite.[71]

Optical absorbance data was collected with a Perkin Elmer (Waltham, MA) Lambda 1050 UV/Vis/NIR Spectrometer. Samples were dispersed in hexanes and data were collected at room temperature.

Fourier-transform infrared (FTIR) spectra on the nanocrystals were obtained using a Thermo Fisher Nicolet 6700 spectrometer. Samples were deposited form a hexanes solution and pressed into a KBr pellet.

*Synthesis of Transition-metal Doped-Indium Oxide Nanocrystals:*

Samples were prepared as described previously.[56] One mmol metal carboxylate solutions were prepared by mixing indium(III) acetate and the appropriate metal dopant salt with 2 mL of oleic acid in a 20 mL glass scintillation vial. The vial was then heated to 150°C in an oil bath under $N_2$ for at least one hour to generate a metal-oleate precursor solution. For the Fe doped precursor, the solution was allowed to sit at 190°C for at least an hour. The as-prepared precursor solution was added dropwise (0.35 mL/min) to a three-neck 100 mL flask containing 13 mL of oleyl alcohol heated to 290°C. The precursor solution was added using a syringe pump fitted with a 20 mL syringe. During addition, $N_2$

37

was flowing through the flask at a rate of 120-130 cc/min. All three necks of the flask were capped with septa, and three 16-gauge purge needles were placed in one of the necks with a small amount of Kimwipe in the purge needles to prevent water reintroduction into the flask.

After synthesis, the nanocrystal solution was allowed to sit at reaction temperature for 5 minutes under $N_2$ flow, after which the solution cooled to room temperature. To isolate the nanocrystals, 30 mL of ethanol was added to precipitate the nanocrystals. The nanocrystals were isolated by centrifugation at 7300 rpm for 10 minutes. The product was washed twice more with ethanol and collected by centrifugation. The washed nanocrystals were then dispersed in hexanes. The solution of nanocrystals was then centrifuged at 7000 rpm for one minute to remove any insoluble material. After purification, typical yield of doped nanocrystal was > 100 mg (~90% yield).

**Bridge to Chapter III**

The continuous addition synthesis allows for stoichiometric dopant incorporation, with the dopant concentrations easily tuned and controlled in through the precursor composition. The slow, layer-by-layer growth of the nanocrystals allows for the dopant atoms incorporate and remain homogeneously distributed. This control over dopant incorporation, as well as control over nanocrystal growth, allows for the systematic study of size-property relationships of doped-metal oxide nanocrystals. Chapter III demonstrates this approach with Sn-doped $In_2O_3$, and correlates the nanocrystal size to the optoelectronic properties. The study demonstrates the first example of size tuning for Sn-doped $In_2O_3$ nanocrystals, where all sizes are produced from a single continuous reaction, and the dopant incorporation is stoichiometric and homogeneously distributed across the size series.

CHAPTER III


THE INFLUENCE OF NANOCRYSTAL SIZE ON OPTOELECTRONIC

PROPERTIES OF THIN, SOLUTION CAST Sn-DOPED In$_2$O$_3$ FILMS


This chapter will be published in the forthcoming publication co-authored with Adam W, Jansons, Kristopher M. Koskela, Meredith C. Sharps, Darren W. Johnson, and James E. Hutchison. I am the primary author and lead scientist on experimental data collection and analysis.

**Introduction**

Transparent conducting oxides (TCOs) are vital as thin film electrode materials for many modern electronic devices such as flat panel displays, touch screens, solar cells, and energy efficient windows.[1–6] Commercially available TCO thin films are produced via vacuum deposition, which currently yields the best combination of electrical, optical, and physical properties.[7–10] However, vacuum deposition suffers from several limitations: over 70% of the deposition source is wasted because it is deposited onto the chamber walls,[2,11] vacuum-deposited TCOs are brittle and incompatible with electronics that are flexible, stretchable, and wearable,[12–15] and the deposition conditions can damage soft optoelectronic materials such as perovskites used in solar cells.[16–18] Solution processing is a promising approach to address these limitations while reducing processing costs and increasing substrate compatibility. This approach is adaptable to industrial roll-to-roll production and inkjet processing, compatible with hard and soft substrates, and employable in direct-write applications that eliminate the need for lithographic patterning. Such

processes can reduce manufacturing costs and eliminate waste.[11,19–21] Solution processed TCO films have been successfully produced via several approaches including sol-gels,[22–25] inorganic nanoclusters,[26,27] and colloidal nanocrystals.[7,28–30]

Colloidal nanocrystals are of particular interest for TCO thin films because, compared to other approaches, they contain relatively low carbon and salt contamination, the films are fully crystalline upon deposition, and their surface chemistries can be made compatible with a variety of polar and nonpolar solvent systems. Although a number of studies have focused on altering ligand and surface chemistry of the TCO nanocrystals to improve thin film electronic properties, it is not clear how nanocrystal size affects thin film properties such as resistivity and optical transparency. Here, we investigate the influence of nanocrystal size on the optoelectronic properties of solution-processed thin films, using a series of colloidal Sn-doped $In_2O_3$ (ITO) nanocrystals all synthesized under the same reaction conditions, that are uniform and evenly doped across the series.

Low thin film resistivity and high optical transparency are the most important figures of merit for TCO materials. Although nanocrystal size may be expected to influence resulting TCO thin film properties, the dependence on nanocrystal size is relatively unexplored. A survey of the literature reveals only two studies examining the effects of size in ITO nanocrystals, the most commonly reported TCO nanocrystal system. Thin film resistivity was found to trend non-monotonically,[31] or show no correlation[32] with respect to nanocrystal size; no trends were reported on optical transparency. These findings contrast with those reported in the literature for semiconducting nanocrystals, where there is general agreement that an increase in nanocrystal size results in a decrease in film resistivity.[33–38] For semiconducting nanocrystals, the observed trend is attributed to a

synergy of multiple size-dependent factors such as: electron transfer activation energy, reduction of interfacial scattering boundaries, packing density, surface charge distribution, and capacitive charging. These size-dependent factors should also apply to TCO nanocrystals.

Although there are no quantitative size comparisons in the TCO nanocrystal literature, there are a number of reports describing solution-processed, colloidal ITO nanocrystal thin films. We compiled results from 13 of the most-cited ITO nanocrystal thin film studies and plotted the values reported for thin film resistivity as a function of nanocrystal size (Figure 3.1).
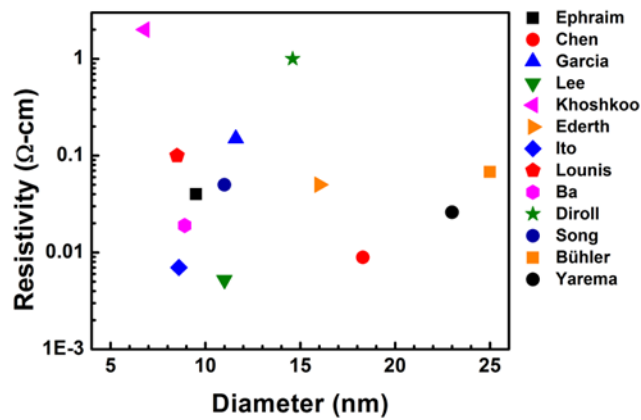


**Figure 3.1.** Thin film resistivity plotted as a function of nanocrystal diameter for ITO films reported in the literature. The plot shows no general correlation between nanocrystal diameter and thin film resistivity. Studies compared include Ephram et al.[39] (black square), Chen et al.[40] (red circle), Garcia et al.[41] (blue triangle), Lee et al.[42] (green triangle), Khoshkoo et al.[32] (pink triangle), Ederth et al.[8] (orange triangle), Ito et al.[43] (blue diamond), Lounis et al.[44] (red pentagon), Ba et al.[45] (pink hexagon), Diroll et al.[46] (green star), Song et al.[28] (blue circle), Bühler et al.[47] (orange square), and Yarema et al.[48] (black circle).

The results displayed in the figure suggest that there is no correlation between nanocrystal size and film resistivity. The resistivity values span three orders of magnitude for nanocrystals with diameters between 6 – 25 nm. For the narrower size window around 10 nm, a relatively common size, there is more than an order of magnitude spread in the

resistivity data. The unexpected spread in the data may be the result of the differences in synthetic approaches and parameters used to form the nanocrystals. In the studies from Figure 3.1, nanocrystals were synthesized over a wide range of temperatures (200 to 320 °C), and using metal precursors (carboxylates,[32,46] halides,[39–42,44] and alkoxides[28,43,45]) with distinctly different reactivities. Additionally, metal-oxygen bond formation was induced from a variety of chemical mechanisms including thermal decomposition,[39,41–44,46,48] precipitation under basic conditions,[40,47] and condensation pathways such as amidification.[28,32] The synthetic variations used to produce the nanocrystals in Figure 3.1 affect properties such as nanocrystal size, dopant incorporation, and surface chemistry in non-trivial ways. Thus, it is currently impossible to make comparisons and draw conclusions from the literature on size-property trends for the ITO nanocrystals.

The wide range of synthetic conditions used to prepare the nanocrystals in Figure 3.1 are also expected to impact the defect and dopant chemistry in the nanocrystals, from which all of the optoelectronic properties arise. In 2014, Lounis *et al.*[44] discovered that ITO nanocrystals synthesized from two literature methods displayed different dopant distributions and activations, resulting in an order of magnitude difference in thin film resistivity between the two samples. More recently, our group,[49] as well as Tandon,[50] and Zhou,[51] observed that nanocrystals with surface-segregated dopants display different optoelectronic properties compared to homogeneously-doped nanocrystals. Nanometer-scale dopant segregation within ITO nanocrystals determines the local electronic structure and ultimately influences intraparticle electron mobility as well as thin film resistivity, often by orders of magnitude. Dopant segregation has only recently been measured in nanocrystals, which raises questions about how varying dopant distribution may have

affected the observed materials properties in previous reports (such as many shown in Figure 3.1).

The development of a discrete size-ladder for TCO nanocrystals has not been demonstrated, because of several synthetic challenges. Although a few size-tunable syntheses for TCO NCs have been reported,[52–55] the examples cover a narrow range. Nanocrystal size is generally tuned through optimized synthetic adaptations in reaction temperature, surfactant identity, or precursor reactivity, which affect nanocrystal size in unintuitive and unpredictable ways. Additionally, changing synthetic variables as described also impacts the dopant distribution and defect chemistry, rendering direct size-property comparisons meaningless.

In order to elucidate size effects on TCO nanocrystal thin film properties (such as resistivity and optical transparency), a synthetic approach is needed that (*i*) produces a defined nanocrystal size ladder, (*ii*) utilizes the same reaction conditions for each nanocrystal size produced, (*iii*) produces a consistent level of defects, and (*iv*) incorporates dopant atoms uniformly at all sizes. To this end, we developed a continuous injection, living growth, low-temperature (< 300 °C) nanocrystal synthesis that utilizes the same chemistry during the production of all sizes, and produces nanocrystals with homogeneous doping at all sizes examined.

A series of seven Sn-doped $In_2O_3$ (ITO) nanocrystal samples from 5 – 21 nm in diameter are synthesized consecutively in this manner. The doping levels and distributions confirmed to be constant and homogeneous, respectively. The nanocrystals are soluble (> 100 mg/mL) in organic solvents, and the dispersions are shelf stable for over 1 year. The nanocrystal dispersions can be solution processed into smooth, crack-free thin films at all

sizes produced, the insulating ligands can be removed in situ, and the impacts of nanocrystal size on thin film optoelectronic properties are demonstrated.

**Results and Discussion**

*Synthesis and Characterization of Sn-Doped In$_2$O$_3$ Nanocrystals*

To investigate the influence of nanocrystal size on thin film resistivity, a series of ITO nanocrystals were designed and prepared. Once synthesized, the size, size uniformity, doping level and dopant distribution were all analyzed to ensure that each sample has the desired composition and structure. The nanocrystals were then analyzed optically to determine their carrier concentrations. Next, uniform thin films of the nanocrystal dispersions were deposited, the insulating organic capping ligands removed, and the films annealed. Lastly, the thin films were optically and electrically characterized and compared across the series.

The ITO nanocrystals are synthesized through a slow-injection, metal-catalyzed esterification reaction.[49,56,57] A mixture of indium/tin oleate precursor (9:1 In:Sn, 12 mmol total) containing a six-fold molar excess of oleic acid was slowly injected (18 mL/min) into oleyl alcohol held at 290 °C. The reaction, shown in Scheme 3.1, proceeds in three steps: (1) the injected metal oleate precursor reacts with the oleyl alcohol to produce ester and metal hydroxide species, (2) metal hydroxides condense to form the metal oxide nanocrystals, (3) additional metal oleate precursor is added continuously allowing the nanocrystal growth to continue. Because the reaction proceeds by a continuous growth process, aliquots taken periodically during the reaction represent different core sizes. Seven samples, taken at different reaction times, comprise the nanocrystal size ladder. Nanocrystal samples were purified through anti-solvent precipitation, centrifugation, and

dispersion in a nonpolar solvent such as toluene. This process was repeated several times to remove any impurities or unreacted starting material. All seven of the nanocrystal dispersions are a deep blue in color, indicating the incorporation of $Sn^{4+}$ into the oxide lattice and the filling of the $In_2O_3$ conduction band with free electrons.[58–60] The colloidal solutions are shelf stable for over a year.

**Scheme 3.1.** Reaction mechanism for nanocrystal growth proceeds through a metal-catalyzed esterification and subsequent metal-hydroxo condensation. Continuous addition of a metal carboxylate facilitates nanocrystal growth through additional surface condensation.
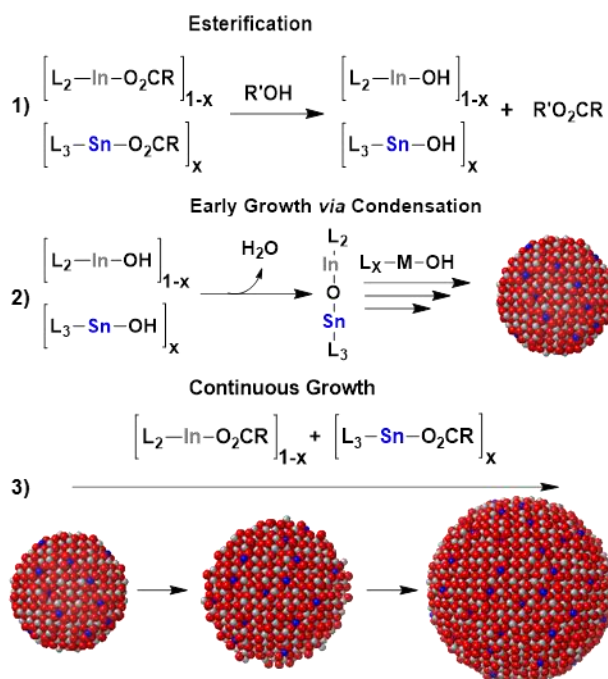


Figure 3.2a-d displays TEM micrographs of the ITO nanocrystals. Each of the nanocrystals within the size ladder are single crystalline (evidenced by the lack of visible grain boundaries), uniform in size, and readily pack into extended arrays on the TEM grid. Powder XRD confirmed that the crystalline phase is cubic bixbyite $In_2O_3$ (ESI Figure B1), with no segregated $SnO_x$ phases present. The core diameter and size dispersity of purified

samples were analyzed *via* Small Angle X-Ray Scattering (SAXS), with the results plotted

against amount of precursor added in Figure 3.2e. The nanocrystal sizes range from 5.3 nm

to 21.5 nm in diameter, and exhibit low dispersities, ~ 15% for the 5.3 nm sample and <

10% for all samples greater than 10 nm (Figure 3.2e). The nanocrystal volumes were

calculated from the measured sizes and plotted versus amount of precursor added in Figure

3.2f. There is a linear correlation between nanocrystal volume and the amount of metal

oleate precursor added, indicating that the growth of the ITO nanocrystals is living.[56,61,62]
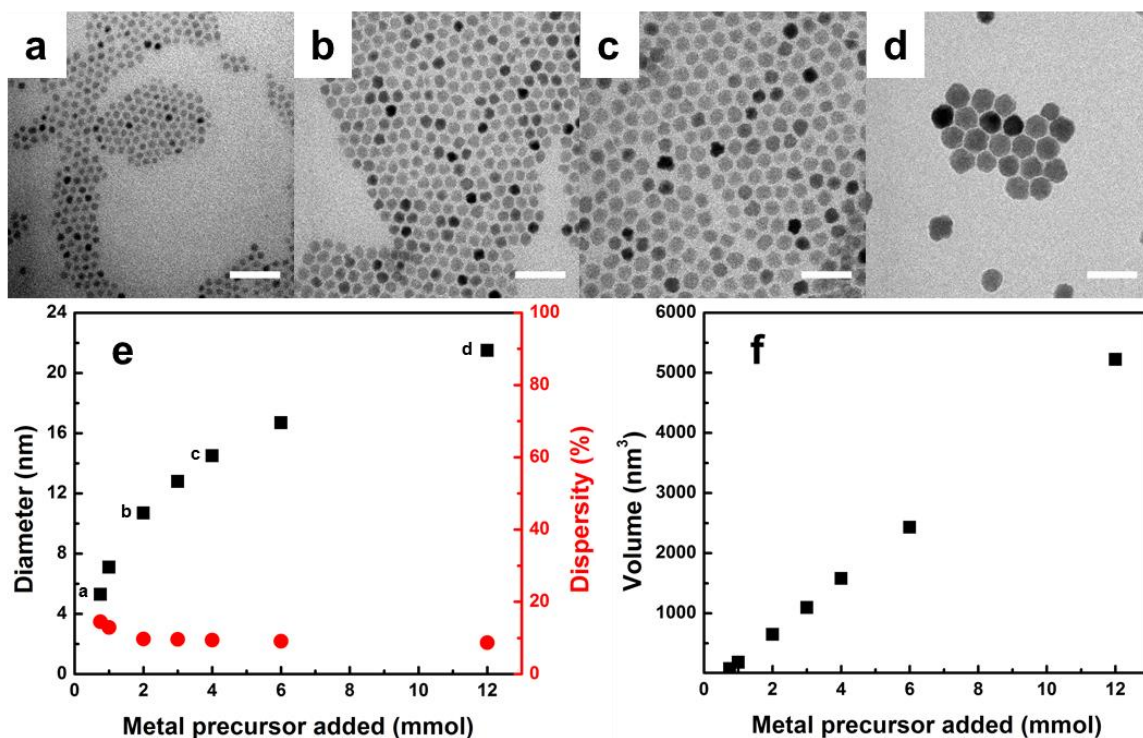
**Figure 3.2.** TEM micrographs and growth curves for the ITO nanocrystals within the size ladder, produced from one reaction pot, with growth proceeding linearly with volume added. TEM micrographs show nanocrystals with diameters of (a) 5.3 nm, (b) 10.7 nm, (c) 14,5 nm, and (d) 21.5 nm. Scale bars are 50 nm. Nanocrystal growth curve (e) plots diameter versus amount of precursor added. The nanocrystal diameter (black squares) and dispersity (red circles) were measured by SAXS. Nanocrystal volume (calculated from the diameter measurements) plotted versus the amount of precursor added (f).

The atomic compositions and dopant distribution profiles of the nanocrystals were analyzed using a previously reported approach[44,49] to probe both absolute and surface dopant concentrations. Reports have shown that dopant distribution profiles have profound impacts on nanocrystal optoelectronic properties,[29,44,49,53,63] and dopant distribution can affect thin film resistivity by over an order of magnitude;[44] therefore it is imperative to determine the nanocrystals' dopant distribution profiles and ensure that they are consistent across the series to be examined. The absolute dopant concentration was determined *via*

inductively-coupled plasma optical emission spectroscopy (ICP-OES) performed on a small sample of each nanocrystal digested in HCl. The results for the absolute Sn atomic % (relative to total metal) are shown in Table 3.2. The surface dopant concentration was determined *via* X-Ray photoelectron spectroscopy (XPS) performed on a dropcast sample for each size, and reported as % Sn relative to total metal content in Table 3.2.

**Table 3.1.** Bulk and surface dopant concentrations (Sn %) determined by ICP-OES and XPS, respectively. The feed ratio was determined by the ratio of In:Sn oleate used in the injected precursor. The fact that both ICP-OES and XPS (which measures the nanocrystal bulk and surface Sn concentrations, respectively) agree with the feed ratio suggests that doping is stoichiometric and homogeneously distributed.

| Size | | Sn % | |
| --- | --- | --- | --- |
| (nm) | Feed ratio* | ICP-OES | XPS |
| 5.3 | 10.0 | $9.8 \pm 0.1$ | $10.0 \pm 0.7$ |
| 7.1 | 10.0 | $10.2 \pm 0.1$ | $9.9 \pm 0.7$ |
| 10.7 | 10.0 | $10.7 \pm 0.1$ | $10.2 \pm 0.3$ |
| 12.8 | 10.0 | $10.6 \pm 0.1$ | $10.1 \pm 0.7$ |
| 14.5 | 10.0 | $10.1 \pm 0.1$ | $10.3 \pm 0.4$ |
| 16.7 | 10.0 | $9.9 \pm 0.1$ | $10.4 \pm 0.5$ |
| 21.5 | 10.0 | $10.4 \pm 0.1$ | $10.8 \pm 0.5$ |

The XPS analysis probes the surface atomic composition to a depth of ~3-4 nm in the $In_2O_3$ lattice.[44,49] By comparing the ICP-OES and XPS data, the local distribution of dopant atoms can be deduced. From the data shown in Table 3.2, the bulk Sn atomic % measured from ICP-OES is in agreement with the surface Sn atomic % measured by XPS, as well as the feed ratio at all sizes synthesized. This agreement between the ICP-OES and XPS measurements, as well as with the feed ratio, indicates that the nanocrystals stoichiometric and homogeneous doping at all sizes. Therefore, the optoelectronic

properties of prepared thin films from this series will not the result of inhomogeneous doping.

TCO nanocrystals require a high carrier concentration to be electrically conductive. We also need to ensure the carrier concentrations are consistent across the series so that when thin film resistivities are compared, only the effects of size are being observed. Carrier concentration in TCO nanocrystals can be determined optically from the localized surface plasmon resonance (LSPR) frequency in their NIR spectra using the relationship in Equation 1:

$$\omega_p = \sqrt{\frac{N_e e^2}{m^* \varepsilon_o}} \qquad\qquad (1)$$

where $\omega_p$ is the bulk plasma frequency, $Ne$ is the free carrier concentration, $e$ is the elementary charge, $m^*$ is the effective mass, and $\varepsilon_o$ is the permittivity of free space. The NIR spectra are shown in Figure 3.3a.
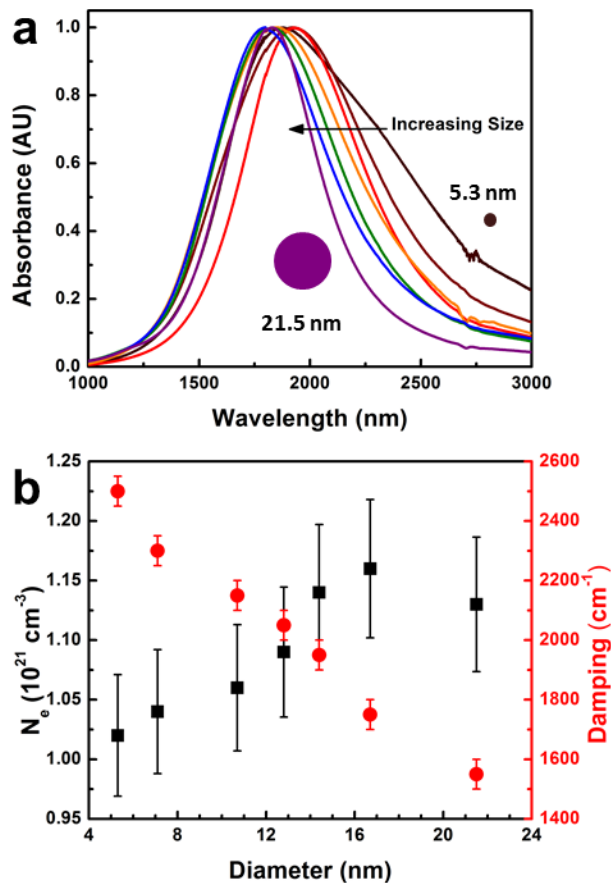
**Figure 3.3**. NIR spectra of ITO nanocrystals, and the free electron concentrations and damping values extracted from the NIR spectra. The NIR spectra (a) show a blue shift in the LSPR and a decrease in linewidth at increasing nanocrystal sizes. Plot (b) shows that the free electron concentration increases with an increase in nanocrystal diameter, while damping decreases. Error bars are taken from the fitting parameters.

The LSPR peaks in Figure 3.3a shift to shorter wavelengths (blue shift) and decrease in linewidth as nanocrystal size increases. Because the elemental composition and dopant distributions are equivalent across the series (Table 3.2), the observed spectral changes can be attributed to size alone. The blue shift in the LSPR suggests an increase in carrier concentration (Equation 1), whereas the decrease in linewidth indicates a decrease in LSPR damping.[64,65] The spectra can be analyzed with the Drude model to extract the

carrier concentration and LSPR damping values,[44,49,66] (see ESI for an example analysis). The carrier concentrations and damping values for the LSPR spectra are plotted versus nanocrystal diameter in Figure 3.3b. The carrier concentrations increase by about 10% as nanocrystal diameter increases, and the damping values decrease by 1000 cm$^{-1}$. Both of these trends are consistent with the spectral shifts and peak width changes seen in Figure 3.3a.

The observed increase in carrier concentration and decrease in damping can both be attributed to geometric factors. Similar effects have been recently reported for Cr/Sn doped In$_2$O$_3$ by Tandon et al.[50] The decreased surface area-to-volume ratio found at larger nanocrystal dimensions reduces the number of dopant atoms that are in inactive trap states at the surface and less damping of the LSPR through scattering of electrons by dopant atoms near the surface. The lower percentage of Sn atoms at the surface, relative to those in the core, results in a greater percentage of Sn atoms contributing electrons to the In$_2$O$_3$ conduction band, and at sufficiently large sizes the carrier concentration will plateau. Damping has been previously shown to be a strong indicator for electrical performance for doped In$_2$O$_3$ nanocrystal thin films, with decreases in plasmonic damping correlating with significant increases in electron mobility[53] and reduction in thin film resistivity.[44] Reducing LSPR damping is a fundamental design criteria for TCO nanocrystal thin films, and we hypothesize that the larger nanocrystals will exhibit significant decrease in thin film resistivity.

*Preparation and Analysis of Sn-Doped In$_2$O$_3$ Nanocrystalline Thin Films.*

The oleate ligands that cap the surface of the nanocrystals introduce significant insulating barriers between the nanocrystals, thus, removing the ligands is crucial to

improving electronic conduction. Thermogravimetric analysis (TGA) of our nanocrystal samples (ESI Figure B2) confirmed that all ligands are lost by 400 °C. This processing temperature is too high to be compatible temperature-sensitive materials. A lower temperature ($\leq$ 300 °C) is typically desired, especially for soft substrates. To adapt these fatty-acid stabilized nanocrystals for lower temperature processing, we tried an *in situ* ligand exchange with formate ligands, previously demonstrated by Zarghami[67] for thin films of PbS or $Fe_2O_3$ nanocrystals. A dispersion of 10 mg of ITO nanocrystals (12.8 nm) dissolved in 1 mL of hexanes was added to a 1 M solution of formic acid in acetonitrile, leading to rapid precipitation of the nanocrystals. TGA analysis of the precipitate showed that all mass was lost by 300 °C (Figure B2), indicating that the ligand exchange was successful and suggesting this method will be useful for the nanocrystals in this study.

Thin film samples were prepared with oleic acid-stabilized ITO nanocrystal dispersions (50 mg/mL in toluene) deposited *via* spin-coating. IR-transparent Si substrates were used so that the ligand exchange could be monitored *via* FT-IR. The thin films were soaked in a 1M formic acid/acetonitrile solution for the ligand exchange. FTIR spectra (shown in Figure 3.4a) were taken periodically to monitor the ligand exchange. The oleate ligand C-H stretches absorb prominently at 2925 $cm^{-1}$ and 2850 $cm^{-1}$ in the as-deposited films (Figure 3.4a black trace). A reduction in the intensity for the C-H stretches was observed upon soaking in the formic acid solution, indicating the ligand exchange was successful (Figure 3.4a inset). Beyond 60 minutes there was no further reduction in ligand C-H intensity. Similar results were also found for the 5.3 nm and 21.5 nm samples. All samples used for evaluation of the thin film properties were ligand exchanged for 60 minutes using this approach.
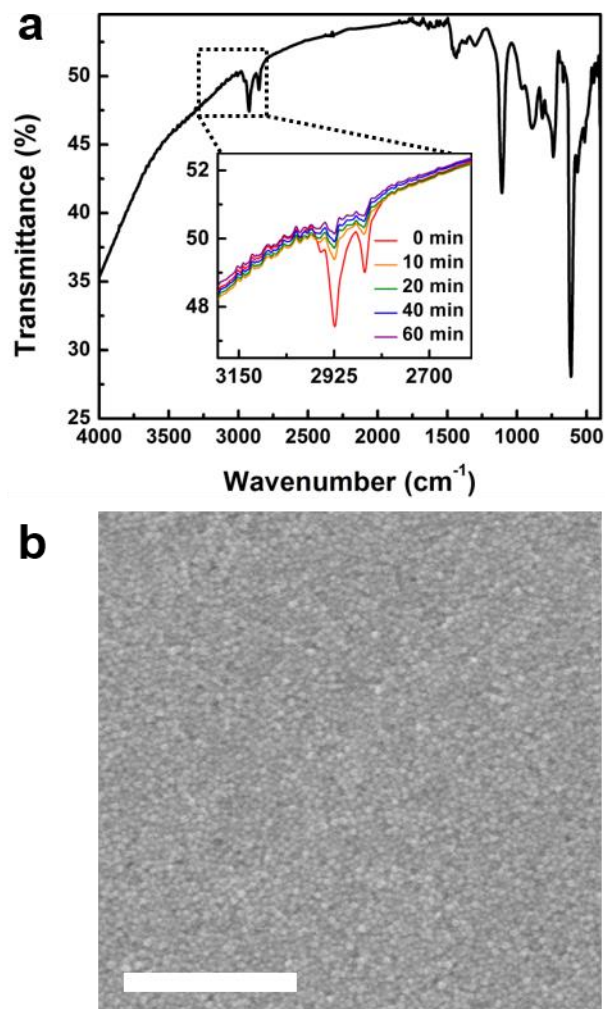
**Figure 3.4.** Monitoring ligand exchange of oleate ligands with formic acid and film annealing *via* FT-IR and SEM analyses. FT-IR spectra (a) of ITO nanocrystal thin films shows decrease in oleate C-H stretches over time as ligand exchange progresses. SEM micrograph (b) of the nanocrystal film surface after formic acid exchange illustrating the film is uniform, and crack- and defect-free, scale bar is 500 nm.

After ligand exchange, thin films were annealed under a reducing atmosphere of

5:95 $H_2$:$N_2$ mixture[9,42] at 300 °C for 1 h to 6 h to remove remaining organic material from

the film. The temperature was selected based upon the TGA collected in Figure B2. FTIR

spectra were taken during the annealing process (ESI Figure B3) to determine the length

of the annealing period. Upon annealing for 1 h, the plasmon shifts to approximately 3200

54

cm$^{-1}$. The shift in the plasmon suggests increased electron correlation between the nanocrystals in the film,[41] indicating the free electrons are no longer localized to individual nanocrystals and should conduct well. The plasmon remains relatively unchanged for annealing times from one hour up to six hours. Thus, all samples for subsequent analysis were annealed for one hour.

The surfaces of the thin films were examined with scanning electron microscopy (SEM) to look for any defects such as voids and cracks that may have been induced by the ligand exchange and annealing processes. A representative top-down SEM micrograph is shown in Figure 3.4b, revealing the film to be void and crack-free over an area greater than 1 μm$^2$ after the processing steps were performed.

Nanocrystal thin films were prepared for each size reported earlier from 5.3 to 21.5 nm on 2 x 2 cm glass slides for cross-sectional SEM analysis and UV-Vis transmittance measurements. Each sample was ligand exchanged and annealed as previously described. To determine film thicknesses, cross-sectional images were taken with SEM. Figure 3.5a, 5b, and 5c, show the results for the nanocrystals with diameters 5.3 nm, 12.8 nm, and 21.5 nm, respectively. The thin films are approximately 150 nm thick for each of these three samples. Individual nanocrystals can be resolved in the SEM images and are about the size expected, indicating that there is not significant sintering of the nanocrystals during the thermal processing. Additionally, the thin films are smooth and void of defects after ligand exchange and thermal processing. Figure 3.5d displays the UV-Vis spectra for the samples shown in Figure 3.5a - 5c. The nanocrystal films display greater than 90% transmittance from 450 – 900 nm compared to the bare glass substrates (Figure 3.5d), and the transmittances are comparable to vacuum deposited films. These films have transmittance

that is comparable to vacuum deposited films.[7–10] Although there is a slight decrease in transmittance in the 325 – 600 nm range with the larger nanocrystals, the 21.5 nm nanocrystals still transmit ~ 95 % relative to the glass substrate.
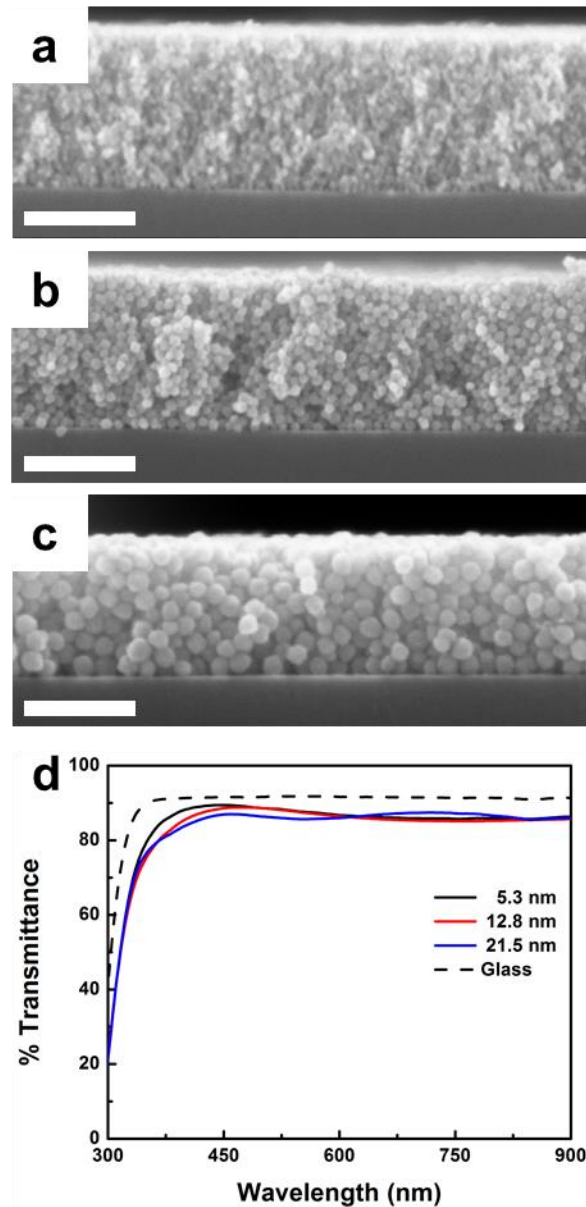


**Figure 3.5.** SEM film cross-sections and UV-Vis spectra for nanocrystal thin films highlighting thin film morphology and optical transmittance with respect to diameter. SEM film cross-sections for (a) 5.3 nm, (b) 12.8 nm, and (c) 21.5 nm samples, illustrating that the thin films are smooth and crack-free; scale bars are 100 nm. Individual nanocrystals can be resolved, indicating there is little to no sintering of the nanocrystals during thermal

treatment. UV-Vis spectra of the nanocrystal thin films (d) from sample sizes of (black) 5.3 nm, (red) 12.8 nm, and (blue) 21.5 nm, along with the $SiO_2$ substrate (dashed). The nanocrystal thin films display transmittance > 95% for all samples.

Three thin film samples were prepared for each nanocrystal size in the series. After deposition on $SiO_2$/Si substrates, the ligands were removed by formic acid ligand exchange and each sample annealed as described above. I-V measurements were taken with a 4-pt probe. The resistivity values were calculated from the linear I-V curves and the film thicknesses as measured by cross-sectional SEM. Resistivity values are plotted as a function of nanocrystal diameter in Figure 3.6a.
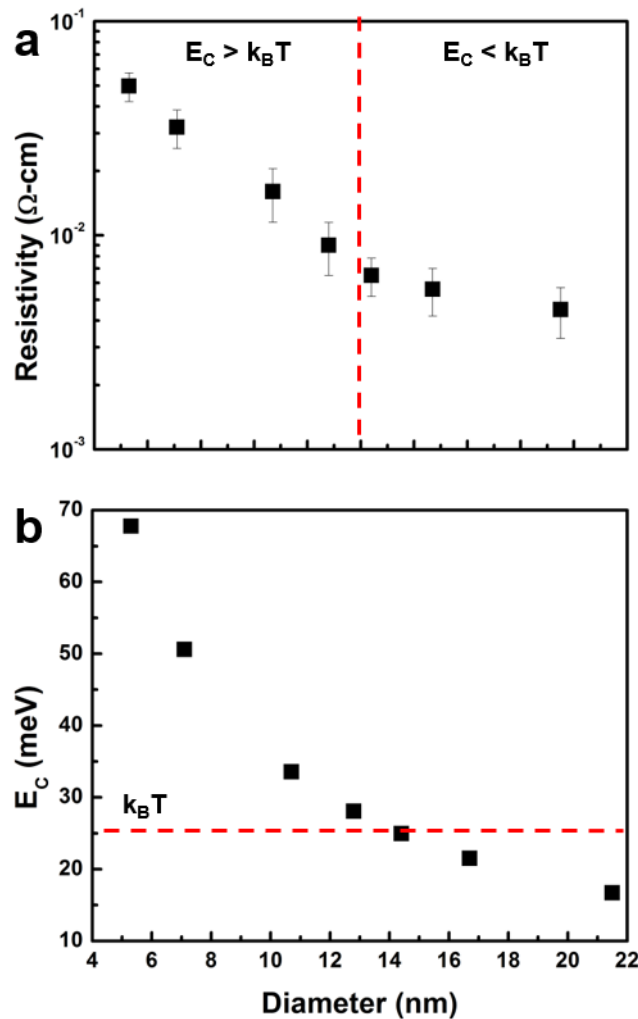
**Figure 3.6.** Thin film resistivity and nanocrystal coulombic charging energy ($E_C$) plotted versus nanocrystal diameter. Thin film resistivity (a) is shown to decrease as nanocrystal size increases, error bars are the standard deviation from three samples for each diameter. $E_C$ values (b) are calculated from Equation 3 and are inversely proportional to nanocrystal diameter.

Figure 3.6a displays a decrease in thin film resistivity as nanocrystal size increases. In fact, resistivity drops by an order of magnitude between the 5.3 nm and the 21.5 nm samples, from $5.0 \cdot 10^{-2}$ Ω-cm to $4.5 \cdot 10^{-3}$ Ω-cm, respectively. Interestingly, there seem to be two linear regions in Figure 3.6a that intersect at around 14 nm. Electronic conduction through nanocrystalline media is well known to proceed through an activated hopping process.[36,37,68–70] Therefore, the decrease in resistivity shown in Figure 3.6 reflects a decrease in the activation energy required for electron hopping, and the two separate linear regions from Figure 3.6 may have different size-dependencies for their activation energies.

The activation energy is a combination of many factors including spacing between hopping sites (generally determined by ligand length), electronic coupling energy between adjacent nanocrystals, coulombic charging, and the density of barriers present in the nanocrystalline film.[36,37,68] Electronic coupling energy is generally low relative to $k_B T$,[36] with coulombic charging and grain boundary density presenting the largest energy barriers to electronic conduction.[31,37,69,71] The relationship between coulombic charging ($E_C$) and nanocrystal diameter ($d$) is given by Equation 3[36,68,71,72]

$$E_C = \frac{e^2}{2\pi \varepsilon_m \varepsilon_o d} \tag{3}$$

where $e$ is the elementary charge, $\varepsilon_m$ is the dielectric constant of ITO (4),[49] and $\varepsilon_o$ is the permittivity of free space. Figure 3.6b shows the calculated values for $E_C$ for the

nanocrystal series. Interestingly, above approximately 14 nm in diameter $E_C$ is larger than

$k_BT$ at room temperature (25.7 meV), indicating that for sizes above 14 nm there is

sufficient thermal energy to overcome the energetic cost of coulombic charging.[35–37,68] This

is likely the cause for the two linear regions in Figure 3.6a; above 14 nm, film resistivity is

no longer dictated by $E_C$ and thus the rate of decrease for resistivity with respect to size

lowers. Thus, a key strategy to enhance conductivity in ITO nanocrystal thin films is to

employ nanocrystals larger than 14 nm to avoid the coulombic charging barrier. Above 14

nm the thin film resistivity continues to marginally decrease, and this must be due to other

factors such as grain boundary scattering and barrier density.

The other major component in the activation energy to electronic conduction is

grain boundary scattering,[73–76] and the literature suggests that reducing the grain boundary

density (and thus the interface density) increases electron mobility and lowers thin film

resistivity. While it is not viable to explicitly measure interface density and scattering

within a film, we can measure the packing densities of the nanocrystal thin film using

ellopsometry.[42] The calculated packing densities can then be compared with known

packing geometries and their average coordination numbers; this comparison can yield an

average range for interface density as a function of nanocrystal size. First, to calculate the

packing densities, the refractive indices of the nanocrystalline thin films were measured

from ellipsometry. The packing densies were then calculated[42] and plotted in Figure 3.7a.
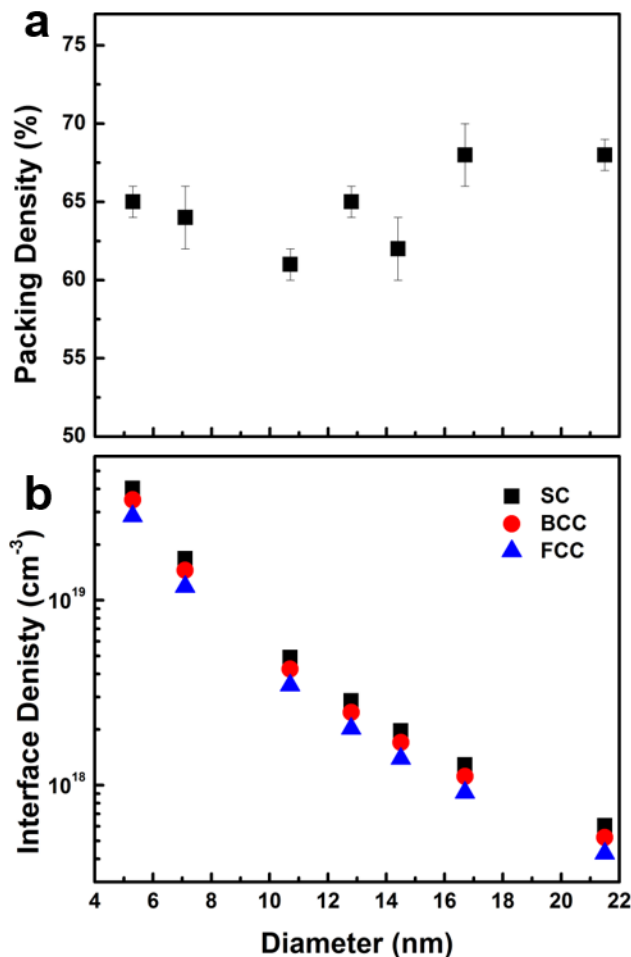
**Figure 3.7.** Packing densities of the nanocrystals (a) were determined *via* ellipsometry and plotted with respect to nanocrystal diameter. All nanocrystal sizes exhibit packing densities between 60–70%, in agreement with randomly-packed spheres. Calculated interface densities (b) plotted against nanocrystal diameter, using common sphere packing geometries of simple cubic (SC, black squares), body centered cubic (BCC, red circles), and face centered cubic (FCC, blue triangles). Grain boundary density is calculated to decrease exponentially with respect to nanocrystal size, regardless of packing efficiency or coordination number.

A slight increase (~3%) in packing is observed from the smallest to the largest nanocrystals, however all of the packing density values fall between 60 and 70%, which is the generally accepted range for randomly packed spheres.[77–81] Comparisons of the data in Figure 3.7 with other known packing geometries can give better insight into the range of

interface densities present in the nanocrystalline films. For close packed systems, the interface density can be calculated using the unit cell dimensions and coordination number (see ESI for example calculation).

Figure 3.7b plots the calculated interface densities of common close-packed geometries with respect to the nanocrystal diameters of the size series. Interestingly, interface density doesn't strongly depend on packing geometry, but significantly depends upon nanocrystal size. The effects of interface density reduction on thin film resistivity can be observed without the coulombic influence by examining the data from Figure 3.6 where $E_C$ is below $k_BT$. The resistivity trend continues to decrease at the larger nanocrystal sizes, albeit at a slower rate. This gives evidence that $E_C$ is the larger contributor to the activation energy, but both $E_C$ and the interface density minimization are required for future improvements in thin film performance.

**Conclusions**

We have shown that ITO nanocrystals can be synthesized, utilizing the same chemical pathway, over a size range of 5 – 21 nm through a layer-by-layer continuous growth method. Seven different nanocrystal sizes were produced from the same reaction, and the nanocrystals exhibit dopant incorporation that is stoichiometric and homogeneously distributed at all sizes produced. The nanocrystals were solution deposited into smooth, defect free films, and displayed high transmittance (> 95%) with respect to $SiO_2$ at all nanocrystal sizes. The thin films were ligand exchanged in situ in order to reduce thermal treatment requirements. Thin film resistivity was found to decrease by an order of magnitude as nanocrystal size increased from 5.3 to 21.5 nm in diameter.

We concluded that the observed decrease in thin film resistivity with increasing nanocrystal size is attributed to several, size-dependent factors including a reduction in coulombic charging energy ($E_C$), a reduction in plasmonic damping (which is related to intraparticle electron mobility), and a reduction in interface density. The trends observed indicate that for nanocrystals below 14 nm in diameter, a reduction in $E_C$ had the largest influence on reducing resistivity. For all sizes above 14 nm in diameter, $E_C$ was calculated to be above $k_BT$ and was no longer influential in the size-resistivity correlation. However, at the sizes above 14 nm, marginal gains in electrical performance were still present, and were due to the reduction in interface density as nanocrystal diameter is increased. Interestingly, resistivities comparable to the lowest values reported herein have been achieved at nanocrystal size below 14 nm,[42,43] indicating that additional activation energies aside from $E_C$ can be minimized to enhance thin film performance. The literature currently suggests that the activation barrier to electron transfer between oxide nanocrystals can also be lowered through defect engineering,[53] dopant distribution,[44] and tuning surface depletion widths.[29] Coupling those strategies with size control (to minimize interface density and $E_C$) should enable TCO nanocrystal thin film electrical properties to approach those of vacuum-deposited thin films.

**Materials and Methods**

*Materials*

Indium(III) acetate (99.99%), oleic acid (90% technical grade), and tin(IV) acetate were purchased from Sigma-Aldrich and used as received. Oleyl alcohol (80-85% technical

grade) was purchased from Alfa Aesar and used as received. A flow meter purchased from Cole-Parmer was used to monitor nitrogen flow.

*Synthesis of Indium Oxide Nanocrystals*

The synthesis followed a similar procedure as reported in literature.[49,56,57] A 10 molar percent Sn-doped Indium oleate solution was prepared by adding 0.075 mmol Sn(IV) acetate to 6.75 mmol In(III) acetate with 15 mL oleic acid. The solution was kept at 160 $^{\circ}$C for several hours under $N_2$ to produce a Sn-dopled indium oleate solution with a concentration of 0.5 mmol metal/mL oleic acid. The metal oleate solution obtained was then added dropwise to 13.0 mL of oleyl alcohol heated to 290 $^{\circ}$C in a 100.0 mL three-neck flask. The oleate solution was added using a 20 mL syringe and syringe pump at a rate of 0.35 mL/min. During addition, $N_2$ was flowing through the flask at a rate of 130 cc/min. All three necks of the flask were capped with septa, and three 16-gauge purge needles were placed in one of the necks to prevent pressure buildup.

For the synthesis of ITO NCs of varying size, various amount of precursor solution was added to the flask. For the synthesis of 5.3, 7.1, 10.7, 12.8, 14.4, 16.4, and 21.5 nm NCs, 0.75, 1, 2, 3, 4, 6, and 12 mmol of metal oleate solution was added, respectively. Excess oleyl alcohol (13 mL) was added dropwise to the reaction flask at a rate of 0.24 mL/min after half of the metal oleate solution had been added. After synthesis, the NCs were precipitated with 12 mL ethanol. The solid was collected by centrifugation (7300 rpm), dispersed in hexanes, and washed once more with 12 mL ethanol. The purification procedure was repeated two additional times.

*Characterization of Indium Oxide Nanocrystals*

Small-angle X-ray scattering (SAXS) analysis was done on a lab-scale SAXS (SAXSess, Anton Paar, Austria). The system was attached to an X-ray generator equipped with a X-ray tube (Cu Kα X-rays with wavelength λ = 0.154 nm) operating at 40 kV and 50 mA. The scattered X-ray intensities were measured with a charge-coupled device (CCD) detector (Roper Scientific, Germany). The raw data were processed with SAXSquant software (version 2.0). Scattering curves were averaged over 50 individual curves for various acquisition times (2-40s). Curve fitting was done using Irena macros for IGOR (V. 6.3).[82] The SAXS was calibrated to absolute intensity using 18.2 MΩ water as a standard. Transmission electron microscopy (TEM) images were collected on 400 mesh Cu grids (Ted Pella, Redding, CA) using a Tecnai Spirit TEM (FEI, Hillsboro, OR) operating at 120 kV. Samples were prepared by dropcasting a toluene solution directly onto a copper grid. Bulk elemental compositions the nanocrystal cores were determined using a Teledyne Leeman Labs (Hudson, NH) Prodigy High Dispersion Inductively Coupled Plasma Optical Emission Spectrometer (ICP-OES). Nanocrystals were dried and digested in stock HCl for at least 48 hrs before being diluted for analysis. Elemental composition for the surface of the nanoparticles was determined using a Thermo Scientific ESCALAB 250 X-ray Photoelectron Spectrometer (XPS). Samples were prepared by dropcasting a hexanes solution onto mica substrates. Surface tin content was determined by integrating the tin $3d_{5/2}$ peaks and comparing those intensities to those of the indium $3d_{5/2}$ peaks. Optical measurements were carried out on a PerkinElmer (Waltham, MA) Lambda 1050 UV/Vis/NIR Spectrometer. Spectra were collected in $CCl_4$ using only one detector (PbS) in order to remove most detector artifacts. Samples were diluted to a

concentration of ~0.5 mg/mL. Spectra were sampled from 1000 – 3300 nm with a scan resolution of 1 nm. Drude modeling was performed in MatLab. Models were fitted manually to simulated spectra, example shown in the ESI. Models were allowed to optimize to a least-squared fit, with extracted value errors of 25 cm$^{-1}$.

*Preparation and Characterization of ITO Nanocrystal Thin Films*

ITO NCs were dispersed in toluene, with a solution concentration of ~ 50 mg/mL. For substrates, (100) low resistivity Si was used. Prior to deposition, Si wafers were cut to 1.5 x 1.5 cm squares. A wet thermal oxide was grown to a thickness of ~ 500 nm. The wafers were rinsed with isopropanol and sonicated in isopropanol for 1 minute. The toluene NC solutions were spin coated onto the $SiO_2$/Si wafers @ 3000 rpm for 30 s. The wafers were then soft baked on a hot plate set to 250 ºC for 10s. The spin coat and soft bake procedure was repeated two more times. The resulting thin films were heated to 300 ºC in 30 mins, and held for 6 h under forming gas (5% $H_2$/ 95% $N_2$). Scanning electron microscopy (SEM) images were collected using a ZEISS Ultra-55 SEM operating at 30 kV. UV-Vis spectra of thin films were collected on a Perkin Elmer Lamda 1050 spectrometer, with the ITO NCs deposited on 2x2 cm glass slides. Ellipsometry data were taken on a J.C. Woollam M44 Spectroscopic Ellipsometer. Three separate films for each nanoparticle sample were spin coated onto silicon wafers with 100 nm of thermal oxide. The films were modeled as Cauchy films on 100 nm of $SiO_2$. The data were first fit to find thickness of each film. The thickness given by the model was then held constant while the optical constant was fit over the full wavelength range. The MSE was below 5 for all fits. The value of *n* at $\lambda$ = 555.7 was used in the equation to calculate the packing density. I-V measurements were performed with a 4-pt probe, on ITO samples deposited onto 2x2 cm

100 nm SiO2/Si substrates. Voltage was scanned from -100 to 100 mV, with the resistivity calculated from the linear I-V fits.

**Bridge to Chapter IV**

The continuous addition synthesis has been shown to allow for stoichiometric and homogeneously-distributing dopant incorporation (Chapter II), as well as simultaneous control over the nanocrystal size (Chapter III). The layer-by-layer growth yields the ability to control compositional gradients in the nanocrystal, where dopants are deliberately localized within the nanocrystal core or shell. This localization, or radial dopant distribution, can be altered simply by when the dopant precursor is introduced into the nanocrystal reaction during growth. This allows the ability to synthesize doped/undoped and undoped/doped core/shell nanocrystals, and to systematically investigate the radial dopant distribution on the optical properties, namely the plasmonic properties. The study reveals a strong influence of radial dopant distribution on the plasmonic energies, dopant activations, and overall damping of the system, which are discussed in Chapter 5. The study is the first example of tailoring plasmonic properties through deliberate radial dopant placement, and gives mechanistic insight into the effects of dopant localization on the plasmonic properties.

CHAPTER IV


RADIAL DOPANT PLACEMENT FOR TUNING PLASMONIC PROPERTIES IN

METAL OXIDE NANOCRYSTALS


This chapter was previously published as Crockett, B. M.; Jansons, A. W.; Koskela, K. M.;

Johnson, D. W.; Hutchison, J. E. Radial Dopant Placement for Tuning Plasmonic

Properties in Metal Oxide Nanocrystals. *ACS Nano* **2017**, *11* (8), 7719–7728. Copyright

2017 American Chemical Society.


**Introduction**

The unique properties of plasmonic nanomaterials allow their use in a variety of

applications, such as spectroscopy,[1,2] chemical sensing,[3–5] transparent conducting films,[6,7]

and as biomedical agents.[8–10] Recently, non-noble metal nanomaterials that display

localized surface plasmon resonances (LSPRs) in the infrared (IR) and near-IR (NIR)

region of the electromagnetic spectrum have been investigated, and their use explored as

active components in a variety of the above applications.[11–15] Several types of extrinsically-

doped oxide nanocrystals that display tunable LSPRs have been reported, including Sn-

doped $In_2O_3$ (ITO),[16–20] Ce-doped $In_2O_3$,[21] In or Al-doped ZnO,[22–24] In and F/In co-doped

CdO,[6,25,26] and Nb-doped $TiO_2$.[27] In these cases, the LSPR arises when dopant atoms and

crystalline defects contribute free electrons into the conduction band that collectively

oscillate when excited by their resonance frequency. In the case of metal oxides, the energy

of the LSPR can be tailored through changes in aliovalent dopant concentration or dopant identity.[14–16,26,28,29]

Recent reports suggest that the radial distribution of dopants in metal oxide nanocrystals may contribute to large variations in the plasmonic properties of these materials, specifically damping (which correlates to the LSPR linewidth)[14,30] and dopant activation (the number of free electrons per dopant cation).[31] Three example dopant architectures are shown in Figure 4.1.  Using ITO nanocrystals as a model system, Lounis *et al*. observed that the LSPR energy and shape depend upon the radial dopant distribution of Sn.[31] The authors suggest that mitigating dopant heterogeneity and size effects, as well as deliberate radial placement of dopant atoms would be a powerful strategy for designing plasmonic nanocrystal properties. Such an approach however, is difficult to impossible to achieve given the current state of colloidal nanocrystal syntheses. In order to gain access to such level of LSPR control, a synthetic approach is required that allows for sub-nanometer size and composition control during the growth phase, which would permit the logical production of advanced structures, including doped/undoped or undoped/doped core/shell architectures.
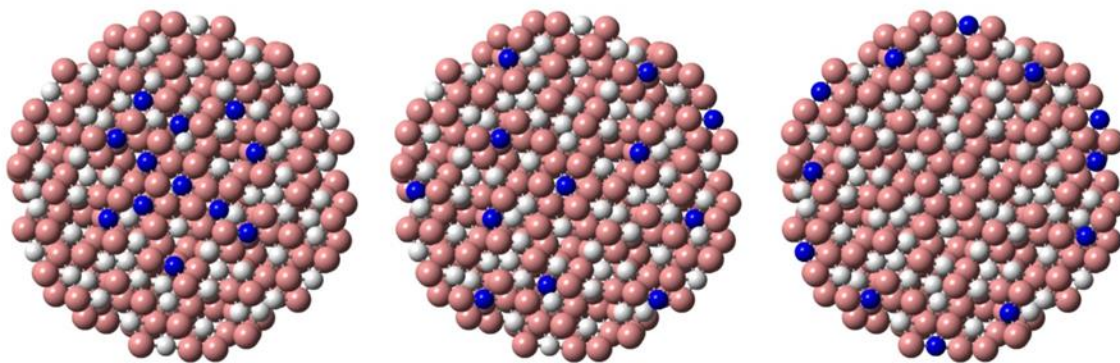


**Figure 4.1**. Schematic cross-section representations for three dopant distributions of Sn in an In$_2$O$_3$ nanocrystal. Sn localized in the core (left), Sn homogeneously doped (middle), and Sn localized towards the surface (right). Oxygen, indium, and tin atoms are red, white,

and blue spheres respectively. Schematics were generated in CrystalMaker using a bixbyite $In_2O_3$ lattice.

Recently, we reported a synthesis for both binary and doped metal oxide nanocrystals based upon esterification of metal oleates in long-chain alcohol solution that has the potential for deliberate and precise radial control over dopant placement.[32–34] During *slow* addition of a metal carboxylate into long-chain alcohol at elevated temperatures (> 200 °C), metal oxide particles nucleate and then grow continuously without coalescence, ripening, or forming additional particles. The synthesis proceeds with > 90 % yield and can provide gram-scale material.[33] This approach proceeds through a living or continuous growth mechanism, where the nucleated particles continue to grow upon the addition of more precursor. New metal oxide compositions can be added as a shell on the core matrix in a predictable fashion. Thus, this approach should permit the precise placement of dopants within a particle due to the layer-by-layer growth process.

Herein we utilize this approach to synthesize Sn-doped $In_2O_3$ nanocrystals with deliberate radial dopant placement and investigate the resulting LSPR spectra. We demonstrate that it is possible to precisely control the radial placement of dopants, maintaining uniform size dispersions and controlled core dimensions. We observe decreases in LSPR damping with dopant-segregated regions in the core or the shell with respect to homogeneously-doped nanocrystals. We confirm the presence of inactive Sn dopants on the nanocrystal surface, and observe their activation upon the addition of a sub-nanometer thick undoped $In_2O_3$ shell. Finally we show it is possible predictively design LSPR shape and energy, independent of dopant concentration, through control over core or shell dopant placement.

## Results and Discussion

*Synthesis of core/shell nanocrystals with varying radial dopant placement*

Two series of core/shell nanocrystals (In$_2$O$_3$/ITO core/shell, ITO/In$_2$O$_3$ core/shell) were synthesized through a one-pot, controlled, slow addition approach. Each series was synthesized (Scheme 4.1) by a two-stage approach whereby either i) an indium oleate precursor is used to produce an In$_2$O$_3$ core, then subsequently, and without purification, the mixed In/Sn precursor is slowly added to produce In$_2$O$_3$/ITO core/shell nanocrystals, or ii) a mixture of Sn and In oleate precursors is used to produce an ITO core, then subsequently, an indium oleate precursor is slowly added to produce ITO/In$_2$O$_3$ core/shell nanocrystals. Shell thicknesses were varied in each series to investigate the influence of dopant placement on the LSPR. Aliquots were taken and purified for analysis after the formation of the core and periodically during shell growth.

**Scheme 4.1.** Living growth synthesis of homogeneously doped and core/shell nanocrystals. In$_2$O$_3$ and ITO are represented in red and blue, respectively.
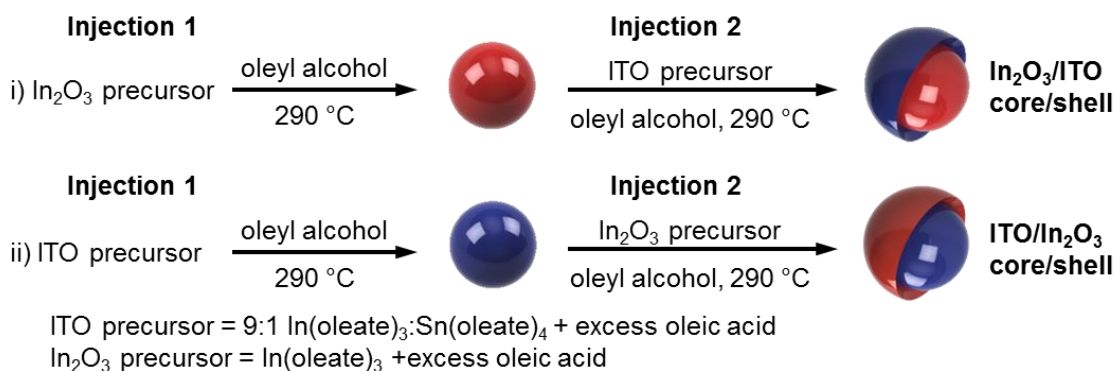


The dopant locations in the nanocrystals were investigated through a combination of bulk and surface elemental analysis. Absolute dopant concentration was determined for nanocrystals digested in stock hydrochloric acid and analyzed using inductively coupled

plasma optical emission spectroscopy (ICP-OES). The concentrations of surface localized Sn were investigated using X-ray photoelectron spectroscopy (XPS). XPS probes only the surface atomic structure (the sampling depth was calculated to be ~ 5 nm for the In and Sn 3d photoelectrons)[35] and has been previously shown to be a powerful technique in elucidating nanocrystal dopant distributions.[22,31] Relative surface Sn concentrations were quantified by integrating the In and Sn $3d_{5/2}$ peaks in the XPS spectra. Only minor attenuation of the signal is expected from the ligand shell, and this should be similar for both the indium and tin signals. Elemental analysis results are shown in Figures S1 and S2, and were used to confirm that Sn dopants were either located in the core or shell of the nanocrystals for the ITO/$In_2O_3$ and $In_2O_3$/ITO core/shell series respectively.

Figure 4.2 displays TEM micrographs of the initial core and final core/shell samples for the $In_2O_3$/ITO core/shell and ITO/$In_2O_3$ series. The nanocrystals are uniformly-sized single crystals that pack readily into extended arrays. HRTEM was performed on the largest $In_2O_3$/ITO and ITO/$In_2O_3$ core/shell particles (Figure C3). The analysis does not reveal the presence of any apparent structural defects of the crystalline particles at the core/shell interfaces, suggesting that the shells are epitaxially grown onto the core of the nanocrystals. Shell growth was monitored *via* SAXS (Figures S1 and S2). The final (largest) shell thicknesses were 4.1 and 4.0 nm for the $In_2O_3$/ITO and ITO/$In_2O_3$ series, respectively. SAXS and TEM analysis confirmed that there was no new nucleation upon shell precursor injection. The NIR absorbance spectra were measured from 3,100 to 11,000 $cm^{-1}$ (3225 to 909nm), and plotted for the $In_2O_3$/ITO and ITO/$In_2O_3$ core/shell series in Figures 2e and 2f, respectively. The initial absorbance spectrum of the $In_2O_3$/ITO core/shell

series in Figure 4.2e (black spectrum) displays no LSPR absorbance in the NIR and only displays ligand C-H stretches, as expected for an undoped nanocrystal.
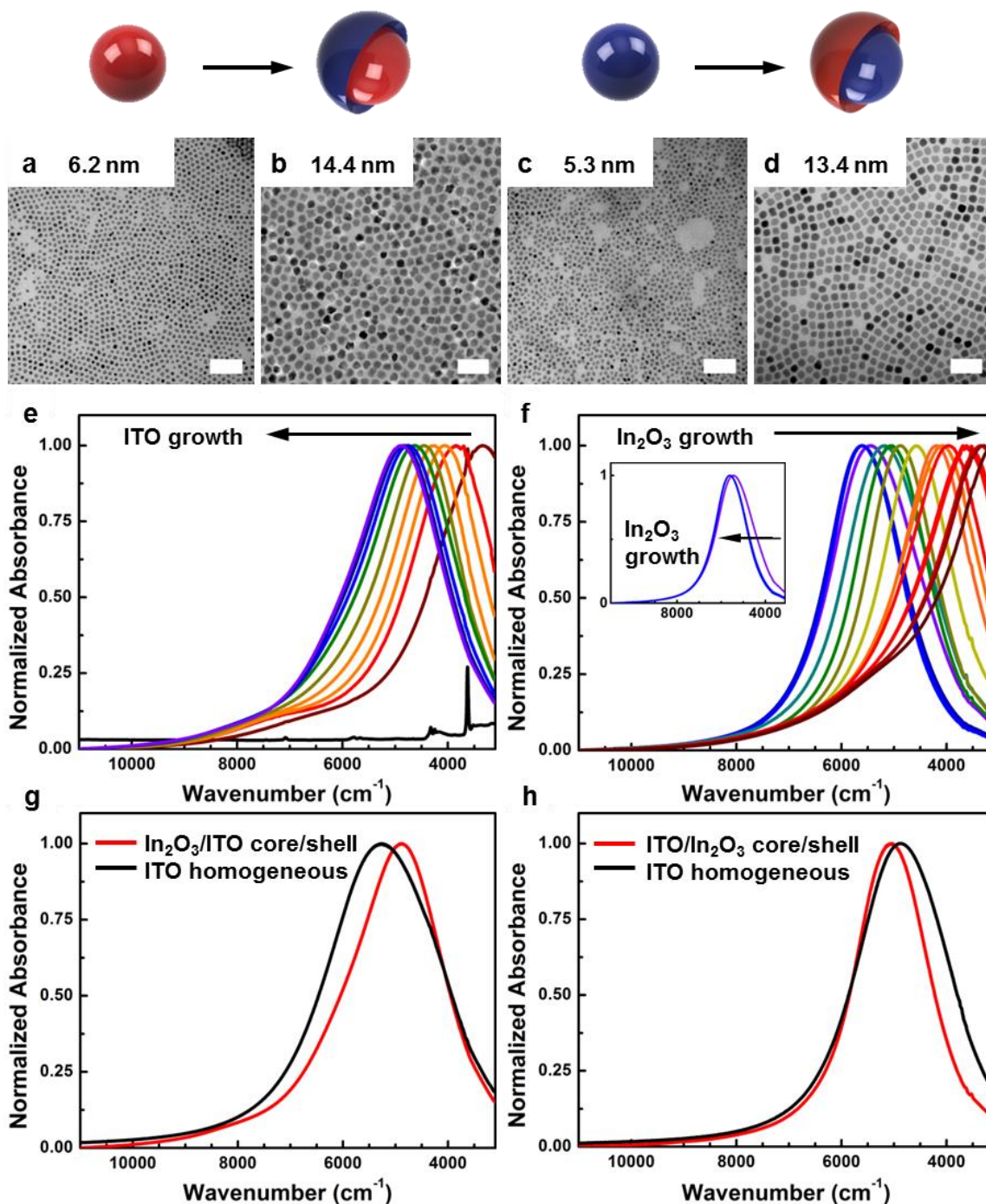


**Figure 4.2.** Core/shell schematics, TEM micrographs, and NIR spectra of $In_2O_3$/ITO (left) and ITO/$In_2O_3$ (right) core/shell nanocrystals. TEM images and respective core/shell schematics of the initial core and final core/shell samples, with sizes reported from SAXS:

In$_2$O$_3$ core (**a**); In$_2$O$_3$/ITO core/shell (**b**); ITO core (**c**); ITO/In$_2$O$_3$ core/shell (**d**). Core/shell schematics represent In$_2$O$_3$ and ITO in red and blue respectively. Scale bars are 50 nm. Normalized LSPR spectra for In$_2$O$_3$/ITO series during ITO shell growth (**e**), and ITO/In$_2$O$_3$ series during In$_2$O$_3$ shell growth (**f**). Normalized LSPR spectra of the ITO core and first ITO/In$_2$O$_3$ core/shell nanocrystal to show the initial blue-shift in the LSPR as a result of shell growth (**f, inset**). NIR spectra of In$_2$O$_3$/ITO core/shell sample (red) and homogeneously-doped ITO (black), with Sn concentrations of 9.71 and 9.98 atomic %, respectively (**g**), NIR spectra of ITO/In$_2$O$_3$ core/shell sample (red) and homogeneously-doped ITO (black), with Sn concentrations of 7.36 and 7.17% respectively (**h**).

The LSPR spectra for the In$_2$O$_3$/ITO core/shell nanocrystals are shown in Figure 4.2e. The shift in the LSPR$_{max}$ to higher energies with more incorporated Sn is consistent with that predicted by Eq. 1. The response of the LSPR should be proportional to the bulk plasma frequency ($\omega_p$), described by

$$\omega_p = \sqrt{\frac{N_e e^2}{m^* \varepsilon_0}} \tag{1}$$

where $N_e$ is the free carrier concentration, $e$ is the elementary charge, $m^*$ is the effective mass, and $\varepsilon_0$ is the permittivity of free space. As more Sn is incorporated into the lattice, the free carrier concentration is expected to increase, until a saturation point is reached at very high concentrations[16] (> 15 % Sn). For the ITO/In$_2$O$_3$ core/shell nanocrystals (Figure 4.2f), the LSPR$_{max}$ decreases as the dimensions of the In$_2$O$_3$ shell are increased, consistent with a dilution of free electrons due to the addition of the undoped shell.

Upon closer inspection of the spectra for the ITO/In$_2$O$_3$ core/shell nanocrystals (Figure 4.2f, inset), there is a blue-shift from 5436 to 5629 cm$^{-1}$ upon initial In$_2$O$_3$ shell growth before the peak maxima shift to longer wavelength as the shell thickens. The blue shift is accompanied by a 25% decrease in linewidth (1992 cm$^{-1}$ to 1548 cm$^{-1}$). To further explore the influence of thin shells of indium oxide on the ITO cores, we grew a series of sub-nanometer In$_2$O$_3$ shells on ITO (Figure C4). Although one would expect that the

addition of an undoped, $In_2O_3$ shell would effectively dilute the Sn concentration in the nanocrystal, and therefore should shift the LSPR to lower energy according to equation (1), these experiments (Figure C4) confirmed our initial observation that thin $In_2O_3$ shells lead to an initial blue-shift of the LSPR suggesting an effective increase in free electron concentration in the material. This observation provides further evidence to hypotheses that the ITO surface contains localized Sn surface trap states that contribute to a reduced dopant activation in ITO,[13,31] which can be activated by a sub-monolayer $In_2O_3$ shell. Surface trap states are well known in the QD literature[36–39] and can arise from a combination of ligand-surface interactions, dangling bonds, and surface site defects.

To further explore the influence of dopant placement on the LSPR, samples with the same dopant concentration, but different radial placement of the dopant atoms, were synthesized and examined. Figure 4.2g compares the LSPR response of an $In_2O_3$/ITO core/shell sample with a homogeneously-doped ITO nanocrystal sample, containing 9.71 and 9.98 atomic % Sn, respectively. Structural characterization, including ICP-OES and XPS analysis for both samples are shown in supporting information (Table C4). The $LSPR_{max}$ for the $In_2O_3$/ITO core/shell sample is red-shifted by approximately 381 $cm^{-1}$ and linewidth is decreased by approximately 439 $cm^{-1}$ (17%), relative to the homogeneously-doped sample. The red-shift is likely due to the slightly lower Sn concentration in the core/shell sample. A similar decrease in linewidth has been previously observed for surface-segregated ITO nanocrystals.[31] In that case, the authors suggest that narrowing of the linewidth results from less dopant-based scattering in the Sn-depleted core.

A comparison of the LSPR spectra for an ITO/$In_2O_3$ core/shell sample and a homogeneously-doped ITO sample of the approximately the same Sn concentration (7.36

and 7.17 atomic %, respectively) is shown in Figure 4.2h. Structural and compositional

characterization for both samples is shown in Table C5. Just as in the previous case, the

LSPR linewidth in the core/shell sample is narrower (by 26%, 1629 *versus* 2201 cm^{-1})

compared to the homogeneously-doped sample. In this case; however, the LSPR$_{max}$ of the

core/shell sample is blue-shifted relative the homogeneously-doped sample by 145 cm^{-1}.

The observed effects likely arise from the dopant-free shell, which aids in reducing

damping and a slight increase in dopant concentration (*vide infra*).

*Extraction of optical constants for core/shell nanocrystals*

The NIR optical responses observed in ITO nanocrystals can be interpreted semi-

quantitatively through their dielectric function described by the free electron

approximation of the Drude equation

$$\varepsilon_{NC}(\omega) = \varepsilon_{\infty} - \frac{\omega_p^2}{(\omega^2 + i\omega\Gamma)} \tag{2}$$

where $\varepsilon_{\infty}$ is the high frequency dielectric constant of ITO (taken as 4), $\omega_p$ is the bulk plasma

frequency of the free carriers, and $\Gamma$ is the free carrier damping. Using the Drude equation,

the LSPR absorption cross-section ($\sigma_A$) of the nanocrystals can be modeled from the quasi-

static approximation of Mie theory

$$\sigma_A = 4\pi k R^3 Imag \left\{ \frac{\varepsilon_{NC}(\omega) - \varepsilon_m}{\varepsilon_{NC}(\omega) + 2\varepsilon_m} \right\} \tag{3}$$

where $\varepsilon_m$ is the dielectric constant of the medium (2.238 for $CCl_4$), $k = \sqrt{\varepsilon_m}\omega/c$, and R

is the nanocrystal radius. The absorbance of the NC solution can then be calculated with

the Beer-Lambert law

$$A = \frac{N\sigma_A L}{\log(10)} \tag{4}$$

where N is the nanocrystal number density (#particles/cm$^{-3}$), and L is the pathlength of the cuvette. LSPR spectra from Figure 4.2 were modeled in order to extract $\omega_p$ and $\Gamma$. This simple Drude model has been used extensively to model LSPR spectra of semiconducting and oxide nanocrystals.[14,15,40–42] Example modeled spectra, along with a comparison to the observed spectra, are shown in Figure C5. Figure 4.3a shows $\omega_p$ and $\Gamma$ as a function of shell thickness for both the In$_2$O$_3$/ITO and the ITO/In$_2$O$_3$ core/shell nanocrystals represented in Figures 2e and 2f.
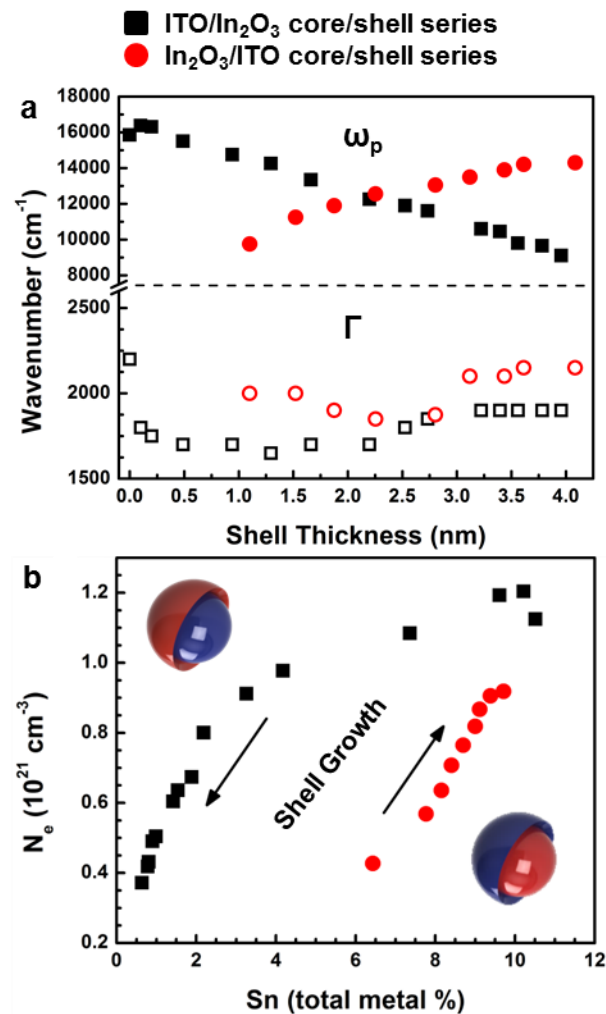


**Figure 4.3.** Extracted parameters from the spectra in Figure 4.2 as a function of shell thickness and absolute Sn concentration (measured by ICP-OES). Black and red symbols represent ITO/In$_2$O$_3$ and In$_2$O$_3$/ITO core/shell nanocrystals respectively. $\omega_p$ (top, solid

symbols) and $\Gamma$ values (bottom, open symbols) plotted *versus* shell thickness (**a**). $N_e$ values plotted against absolute Sn concentration (**b**). The core/shell schematics are placed for reference, with $In_2O_3$ and ITO represented in red and blue respectively.

As expected by equation 1, $\omega_p$ increases with increasing shell thickness for the $In_2O_3$/ITO core/shell nanocrystals. Interestingly $\Gamma$ decreases initially, indicating a reduction in electron scattering during LSPR excitation. As the main scattering mechanism in ITO is electron-ionized impurity scattering,[43,44] this decrease in $\Gamma$ is most likely due to the undoped $In_2O_3$ core providing an impurity-free zone for conduction band electrons to oscillate upon excitation. At greater shell thicknesses, the $In_2O_3$/ITO core/shell nanocrystals display in increase in $\Gamma$, most likely from the nanocrystals being > 90% ITO by volume and exhibiting damping closer to homogeneous ITO (see $\Gamma$ for ITO core, shell thickness = 0 nm, in Figure 4.3a).

For the ITO/$In_2O_3$ core/shell nanocrystals, $\omega_p$ increases during the first nanometer of shell growth, indicating and increase in $N_e$ (Figure C4). A significant decrease in damping, $\Gamma$, is also observed upon initial shell growth. Near the maximum shell thicknesses, $\Gamma$ increases, likely due to the cubic-shape of the nanocrystals (Figure 4.2d) giving rise to additional shape-dependent plasmonic modes in the LSPR spectrum.[21,45] The decrease in damping exhibited by both core/shell nanocrystals provides strong evidence that the undoped $In_2O_3$ region is the main factor in decreasing impurity scattering, independent of dopant concentration (as shown by Figures 2g and 2h). However the undoped $In_2O_3$ region located in the shell seems to reduce damping the most, likely due to reduced surface scattering, lack of Sn surface trap states, in addition to the impurity-free zone that both core/shell nanocrystals possess.

For both core/shell nancorystals, $N_e$ values were calculated from the extracted $\omega_p$ values using equation 1, and plotted in Figure 4.3b *versus* absolute Sn% as measured by ICP-OES. The ITO/In$_2$O$_3$ core/shell nanocrystals display an increasing $N_e$ initially in agreement with the observed blue-shift from Figure 4.2f, and a gradual decrease in $N_e$ as the Sn is diluted from the In$_2$O$_3$ shell. Conversely, the In$_2$O$_3$/ITO core/shell nanocrystals display an increase in $N_e$ with increasing shell thickness. Comparing the two series, the ITO/In$_2$O$_3$ core/shell series utilizes nearly an order of magnitude less absolute dopant % for an equivalent LSPR energy than the In$_2$O$_3$/ITO core/shell series (0.78% Sn for $N_e$ of 0.42 x 10$^{21}$cm$^{-3}$ *versus* 6.43% Sn for $N_e$ of 0.43 x 10$^{21}$cm$^{-3}$ respectively). Because the nanocrystal diameters are several orders of magnitude smaller than the wavelength of absorbing light, size effects on the LSPR are negligible and can effectively be ignored,[40,46] indicating that only dopant concentration and radial location (core *versus* shell) is contributing to the LSPR spectra. As aliovalent doping leads to scattering-based damping in metal oxides, any opportunity to reduce dopant concentration is an opportunity to improve material performance.

*Investigating the impact of radial dopant placement on LSPR energy and damping.*

Currently two of the biggest challenges in plasmonic metal-oxide nanocrystal synthesis are increasing dopant activation (*i.e.*, maximizing the number of free electrons contributed per dopant atom) and mitigating plasmonic damping. Common causes of reduced dopant activation include dopant-induced defects (such as Sn-oxo complexes and the formation of tin oxide phases)[47,48] and inactive surface sites[31,49,50] (arising from crystal defects[36,38] and ligand-metal binding[39]). Thus, in attempts to achieve high dopant activation

at large dopant concentrations, these increases in dopant levels may yield more defects and reduce activation. Plasmonic damping generally arises from a combination of ionized impurity scattering (from the dopant atoms themselves), surface scattering, and scattering from charge compensation defects (such as oxygen vacancies).[14,15] Ionized impurity and charge compensation defect scattering are generally reduced by a decrease in Sn concentration. It is therefore synthetically challenging to mitigate damping when higher dopant densities are needed to achieve desired carrier concentrations.

To explore how the radial placement of dopants can be used as a strategy to enhance dopant activation and reduce plasmon damping, we synthesized and investigated the optical properties of two core/shell series of Sn-doped $In_2O_3$ nanocrystals. The *Doping Series* allows for the investigation of architecture on LSPR energies and dopant activations by keeping the absolute doping levels constant. This is accomplished by adapting the synthetic strategy in Scheme 4.1 so that nanocrystal samples in the Doping Series would be of approximately equal doping concentration and diameter. This ensures that the observed changes to the LSPR and observed dopant activation would be due solely to the radial dopant location. Because the plasmon energy depends on damping (Eqs. 2-4), a series of nanocrystals were produced with the same $LSPR_{max}$ to isolate the effects of radial dopant placement on damping. Thus, the *Damping Series* allows for a convenient comparison of structural effects on damping by holding LSPR energy equivalent across different nanocrystal structures. To this end, two core/shell samples, one from Figure 4.2e and one from Figure 4.2f in Section I, were selected that have the same LSPR energies. A homogeneously-doped sample was designed and synthesized to have the same LSPR energy for comparison to the other two samples.
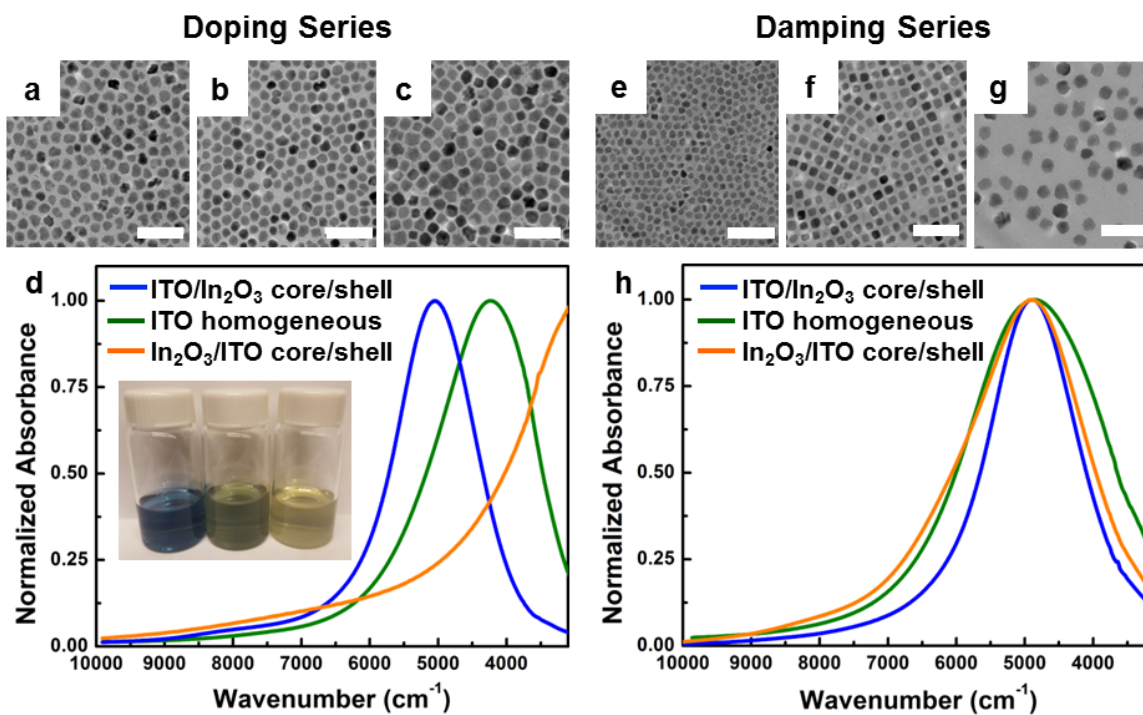
**Figure 4.4.** ITO nanocrystals for the Doping (left) and Damping (right) Series. Doping Series (left): TEM micrographs of homogeneously doped ITO nanocrystals (**a**), ITO/In₂O₃ core/shell nanocrystals (**b**), and In₂O₃/ITO core/shell nanocrystals (**c**). Scale bars are 50 nm. Normalized LSPR absorption spectra (**d**). Inset: photograph of the purified nanocrystal solutions in hexanes, immediately following synthesis, spectra presented left to right correspond to solution presented left to right. Damping Series (right): TEM micrographs of homogeneously doped ITO nanocrystals (**e**), ITO/In₂O₃ core/shell nanocrystals (**f**), and In₂O₃/ITO core/shell nanocrystals (**g**). Scale bars are 50 nm. Normalized LSPR absorption spectra (**h**).

Figure 4.4 displays TEM micrographs for the nanocrystals from both Doping and Damping Series. Samples in the Doping Series are approximately equal size as measured by SAXS (Table 4.1), with the In₂O₃/ITO sample measured to be slightly larger (~ 2 nm larger in diameter), likely due to differences in nucleation without the initial presence of dopant cations. Samples in the Damping Series have different sizes, as well as shape, by SAXS (Table 4.2) and TEM. These size and shape discrepancies are expected given the

80

varying Sn concentrations and core/shell architectures required to produce an LSPR with the same energy. The dopant distributions were investigated *via* ICP-OES and XPS in the same fashion described previously. The overall tin content of samples in the Doping Series (Table 4.1) is essentially the same (within 0.5 atomic % Sn) as measured by ICP-OES. Results of the surface analysis by XPS (Table 4.1) are in agreement with the specific architecture described, and confirm the anticipated Sn localization in each sample. The Damping Series contains a range Sn doping percentages from 3.26 to 9.71 total metal %.

**Table 4.1.** Doping Series: nanocrystal size, absolute and surface Sn concentrations, and extracted parameters from Drude modeling of the LSPR spectra in Figure 4.4d.

| Structure | Size +/- 1$\sigma$ (SAXS, nm) | Core size (SAXS, nm) | Sn % (ICP-OES) | Sn % (XPS) | $\omega_p$ (cm$^{-1}$) | $N_e$ ($10^{21}$cm$^{-3}$) | $\Gamma$ (cm$^{-1}$) |
|---|---|---|---|---|---|---|---|
| ITO homogeneous | 10.7+/- 1.6 | N/A | 4.17 +/- 0.05 | 4.5 +/- 0.2 | 12750 | 0.73 | 1850 |
| ITO/In$_2$O$_3$ core/shell | 10.2+/- 1.2 | 7.0 +/- 1.0 | 3.63 +/- 0.08 | 2.5 +/- 0.2 | 15280 | 1.05 | 1650 |
| In$_2$O$_3$/ITO core/shell | 12.8 +/- 1.6 | 11.1 +/- 1.4 | 3.84 +/- 0.06 | 5.6 +/-0.1 | 7500 | 0.25 | 3100 |

**Table 4.2.** Damping Series: nanocrystal size, absolute and surface Sn concentrations, and extracted parameters from Drude modeling of the LSPR spectra in Figure 4.4h.

| Structure | Size +/- 1$\sigma$ (SAXS, nm) | Core size (SAXS, nm) | Sn % (ICP-OES) | Sn % (XPS) | $\omega_p$ (cm$^{-1}$) | $N_e$ ($10^{21}$cm$^{-3}$) | $\Gamma$ (cm$^{-1}$) |
|---|---|---|---|---|---|---|---|
| ITO homogeneous | 7.3+/- 1.1 | N/A | 7.17 +/- 0.05 | 7.7 +/- 0.2 | 14250 | 0.91 | 2500 |
| ITO/In$_2$O$_3$ core/shell | 7.9+/- 0.9 | 5.3 +/- 2.3 | 3.26 +/- 0.07 | 3.5 +/- 0.2 | 14300 | 0.92 | 1600 |
| In$_2$O$_3$/ITO core/shell | 14.4 +/- 2.2 | 6.3 +/- 0.8 | 9.71 +/- 0.04 | 10.3 +/-0.2 | 14300 | 0.92 | 2050 |

The NIR absorbance spectra were measured and plotted for the Doping Series in Figure 4.4d. The colors of the as-synthesized nanocrystal solutions dispersed in hexanes (Figure 4.4d inset) are strikingly different, ranging from yellow to blue, despite the nanocrystal containing the same concentration of dopant. Upon inspection of the NIR spectra (Figure 4.4d) we observe the ITO/In$_2$O$_3$ core/shell nanocrystals to have the highest LSPR energy (of 5020 cm$^{-1}$), compared to 4220 cm$^{-1}$ and 3030 cm$^{-1}$ for the homogeneously-doped and In$_2$O$_3$/ITO nanocrystals, respectively. To further investigate the LSPR, we modeled all three spectra with the Drude formula., with the extracted values in Table 4.1.

The ITO/In$_2$O$_3$ core/shell sample exhibits an N$_e$ value four times greater than the In$_2$O$_3$/ITO core/shell sample, with damping reduced by 50%. The extracted damping from the In$_2$O$_3$/ITO sample is much larger, either because of the cubic nature of the nanocrystal and/or detector cutoffs that do not allow the full LSPR to be observed and modeled. The ITO/In$_2$O$_3$ core/shell sample also yields an N$_e$ value 25% larger, and damping value that is 11% reduced with respect to the homogeneous sample. The N$_e$ value (1.05 10$^{21}$cm$^{-3}$) for the ITO/In$_2$O$_3$ core/shell nanocrystals is unusually high given the doping level (3.26% Sn). In previously reported ITO nanocrystal samples, significantly higher doping levels (5 – 7% Sn) were required in order to attain an analogous free carrier concentration, depending upon the reaction chemistry used to synthesize the nanocrystals.[31] Combined, these results indicate that having a dopant-free shell (*i.e.*, ITO/In$_2$O$_3$ core/shell) increases dopant activation more than the other two architectures.

The NIR absorbance spectra were measured and plotted for the Damping Series in Figure 4.4h. LSPR linewidth (which is an indication of the overall damping in the

nanocrystal) has been shown to be a defining feature for device performance and design,[4,30,51–53] from sensing, thin film conductivity,[31] and selective electromagnetic radiation filtering.[54–56] From the spectra in Figure 4.4h, it is readily apparent that linewidth can be tuned with radial dopant placement, with linewidths measured to be 1552, 2101, and 2358 cm$^{-1}$ for the ITO/In$_2$O$_3$ core/shell, In$_2$O$_3$/ITO core/shell, and ITO homogeneous nanocrystals respectively.  As measured by ICP-OES, the Sn % required to produce an LSPR of ~4870 cm$^{-1}$ for the ITO/In$_2$O$_3$ core/shell sample is only 3.55 %, compared to 7.20 % and 9.71 % for the homogeneously doped ITO and In$_2$O$_3$/ITO core/shell nanocrystals respectively. This activation trend is in agreement with our findings from the Doping Series, with Sn being most activated when there is an In$_2$O$_3$ shell (ITO/In$_2$O$_3$ core/shell).

To compare damping and carrier concentration values between the samples, Drude modeling was performed on the LSPR spectra from Figure 4.4h for the Damping Series, and the extracted values shown in Table 4.2.  Both core/shell nanocrystals display dramatically reduced damping values with respect to the homogeneous sample, with a 36% and 18% damping reduction for the ITO/In$_2$O$_3$ and In$_2$O$_3$/ITO nanocrystals, respectively. The In$_2$O$_3$/ITO core/shell sample is particularly interesting, because the nanocrystals contain much more overall Sn relative to the homogeneously-doped sample (Table 4.2), however In$_2$O$_3$/ITO core/shell nanocrystals display *less* plasmonic damping. This suggests that the dopant-depleted core is aiding in reducing the damping regardless of the excess Sn present. Across the three samples the ITO/In$_2$O$_3$ core/shell sample produces the lowest damping value of 1600 cm$^{-1}$ due to (i) reduced impurity scattering from fewer dopant cations present (Table 4.2) and (ii) the dopant-depleted shell. Plasmon damping values have been reported with wide ranges[31] as high as 5000-8000 cm$^{-1}$, from nanocrystals

synthesized with a combination of carboxylates and amines,[16] and with much lower values of 900 – 1500 $cm^{-1}$ from nanocrystals synthesized from a mixture of metal acetonates, chlorides and oleyl amine.[18] While it may be tempting to draw direct comparisons from values in this study to other values reported for ITO nanocrystals in the literature, the chemistries used to synthesize the nanocrystals can influence the properties beyond the effects due to doping. The range of ITO syntheses rely on different solvents, surfactants, metal precursors, temperatures, and counter anions, all of which will contribute to the defect chemistry in the nanocrystals that is then manifested spectrally in sometimes unpredictable ways. The approach presented here allows for direct comparison between nanocrystals synthesized with varying levels and placements of dopants because the nanocrystals are all synthesized from the same precursor material, using the same surfactants, under the same reaction conditions.

**Conclusion**

The synthetic method described here offers the opportunity for precise radial dopant positioning within an oxide nanocrystal matrix. Dopants can be positioned with sub-nanometer precision into the host nanocrystal *via* the slow injection of metal precursors, with no purification required in between precursor additions. We utilized Sn-doped $In_2O_3$ (ITO) as a model system to evaluate the influence of radial dopant position on resulting properties, in this case the LSPR response. The core/shell nanostructure architectures were confirmed through bulk and surface elemental analysis.

Radial dopant placement has a profound influence on the LSPR energy, free electron concentration, and damping. Inactive Sn surface sites could be activated upon the addition of a thin ($\leq 0.5$ nm) $In_2O_3$ shell. In both types of core/shell nanocrystals, damping

decreased relative to homogeneously-doped nanocrystals, due to the dopant-free region. $ITO/In_2O_3$ core/shell nanocrystals have the lowest damping, due to the dopant-free region at the surface, which reduces surface and impurity scattering, while increasing activation. This undoped region is crucial to realizing the theoretical minimum damping in metal-oxide nanocrystals, which has been a challenge in material development.

The ability to precisely control the radial placement of dopants creates opportunities in structure/property design and optimization. We foresee this approach ultimately being widely applicable to other metal oxide nanocrystal systems, whose properties are inhibited by dopant-scattering and localized-surface defects. Studies involving a combination of ultrafast optical spectroscopy and rigorous computational modeling will aid in developing a more comprehensive understanding of the underlying electronic structure of these materials and prove useful in tapping the nearly infinite compositions made possible through the control of dopant placement in these materials. This same approach should also be useful in modifying catalytic, magnetic, and electronic properties of nanocrystal extending beyond $In_2O_3$ systems.

**Materials and methods.**

Indium(III) acetate (99.99%), oleic acid (90% technical grade), and tin(IV) acetate were purchased from Sigma-Aldrich and used as received. Oleyl alcohol (80-85% technical grade) was purchased from Alfa Aesar and used as received. A flow meter purchased from Cole-Parmer was used to monitor nitrogen flow (model 03216-10).

*Synthesis of Homogeneously-doped and Core/shell Nanocrystals*

All syntheses were carried out similar to those described in literature with modifications to control the placement of dopant atoms into the nanocrystal matrix.[32,33]

*Synthesis of In₂O₃/ITO core/shell nanocrystals (Figures 2, S1, S3)*

Two precursor solutions were prepared in separate vials. In one vial, indium(III) was mixed with of oleic acid (in a 1:6 molar ratio) to yield an undoped indium oleate precursor solution. In a separate vial, tin(IV) acetate and indium(III) acetate (in a 1:9 Sn:In ratio) were mixed with oleic acid (in a 1:6 metal to acid molar ratio) to yield a 10% Sn doped ITO precursor solution. Both precursors were left at 150 °C under $N_2$ for several hours. Indium oxide nanocrystals cores were synthesized by first adding the indium oleate precursor solution at a rate of 0.35 mL/min *via* syringe pump to 13.0 mL of oleyl alcohol at 290 °C. A 6.3 nm $In_2O_3$ core was grown in this manner, and a small aliquot was pulled out of the reaction flask using a 1.0 mL syringe. After the addition of the undoped precursor, a 10% ITO precursor solution was added to the reaction solution in the same manner described above. During the dropwise addition of the ITO precursor, small aliquots were taken out of the reaction vessel for analysis. Nanocrystals were isolated by precipitating with ~12 mL of ethanol. The solid was collected by centrifugation at 7000 rpm for 10 min. The solid was then washed and centrifuged once more with ethanol. Elemental analysis along with size and size dispersion analysis by SAXS from these particles can be found in Figure C1.

*Synthesis of ITO/In₂O₃ core/shell nanocrystals (Figures 2, S2, S3)*

For the synthesis of the ITO/$In_2O_3$core/shell nanocrystals, a 10% Sn ITO precursor solution was added to oleyl alcohol in the same manner described above. A 5.3 nm ITO core was grown in this manner, and a small aliquot was pulled out of the reaction flask

using a 1.0 mL syringe. After the addition of the ITO precursor, an indium precursor solution was added to the reaction solution in the same manner described above. During the dropwise addition of the indium precursor, small aliquots were taken out of the reaction vessel for analysis. Aliquots were purified and analyzed as stated above. Elemental analysis along with size and size dispersion analysis by SAXS from these particles can be found in Figure C2.

*Synthesis of the homogeneously doped ITO nanocrystals (Figure 4.2, Tables S1 and S2)*

An ITO metal oleate precursor was prepared by mixing indium(III) acetate and tin(IV) acetate (in the proper molar ratio for the desired Sn doping level) in oleic acid (1:6 metal to acid molar ratio) in a scintillation vial. The solution was stirred at 150 $^{o}$C under $N_2$ for several hours. Nanoparticles were formed by adding the precursor at a rate of 0.35 mL/min, using a syringe pump, to 13.0 mL of oleyl alcohol in a 100 mL three-neck flask at 290 $^{o}$C. The three-neck flask was sealed with septa, however $N_2$ was allowed to flow over the solution at a rate of ~130 cc/min and exit out each of several purge needles. Aliquots were purified and analyzed as stated above.

*Synthesis for activation of Sn surfaces on an ITO nanocrystal (Figure C4)*

A 10% ITO precursor solution was added to oleyl alcohol in the same manner described above to yield a 6.9 nm ITO nanocrystal. An aliquot was taken at this point for analysis. Next, 20 drops of an undoped, indium oleate precursor was added to the reaction vessel. Another aliquot was taken at this point. Ten more drops of the indium oleate was added to the reaction vessel, another aliquot was taken, and finally ten more drops of undoped precursor was added to the vessel. Aliquots were purified and analyzed as stated above. Size and size dispersions from this synthesis can be found in Figure C4.

*Synthesis of the homogeneously doped ITO nanocrystals (Figure 4.4, Table 4.1)*

A 3.3 % ITO metal oleate precursor was prepared by mixing indium(III) acetate (846 mg, 2.90 mmol) and tin(IV) acetate (35 mg, 0.10 mmol) in 6 mL of oleic acid in a scintillation vial. The solution was stirred at 150 °C under $N_2$ for several hours. Nanoparticles were formed by adding the precursor at a rate of 0.35 mL/min, using a syringe pump, to 13.0 mL of oleyl alcohol in a 100 mL three-neck flask at 290 °C. The three-neck flask was sealed with septa, however $N_2$ was allowed to flow over the solution at a rate of ~130 cc/min and exit out each of several purge needles. Aliquots were purified and analyzed as stated above. After collection, the final nanocrystals (350 mg, > 90% yield; yield for the nanocrystal core was calculated from the inorganic core mass (determined using Thermal Gravimetric Analysis from the mass isolated and the mass percent remaining after heating to 600 °C) and the theoretical maximum yield from the metal salts to form the metal oxide.

*Synthesis of the ITO/In$_2$O$_3$ core/shell nanocrystals (Figure 4.4, Table 4.1)*

Core/shell nanocrystals were prepared using the same method described above for homogeneously doped nanocrystals using different precursor solutions. Two precursor solutions were prepared in separate vials. In one vial, indium(III) acetate (584 mg, 2.00 mmol) was mixed with 4.0 mL of oleic acid to yield an undoped indium oleate precursor solution. In a separate vial, tin(IV) acetate (35 mg, 0.10 mmol) and indium(III) acetate (263 mg, 0.901 mmol) were mixed with 2.0 mL of oleic acid to yield a 10% doped ITO precursor solution. Both precursors were left at 150 °C under $N_2$ for several hours. Nanocrystals were synthesized by first adding the ITO precursor solution at a rate of 0.35 mL/min *via* syringe pump to 13.0 mL of oleyl alcohol at 290 °C. After the addition of the

2.0 mL precursor, the ITO precursor was removed from the syringe pump and replaced with the indium oleate precursor. The indium oleate precursor was added *via* syringe pump to the reaction solution at the same addition rate. Aliquots were purified and analyzed as stated above, and yield determination of the nanocrystal products were carried as described above for homogeneously doped nanocrystals (355 mg, > 90% yield).

*Synthesis of In$_2$O$_3$/ITO core/shell nanocrystals (Figure 4.4, Table 4.1)*

10% ITO and indium oleate precursors were prepared in separate vials as described above. Nanocrystals were synthesized by first adding the undoped indium oleate precursor at a rate of 0.35 mL/min to 13.0 mL of oleyl alcohol at 290 °C the flask, then adding the ITO precursor. Precursors were added *via* a syringe pump and the nanocrystals were isolated and purified as described above (340 mg, > 90% yield.

*Characterization of Indium Oxide and Sn-doped Indium Oxide Nanocrystal*

Optical measurements were carried out on a PerkinElmer (Waltham, MA) Lambda 1050 UV/Vis/NIR Spectrometer. Spectra were collected in CCl$_4$ using only one detector (PbS) in order to remove most detector artifacts. Samples were diluted to a concentration of ~0.5 mg/mL. Spectra were sampled from 1000 – 3300 nm with a scan resolution of 1 nm.

Elemental compositions of the nanocrystal cores were determined using a Teledyne Leeman Labs (Hudson, NH) Prodigy High Dispersion Inductively Coupled Plasma Optical Emission Spectrometer (ICP-OES). Nanocrystals were dried and digested in stock HCl for at least 48 hrs before being diluted for analysis.

Elemental composition for the surface of the nanoparticles was determined using a Thermo Scientific ESCALAB 250 X-ray Photoelectron Spectrometer (XPS). Samples

were prepared by drop casting a hexanes solution onto mica substrates. Surface tin content was determined by integrating the tin $3d_{5/2}$ peaks and comparing those intensities to those of the indium $3d_{5/2}$ peaks.

Transmission electron microscopy (TEM) micrographs were collected using a FEI Tecnai Spirit TEM (Hillsboro, OR) operating at 120 kV. HRTEM images (Figure C1) were collected on a 300 kV $C_s$ image corrected FEI Titan (S)TEM. Nanocrystals were imaged on Ted Pella (Redding, CA) lacey carbon grids supported by a copper grid. Samples were prepared by dropping a sample dissolved in hexanes onto the water surface in a small vial, allowing the hexanes to dissolve, and dipping a grid through the layer of particles.

Small-angle X-ray scattering (SAXS) analysis was done on a lab-scale SAXS (SAXSess, Anton Paar, Austria). The system was attached to an X-ray generator equipped with an X-ray tube (Cu Kα, wavelength λ = 0.154 nm) operating at 40 kV and 50 mA. The scattered X-ray intensities were measured with a charge-coupled device detector (Roper Scientific, Germany). The raw data was processed with SAXSquant software (version 2.0). Scattering curves were averaged over 50 individual curves for various acquisition times (0.25-15s). Curve fitting was done using Irena macros for IGOR (V. 6.3.7.2).[57]

Drude modeling was performed in MatLab. Models were fitted manually to simulated spectra through a combination of Equations 1-4. Models were allowed to optimize to a least-squared fit, with extracted value errors of 25 cm^{-1}. This approach has been used extensively to model LSPR spectra of metal oxide, and metal chalcogenide nanocrystals.[40-42]

**Bridge to Chapter V**

Chapter V presents concluding remarks from the synthetic possibilities described in the previous chapters, and outlooks to future opportunities provide by advances in colloidal synthetic development.

CHAPTER V


CONCLUSION

I am the primary and sole author to the writing of this chapter.


**Concluding Remarks**

Nanotechnology is expected to revolutionize technologies in society, including advances in medicine, energy harvesting and storage, and molecular sensing to name a few. However, the utilization of nanocrystals is hindered by the lack of predictable, intuitive, and accessible syntheses. The properties of nanocrystals arise from nanometer- to angstrom-level structural features and composition, and therefore the synthesis of nanocrystalline materials needs to be approached from the atomic level, atom-by-atom. Atomic-level resolution in synthesis and structural characterization will fuel the nano-technological revolution.

Continuous growth synthesis for producing metal oxide nanocrystals is a leap forward towards the goals and promises of nanotechnology. The synthesis allows for layer-by-layer, nearly atom-by-atom growth of metal oxide nanocrystals, with tailored size, composition, and internal structure. This synthesis has allowed for new size and structure studies to be performed that were previously not possible, and allows for countless new studies on structure and properties to be investigated. The sampling of nanocrystal size, composition, and structure shown in this dissertation is but a small sample of the near infinite structure possibilities provided by the continuous growth synthesis.

In Chapter II of this dissertation, the continuous growth synthesis was applied to investigate dopant incorporation into indium oxide nanocrystals. The continuous growth synthesis was shown to provide dopant incorporation at stoichiometric levels, where the composition can be predicted and tuned simply by altering the precursor composition. The dopants were found to be homogeneously distributed, whereas dopant incorporation has been previously rife with dopant exclusion and segregation. The synthesis allows for the uniquely predictable incorporation of dopants due to the balanced chemical reactivities of the host and dopant precursors under the reaction esterification conditions.

In Chapter III of the dissertation, the first Sn-doped $In_2O_3$ (ITO) nanocrystal size ladder was produced, in order to investigate the dependence of nanocrystal size on thin film optoelectronic properties. Traditional approaches to ITO nanocrystal synthesis, utilized a wide variety of reaction chemistries to produce the nanocrystals. As a consequence, there was a lack of control over size, doping, and dopant distribution, which inhibited any possibility of investigating size-dependent properties. The study performed in Chapter II concluded that thin film resistivity decreases by over an order of magnitude when NC size is increased from 5 to 21 nm. Additionally, it was found that the main barrier to conduction in the nanocrystal thin film is the coulombic charging energy for transferring charge between neighboring nanocrystals, and above 14 nm in diameter the energy barrier becomes negligible.

In chapter IV, the concepts of dopant incorporation and size control from Chapters II and III, respectively, were utilized in tandem to produce dopant localized core/shell nanocrystals. Nanocrystals of Sn-doped $In_2O_3$ were produced with varying radial dopant distributions of core-localized, shell-localized, and homogeneous distributions, and the

93

influence of dopant distribution on the nanocrystal plasmonic properties was investigated. The dopant distributions were altered by simply adjusting the introduction order of the dopant precursor and the undoped precursor into the reaction. The distribution of dopants was found to have a profound influence on the plasmonic properties such as energy, damping, and dopant activation. Dopant distribution was found to be, in some instances, more influential than the general composition of the nanocrystals. This study is the first example of deliberately controlled dopant distribution in metal oxide nanocrystals, the first example of sculpting plasmonic properties through dopant distribution, and the first example of decoupling plasmonic properties from composition.

**Future Outlooks**

Discovery and application of the continuous growth synthetic approach to new oxide materials, and more complex heterostructures, will require a more complete understanding of the chemistry involved throughout the stages in the reaction. A few key examples include: 1) identifying the identity of the monomer species that leads to nanocrystal formation, 2) the role of the slow precursor introduction on nanocrystal growth and formation, 3) the role of the ligand-surface interaction on facilitating nanocrystal growth and resulting morphology, 4) using additional additives and ligands to control the reactivity of the nanocrystal surface, in order to allow epitaxial growth of new oxide materials. Many, if not all, of these examples will be temperature and solution composition dependent, and there is much experimental parameter space to explore regarding the controllable synthetic variables. In general many mechanistic studies on nanocrystals (including the ones in this dissertation) are performed through inference and black-box chemistry, where reaction parameters are altered and the final products analyzed. This

94

approach has been quite successful, but provides little to no insight of the reaction chemistries during reaction progression. Advances in *in situ* studies will improve understanding of nanocrystal formation and growth, and better inform product design.

In the face of challenges and unknown variables in synthetic discovery, the approach provided by the continuous growth synthesis brings inspiration to the future of nanomaterial development. The ultimate goal, would be to apply this approach to the entirety of metal oxides. The goal is not too far-fetched, considering in only a few years the studies from the approach have already covered approximately 10% of the Periodic Table as either host or dopant atoms. It appears that the continuous growth mechanism allows for predictable, intuitive design and production of seemingly endless combinations of materials, that show promise with their catalytic, optical, magnetic, and electronic properties. Looking forward, this synthetic approach should be applied to tackle difficult and technologically relevant targets, as well as develop new and exotic heterostructures. The combination of multiple materials, incorporated into a layer-by-layer approach, with atomic-level composition control can begin to develop advanced nanomaterials that possess not only the combination of properties derived from the constituents, but potentially exhibit new and synergistic properties that were once inconceivable.

APPENDIX A


SUPPORTING INFORMATION FOR CHAPTER IV: TRANSITION METAL-DOPED

METAL OXIDE NANOCRYSTALS: EFFICIENT SUBSTITUTIONAL DOPING

THROUGH A CONTINUOUS GROWTH PROCESS
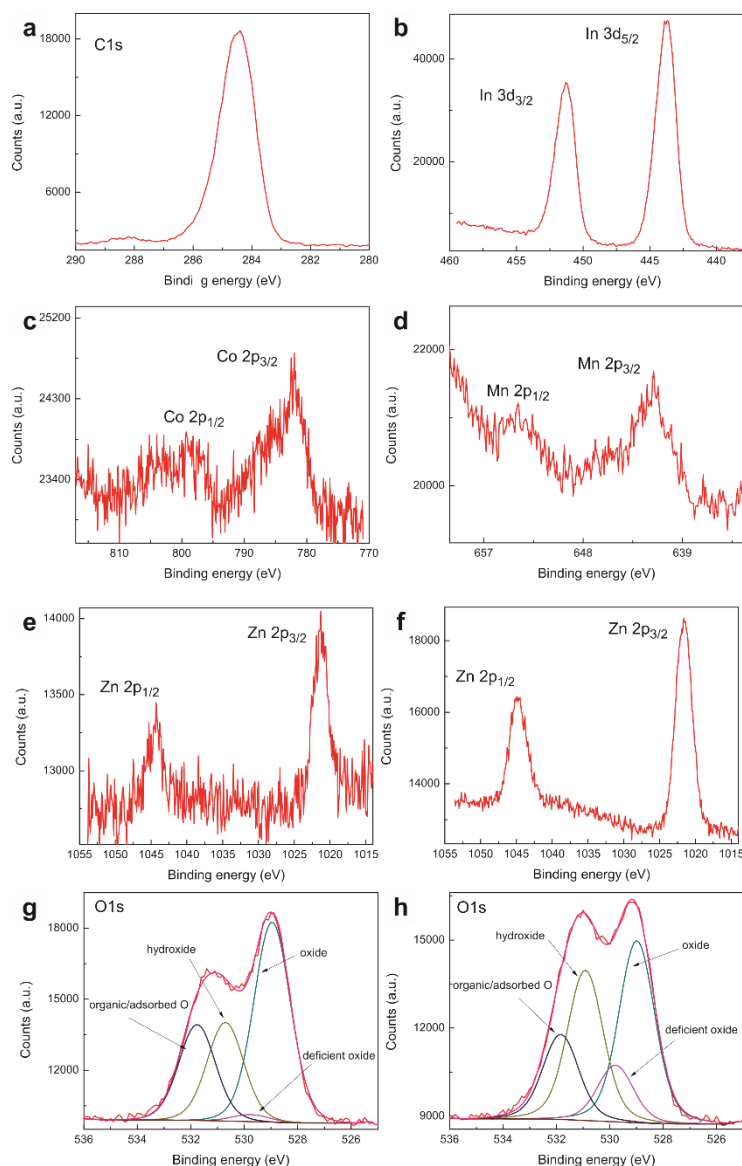
**Figure A1**. XPS spectra of doped $In_2O_3$ nanocrystals. Compositions shown in Table 3 of the manuscript are calculated based on integration of the In $3d_{5/2}$ and dopant $2p_{3/2}$ peak. **a**) displays a typical C1s spectra and **b**) a typical In 3d spectra of the doped and undoped nanocrystals. **c**) and **d**) show the Co and Mn 2p spectra from Co: $In_2O_3$ and Mn: $In_2O_3$ respectively. **e**) and **f**) display the Zn 2p region of 5% Zn: $In_2O_3$ and 20% Zn: $In_2O_3$, respectively. **g**) displays the O1s spectra from 5% Zn: $In_2O_3$, and **h**) 20% Zn: $In_2O_3$. The O1s spectra shown in **g** and **h** can be fit to four peaks of the same peak shape and a width of 1.5 eV; the peak at 529.0 eV corresponds to oxide in $In_2O_3$, the peak 0.7 eV greater corresponds to oxygen deficient/defect oxide, the peak at 530.9 eV corresponds to hydroxide, and the peak at 531.8 eV corresponds to adsorbed oxygen and organic oxygen in the ligand shell.[1–5] The increase in dopant atom concentration likely leads to the increase in oxygen vacancy formation, which displayed in **g** and **h**. Spectra are referenced to the C1s hydrocarbon peak at 284.5 eV.

97
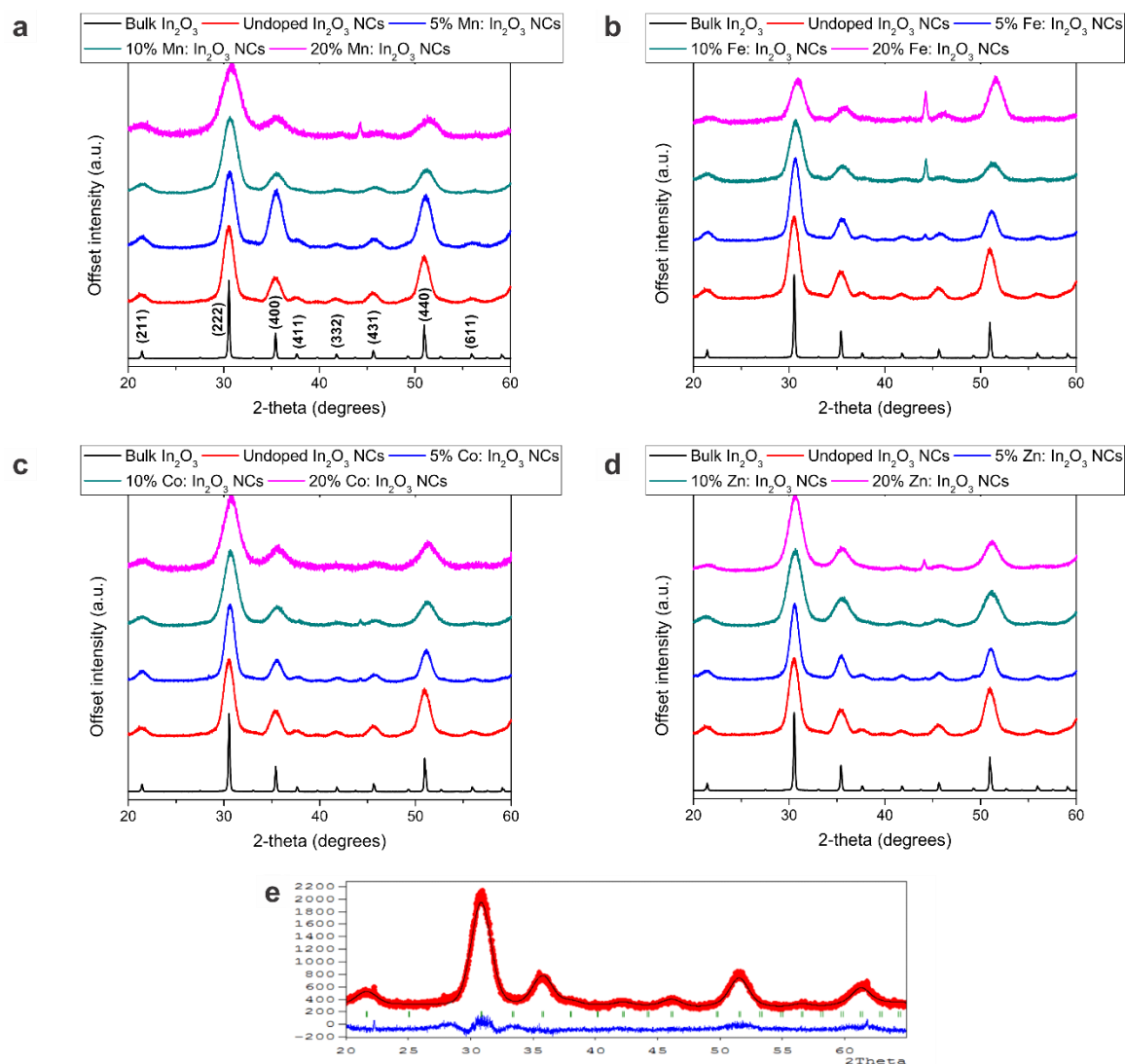
**Figure A2**. Raw XRD patterns acquired from undoped and doped $In_2O_3$ nanocrystals at varying dopant concentrations, re-plotted from Figure 2 in the manuscript: **a**) Mn: $In_2O_3$ **b**) Fe: $In_2O_3$ **c**) Co: $In_2O_3$ **d**) Zn: $In_2O_3$. The peak present at 43.5 º in some samples is due to the silicon substrate. All acquired patterns match that of cubic $In_2O_3$ (bulk pattern shown in black in each plot). **e**) Displays a typical Rietveld refinement using Fullprof Suite.[6] Background points were picked by hand, and peaks were fit using a pseudo-Voigt profile. Once scale, zero offsets, and peak shape were refined, lattice parameters were allowed to optimize. In XRD patterns where the substrate peak is present, an exclusion zone in the refinement was added to prevent model optimization from 43-44 º.
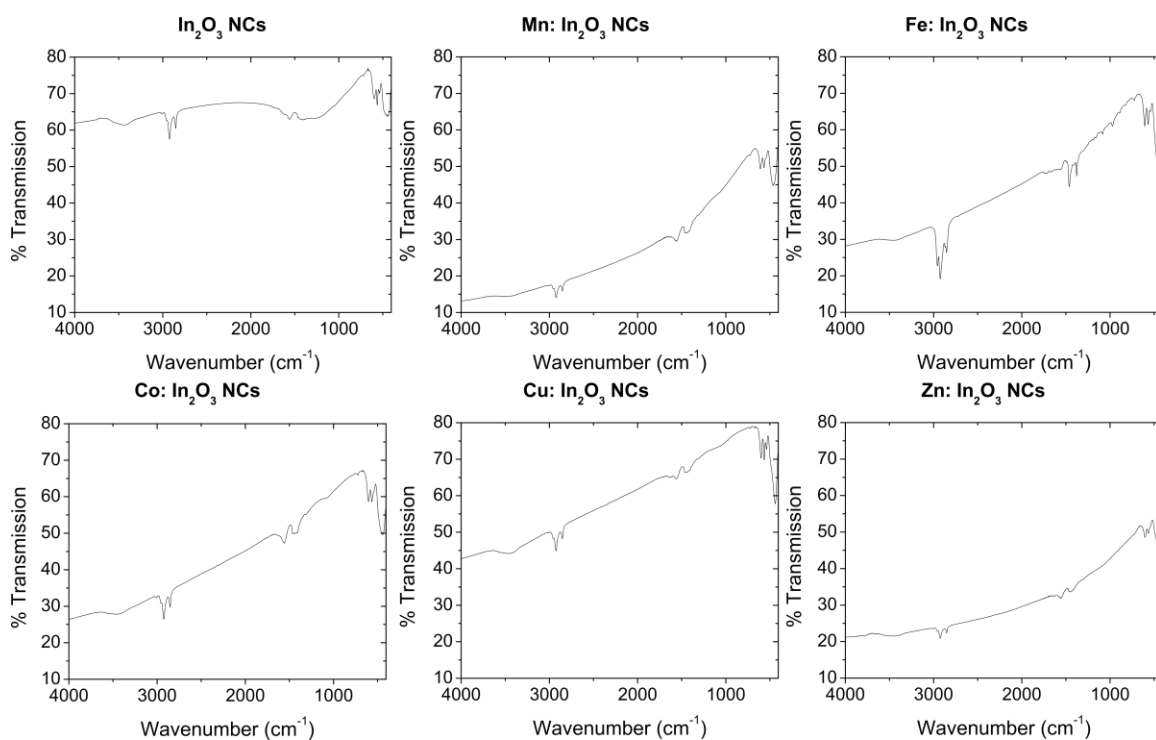
**Figure A3**. FTIR spectra obtained from undoped and doped $In_2O_3$ nanocrystals. Unlike the undoped nanocrystals (top left), which display a weak plasmon resonance ~1400 cm$^{-1}$, the doped nanocrystals display much stronger plasmon absorbances centered at energies > 4000 cm$^{-1}$. The strong absorbance and the shift of the LSPR to higher energies is an indication of an increased concentration of oxygen vacancy formation.

APPENDIX B

SUPPORTING INFORMATION FOR CHAPTER III: THE INFLUENCE OF

NANOCRYSTAL SIZE ON OPTOELECTRONIC PROPERTIES OF

THIN, SOLUTION CAST Sn-DOPED $In_2O_3$ FILMS
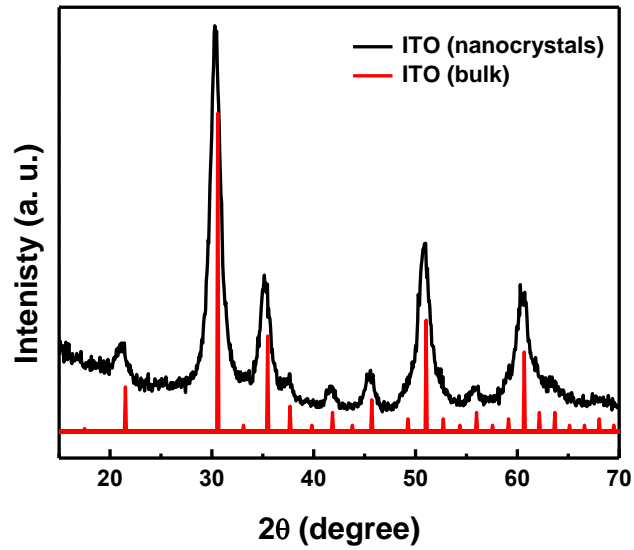


**Figure B1**. Powder XRD of 10.7 nm ITO nanocrystal (black trace) compared to bulk cubic $In_2O_3$ (red trace, JCPDS NO. 76-0152).

*Extraction of optical constants using the Drude model*

All modeling and optical constant extractions of the NIR spectra in Figure 3 were performed in MatLab.

The absorbance of the nanocrystal solution can be modeled with the Beer-Lambert law

$$A = \frac{N\sigma_A L}{\log(10)}$$

where N is the nanocrystal number density (#particles/cm$^{-3}$), $\sigma_A$ is the LSPR absorption cross-section of the nanocrystals, and L is the pathlength of the cuvette. The absorption cross-section can be calculated using

$$\sigma_A = 4\pi k R^3 Imag \left\{ \frac{\varepsilon_{NC}(\omega) - \varepsilon_m}{\varepsilon_{NC}(\omega) + 2\varepsilon_m} \right\}$$

where $\varepsilon_m$ is the dielectric constant of the medium (2.238 for CCl$_4$), $\varepsilon_{NC}$ is the frequency-dependent dielectric function for ITO, $k = \sqrt{\varepsilon_m}\omega/c$, and R is the nanocrystal radius. The frequency-dependent dielectric function for ITO $\varepsilon_{NC}$ is described by

$$\varepsilon_{NC}(\omega) = \varepsilon_\infty - \frac{\omega_p^2}{(\omega^2 + i\omega\Gamma)}$$

where $\varepsilon_\infty$ is the high frequency dielectric constant of ITO (taken as 4), $\omega_p$ is the bulk plasma frequency of the free carriers, and $\Gamma$ is the free carrier damping. The bulk plasma frequency $\omega_p$ is related to $N_e$ through Equation 1 of the main text.
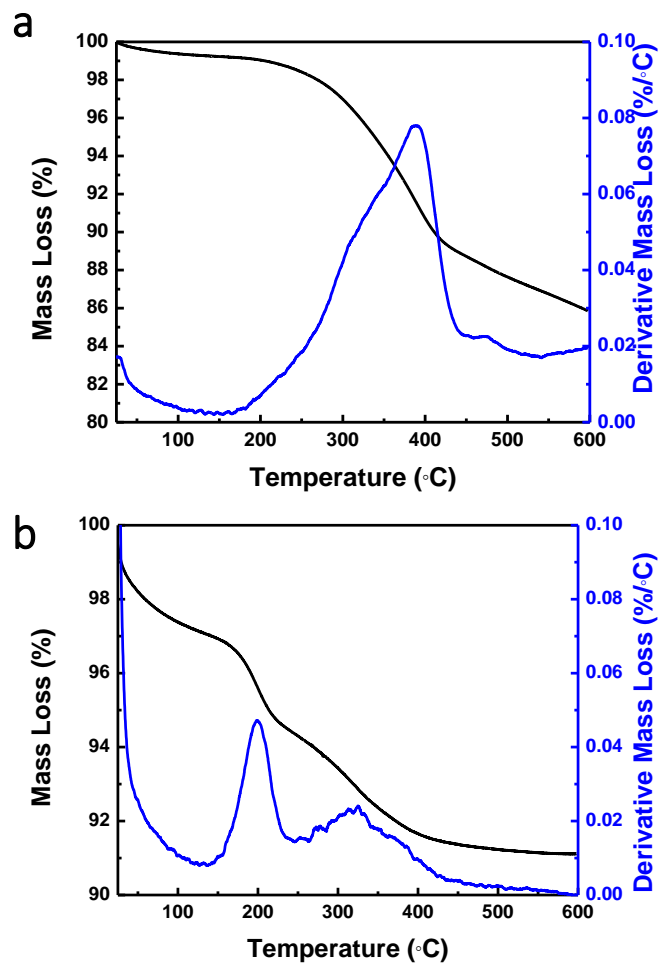
**Figure B2**. TGA analysis of oleate-stabilized ITO nanocrystal (a), mass loss occurs around 375 °C. TGA analysis of formate-stabilized ITO nanocrystals (b) after exposure to 1M formic acid in acetonitrile, main mass loss occurs near 200 °C, and final mass loss occurs around 300 °C. TGA in both cases performed under $N_2$ with a temperature ramp rate of 10 °C/min.
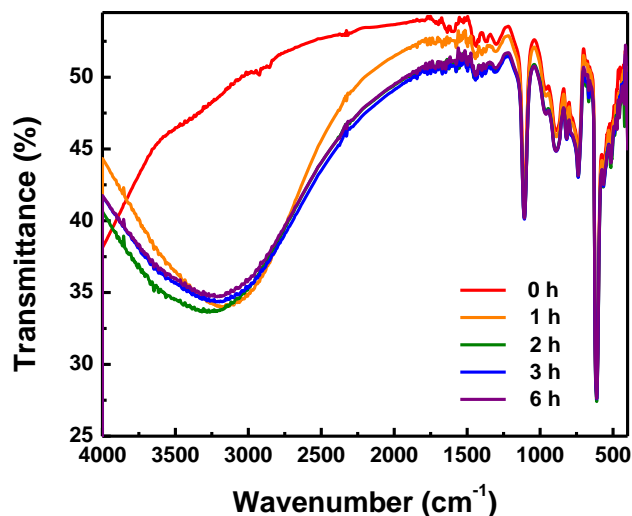
**Figure B3**. FT-IR spectra of ligand exchanged films annealed under reducing atmosphere (95%/5% $N_2$/$H_2$), displaying a redshift in the LSPR and indicate electron delocalization.

*Calculated Interface density for common packing geometries.*

Interface density can be calculated using the average nanocrystal diameter and a common packing density geometry (BCC in this example), where the unit cell volume is:

$$A^3 = \left(\frac{4 \times r}{\sqrt{3}}\right)^3$$

A is the edge length (cm) of the primitive cell and r is the nanocrystal radius (cm). The density of unit cells can be calculated from:

$$\frac{\#_{unit\ cells}}{cm^3} = \frac{1}{A^3}$$

The interface density is equal to the unit cell density multiplied by the coordination number (CN) for the packing geometry (8 for BCC)

$$\frac{\#_{interface}}{cm^3} = \frac{\#_{unit\ cells}}{A^3} \times CN$$

103

SUPPORTING INFORMATION FOR CHAPTER V: RADIAL DOPANT

PLACEMENT FOR TUNING PLASMONIC PROPERTIES

IN METAL OXIDE NANOCRYSTALS
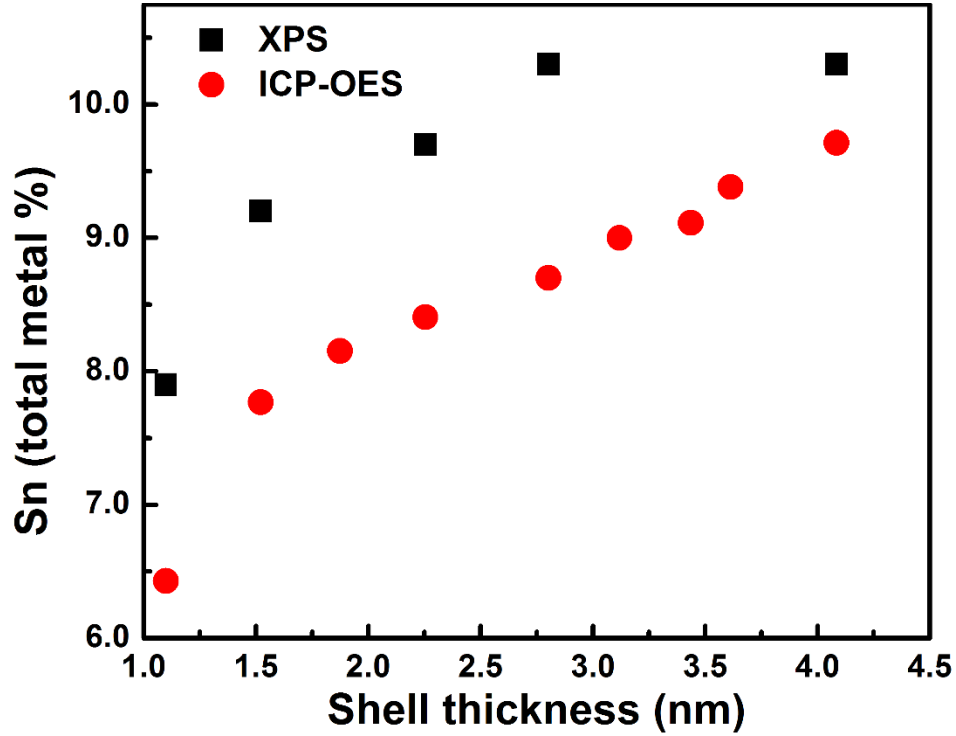


**Figure C1.** Elemental analysis of Sn (plotted as total metal %) via XPS and ICP-OES versus shell thickness for $In_2O_3$/ITO core/shell series. The trend shows an overall increase in Sn with increasing ITO shell thickness. Additionally, measured XPS values are larger than ICP-OES values indicating the dopants are localized in the shell.

**Table C1**. Size and size dispersion from SAXS analysis for the $In_2O_3$/ITO core/shell nanocrystal series. LSPR spectra are shown in Figure 2e in the manuscript.

| Sample | Core size (nm) | Dispersity (1σ, nm) | Shell thickness (nm) |
|---|---|---|---|
| $In_2O_3$ core | 6.3 | 0.8 | - |
| $In_2O_3$/ITO core/shell | 8.5 | 1.0 | 1.1 |
| $In_2O_3$/ITO core/shell | 9.3 | 1.0 | 1.5 |
| $In_2O_3$/ITO core/shell | 10.0 | 1.1 | 1.9 |
| $In_2O_3$/ITO core/shell | 10.8 | 1.2 | 2.3 |
| $In_2O_3$/ITO core/shell | 11.9 | 1.4 | 2.8 |
| $In_2O_3$/ITO core/shell | 12.5 | 1.7 | 3.1 |
| $In_2O_3$/ITO core/shell | 13.1 | 1.8 | 3.4 |
| $In_2O_3$/ITO core/shell | 13.5 | 1.8 | 3.6 |
| $In_2O_3$/ITO core/shell | 14.4 | 2.2 | 4.1 |
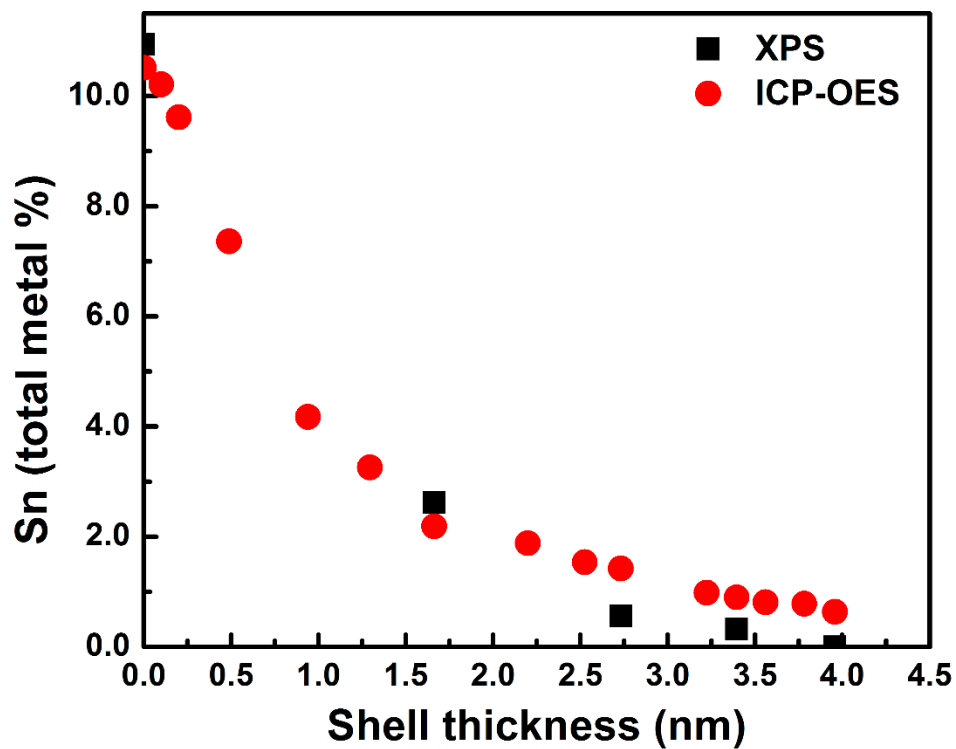
**Figure C2.** Elemental analysis of Sn (plotted as total metal %) via XPS and ICP-OES versus shell thickness for ITO/ $In_2O_3$ core/shell series. The trend shows an overall decrease in Sn with increasing $In_2O_3$ shell thickness. Additionally, XPS values trend to zero indicating the dopants are localized in the core.

**Table C2.** Size and size dispersion from SAXS analysis for the ITO/ $In_2O_3$ core/shell nanocrystal series.

| Sample | Core size (nm) | Dispersity (1σ, nm) | Shell thickness (nm) |
|---|---|---|---|
| ITO core | 5.3 | 2.3 | - |
| ITO/$In_2O_3$ core/shell | 6.3 | 1.4 | 0.5 |
| ITO/$In_2O_3$ core/shell | 7.2 | 1.1 | 0.9 |
| ITO/$In_2O_3$ core/shell | 7.9 | 0.9 | 1.3 |
| ITO/$In_2O_3$ core/shell | 8.7 | 1.0 | 1.7 |
| ITO/$In_2O_3$ core/shell | 9.7 | 1.1 | 2.2 |
| ITO/$In_2O_3$ core/shell | 10.4 | 1.2 | 2.5 |
| ITO/$In_2O_3$ core/shell | 10.8 | 1.2 | 2.7 |
| ITO/$In_2O_3$ core/shell | 11.2 | 1.2 | 2.9 |
| ITO/$In_2O_3$ core/shell | 11.8 | 1.3 | 3.2 |
| ITO/$In_2O_3$ core/shell | 12.1 | 1.3 | 3.4 |
| ITO/$In_2O_3$ core/shell | 12.4 | 1.3 | 3.6 |
| ITO/$In_2O_3$ core/shell | 12.9 | 1.3 | 3.8 |
| ITO/$In_2O_3$ core/shell | 13.2 | 1.3 | 4.0 |
| ITO/$In_2O_3$ core/shell | 13.3 | 1.2 | 4.0 |
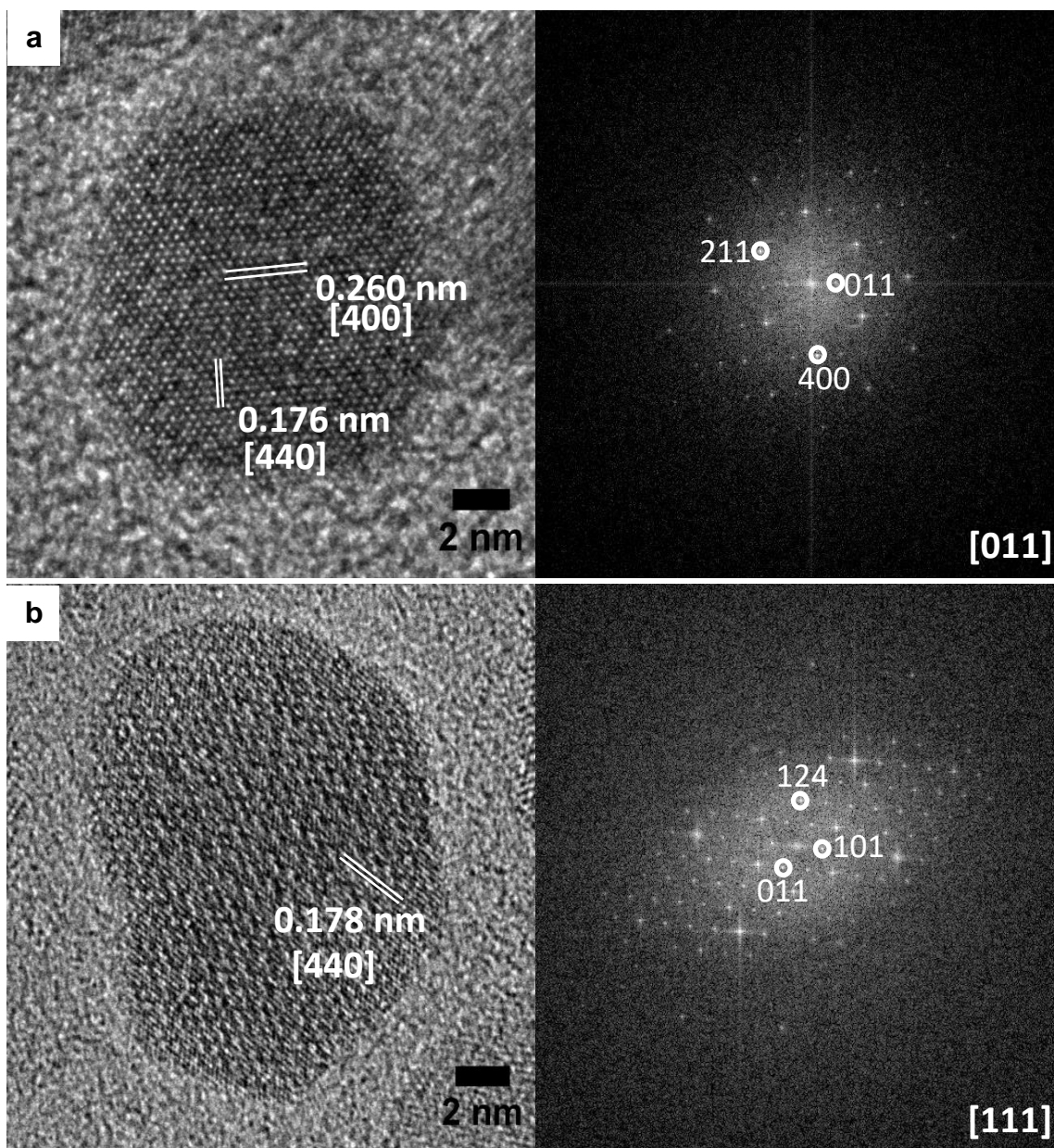
**Figure C3.** HRTEM images of ITO/In$_2$O$_3$ core/shell nanocrystal (**a**) and the In$_2$O$_3$/ITO core/shell nanocrystal (**b**). As shown, no striking structural defects are found in the single crystals. The FFT of the image is shown to the right of the micrographs. The micrograph in **a** is looking down the [011] zone axis, and the micrograph in **b** is down the [111] zone axis.
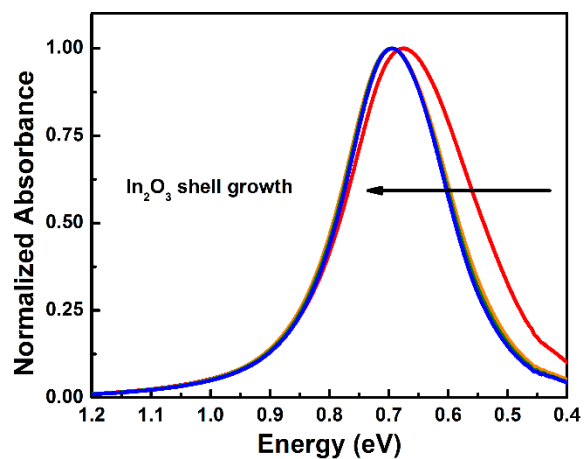
**Figure C4.** NIR spectra of ITO nanocrystal core with sub-namometer shells.

**Table C3.** Size and size dispersion from SAXS analysis for the ITO/In$_2$O$_3$ core/shell nanocrystals with thin undoped shells.

| Sample | Core size (nm) | Dispersity (1σ, nm) |
|---|---|---|
| ITO core | 6.9 | 1.0 |
| ITO/In$_2$O$_3$ core/shell | 7.0 | 1.2 |
| ITO/In$_2$O$_3$ core/shell | 7.1 | 1.1 |
| ITO/In$_2$O$_3$ core/shell | 7.2 | 1.1 |

**Table C4.** Size and composition data for homogeneous ITO and $In_2O_3$/ITO core/shell nanocrystals shown in Figure 4.2g. Sizes and size dispersions are from SAXS analysis. Elemental analyses are derived from XPS and ICP-OES.

| Structure | Size +/- 1σ (SAXS, nm) | Core size (SAXS, nm) | Sn % (ICP-OES) | Sn % (XPS) |
|---|---|---|---|---|
| **ITO homogeneous** | 7.3 ± 1.1 | N/A | 9.98 ± 0.05 | 10.6 ± 0.2 |
| **$In_2O_3$/ITO core/shell** | 14.4 +/- 2.2 | 6.3 +/- 0.8 | 9.71 ± 0.06 | 10.3 ± 0.1 |

**Table C5.** Size and composition for homogeneous ITO and ITO/$In_2O_3$core/shell nanocrystals shown in Figure 4.2h. Size and size dispersion are from SAXS analysis. Elemental analyses are derived from XPS and ICP-OES.

| Structure | Size +/- 1σ (SAXS, nm) | Core size (SAXS, nm) | Sn % (ICP-OES) | Sn % (XPS) |
|---|---|---|---|---|
| **ITO homogeneous** | 6.9 ± 1.0 | N/A | 7.17 ± 0.06 | 7.1 ± 0.2 |
| **ITO/$In_2O_3$ core/shell** | 7.9 +/- 0.9 | 5.3 +/- 2.3 | 7.36 ± 0.04 | 7.5 ± 0.1 |
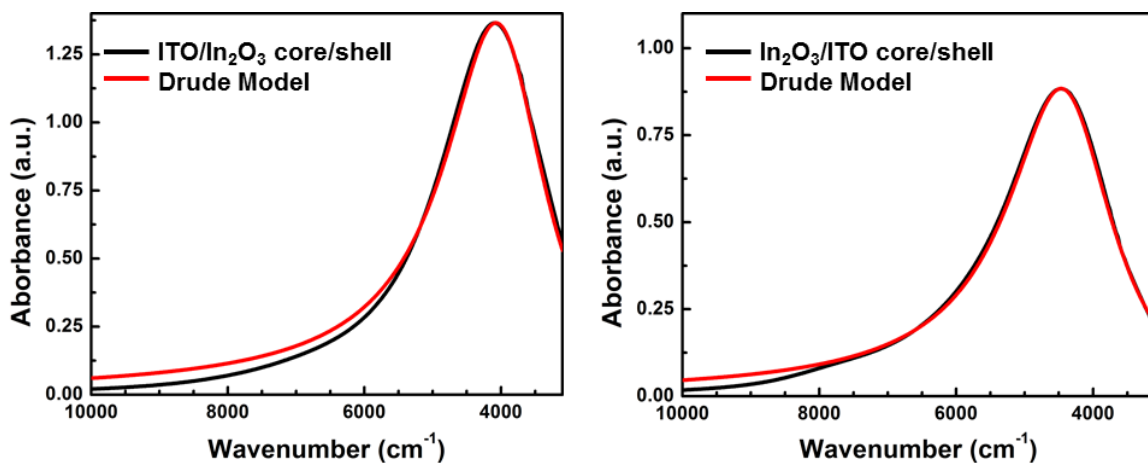
**Figure C5**. Example spectra modeling with the Drude equation of ITO/In$_2$O$_3$ nanocrystals (left) and In$_2$O$_3$/ITO nanocrystals (right). Modeling was performed in MatLab as described in the Experimental section of the main text.

REFERENCES CITED

**Chapter I**

(1)     Liang, X.; Bai, S.; Wang, X.; Dai, X.; Gao, F.; Sun, B.; Ning, Z.; Ye, Z.; Jin, Y. Colloidal Metal Oxide Nanocrystals as Charge Transporting Layers for Solution-Processed Light-Emitting Diodes and Solar Cells. *Chem. Soc. Rev.* **2017**, *46* (6), 1730–1759.

(2)     Kovalenko, M. V.; Manna, L.; Cabot, A.; Hens, Z.; Talapin, D. V.; Kagan, C. R.; Klimov, V. I.; Rogach, A. L.; Reiss, P.; Milliron, D. J.; et al. Prospects of Nanoscience with Nanocrystals. *ACS Nano* **2015**, *9* (2), 1012–1057.

(3)     Cong, Y.; Zhang, J.; Chen, F.; Anpo, M.; He, D. Preparation, Photocatalytic Activity, and Mechanism of Nano-TiO2 Co-Doped with Nitrogen and Iron (III). *J. Phys. Chem. C* **2007**, *111* (28), 10618–10623.

(4)     Xu, A.-W.; Gao, Y.; Liu, H.-Q. The Preparation, Characterization, and Their Photocatalytic Activities of Rare-Earth-Doped TiO2 Nanoparticles. *Journal of Catalysis* **2002**, *207* (2), 151–157.

(5)     Mocatta, D.; Cohen, G.; Schattner, J.; Millo, O.; Rabani, E.; Banin, U. Heavily Doped Semiconductor Nanocrystal Quantum Dots. *Science* **2011**, *332* (6025), 77–81.

(6)     Kriegel, I.; Scotognella, F.; Manna, L. Plasmonic Doped Semiconductor Nanocrystals: Properties, Fabrication, Applications and Perspectives. *Physics Reports* **2017**, *674*, 1–52.

(7)     Runnerstrom, E. L.; Bergerud, A.; Agrawal, A.; Johns, R. W.; Dahlman, C. J.; Singh, A.; Selbach, S. M.; Milliron, D. J. Defect Engineering in Plasmonic Metal Oxide Nanocrystals. *Nano Lett.* **2016**, *16* (5), 3390–3398.

(8)     Ito, D.; Yokoyama, S.; Zaikova, T.; Masuko, K.; Hutchison, J. E. Synthesis of Ligand-Stabilized Metal Oxide Nanocrystals and Epitaxial Core/Shell Nanocrystals via a Lower-Temperature Esterification Process. *ACS Nano* **2014**, *8* (1), 64–75.

(9)     Cooper, S. R.; Plummer, L. K.; Cosby, A. G.; Lenox, P.; Jander, A.; Dhagat, P.; Hutchison, J. E. Insights into the Magnetic Properties of Sub-10 Nm Iron Oxide Nanocrystals through the Use of a Continuous Growth Synthesis. *Chem. Mater.* **2018**, *30* (17), 6053–6062.

(10)    Jansons, A. W.; Hutchison, J. E. Continuous Growth of Metal Oxide Nanocrystals: Enhanced Control of Nanocrystal Size and Radial Dopant Distribution. *ACS Nano* **2016**, *10* (7), 6942–6951.

(11)    Jansons, A. W.; Koskela, K. M.; Crockett, B. M.; Hutchison, J. E. Transition Metal-Doped Metal Oxide Nanocrystals: Efficient Substitutional Doping through a Continuous Growth Process. *Chem. Mater.* **2017**, *29* (19), 8167–8176.

(12) Jansons, A. W.; Plummer, L. K.; Hutchison, J. E. Living Nanocrystals. *Chem. Mater.* **2017**, *29* (13), 5415–5425.

(13) Crockett, B. M.; Jansons, A. W.; Koskela, K. M.; Johnson, D. W.; Hutchison, J. E. Radial Dopant Placement for Tuning Plasmonic Properties in Metal Oxide Nanocrystals. *ACS Nano* **2017**, *11* (8), 7719–7728.

(14) Lee, J.; Zhang, S.; Sun, S. High-Temperature Solution-Phase Syntheses of Metal-Oxide Nanocrystals. *Chem. Mater.* **2013**, *25* (8), 1293–1304.

(15) Deshmukh, R.; Niederberger, M. Mechanistic Aspects in the Formation, Growth and Surface Functionalization of Metal Oxide Nanoparticles in Organic Solvents. *Chemistry – A European Journal* **2017**, *23* (36), 8542–8570.

(16) Johns, R. W.; Bechtel, H. A.; Runnerstrom, E. L.; Agrawal, A.; Lounis, S. D.; Milliron, D. J. Direct Observation of Narrow Mid-Infrared Plasmon Linewidths of Single Metal Oxide Nanocrystals. *Nature Communications* **2016**, *7*, 11583.

(17) Ochsenbein, S. T.; Feng, Y.; Whitaker, K. M.; Badaeva, E.; Liu, W. K.; Li, X.; Gamelin, D. R. Charge-Controlled Magnetism in Colloidal Doped Semiconductor Nanocrystals. *Nature Nanotechnology* **2009**, *4* (10), 681–687.

(18) Iablokov, V.; Barbosa, R.; Pollefeyt, G.; Van Driessche, I.; Chenakin, S.; Kruse, N. Catalytic CO Oxidation over Well-Defined Cobalt Oxide Nanoparticles: Size-Reactivity Correlation. *ACS Catal.* **2015**, *5* (10), 5714–5718.

(19) Kumar, M.; Kumar, A.; Abhyankar, A. C. Influence of Texture Coefficient on Surface Morphology and Sensing Properties of W-Doped Nanocrystalline Tin Oxide Thin Films. *ACS Appl. Mater. Interfaces* **2015**, *7* (6), 3571–3580.

(20) Qiao, L.; Swihart, M. T. Solution-Phase Synthesis of Transition Metal Oxide Nanocrystals: Morphologies, Formulae, and Mechanisms. *Advances in Colloid and Interface Science* **2017**, *244*, 199–266.

(21) Liu, J.; Wu, Z.; Tian, Q.; Wu, W.; Xiao, X. Shape-Controlled Iron Oxide Nanocrystals: Synthesis, Magnetic Properties and Energy Conversion Applications. *CrystEngComm* **2016**, *18* (34), 6303–6326.

(22) De Roo, J.; Van den Broeck, F.; De Keukeleere, K.; Martins, J. C.; Van Driessche, I.; Hens, Z. Unravelling the Surface Chemistry of Metal Oxide Nanocrystals, the Role of Acids and Bases. *J. Am. Chem. Soc.* **2014**, *136* (27), 9650–9657.

(23) Auffan, M.; Rose, J.; Proux, O.; Borschneck, D.; Masion, A.; Chaurand, P.; Hazemann, J.-L.; Chaneac, C.; Jolivet, J.-P.; Wiesner, M. R.; et al. Enhanced Adsorption of Arsenic onto Maghemites Nanoparticles: As(III) as a Probe of the Surface Structure and Heterogeneity. *Langmuir* **2008**, *24* (7), 3215–3222.

(24) Djerdj, I.; Arčon, D.; Jagličić, Z.; Niederberger, M. Nonaqueous Synthesis of Metal Oxide Nanoparticles: Short Review and Doped Titanium Dioxide as Case Study for the Preparation of Transition Metal-Doped Oxide Nanoparticles. *Journal of Solid State Chemistry* **2008**, *181* (7), 1571–1581.

(25)    Niederberger, M. Nonaqueous Sol–Gel Routes to Metal Oxide Nanoparticles. *Acc. Chem. Res.* **2007**, *40* (9), 793–800.

(26)    Niederberger, M.; Garnweitner, G. Organic Reaction Pathways in the Nonaqueous Synthesis of Metal Oxide Nanoparticles. *Chemistry – A European Journal* **2006**, *12* (28), 7282–7302.

(27)    Jang, D. M.; Kwak, I. H.; Kwon, E. L.; Jung, C. S.; Im, H. S.; Park, K.; Park, J. Transition-Metal Doping of Oxide Nanocrystals for Enhanced Catalytic Oxygen Evolution. *J. Phys. Chem. C* **2015**, *119* (4), 1921–1927.

(28)    Comin, A.; Manna, L. New Materials for Tunable Plasmonic Colloidal Nanocrystals. *Chem. Soc. Rev.* **2014**, *43* (11), 3957–3975.

(29)    Sytnyk, M.; Kirchschlager, R.; Bodnarchuk, M. I.; Primetzhofer, D.; Kriegner, D.; Enser, H.; Stangl, J.; Bauer, P.; Voith, M.; Hassel, A. W.; et al. Tuning the Magnetic Properties of Metal Oxide Nanocrystal Heterostructures by Cation Exchange. *Nano Lett.* **2013**, *13* (2), 586–593.

(30)    Zhang, Y.; Kumar Das, G.; Xu, R.; Tan, T. T. Y. Tb-Doped Iron Oxide : Bifunctional Fluorescent and Magnetic Nanocrystals. *Journal of Materials Chemistry* **2009**, *19* (22), 3696–3703.

(31)    Ohno, H. Making Nonmagnetic Semiconductors Ferromagnetic. *Science* **1998**, *281* (5379), 951–956.

(32)    *Microelectronic Materials and Processes*; Levy, R., Ed.; Nato Science Series E:; Springer Netherlands, 1989.

(33)    Galli, G. Solid-State Physics: Doping the Undopable. *Nature* **2005**, *436* (7047), 32–33.

(34)    Norris, D. J.; Efros, A. L.; Erwin, S. C. Doped Nanocrystals. *Science* **2008**, *319* (5871), 1776–1779.

(35)    Buonsanti, R.; Milliron, D. J. Chemistry of Doped Colloidal Nanocrystals. *Chem. Mater.* **2013**, *25* (8), 1305–1317.

(36)    Erwin, S. C.; Zu, L.; Haftel, M. I.; Efros, A. L.; Kennedy, T. A.; Norris, D. J. Doping Semiconductor Nanocrystals. *Nature* **2005**, *436* (7047), 91–94.

(37)    Schimpf, A. M.; Knowles, K. E.; Carroll, G. M.; Gamelin, D. R. Electronic Doping and Redox-Potential Tuning in Colloidal Semiconductor Nanocrystals. *Acc. Chem. Res.* **2015**, *48* (7), 1929–1937.

(38)    Radovanovic, P. V.; Norberg, N. S.; McNally, K. E.; Gamelin, D. R. Colloidal Transition-Metal-Doped ZnO Quantum Dots. *J. Am. Chem. Soc.* **2002**, *124* (51), 15192–15193.

(39)    Djerdj, I.; Garnweitner, G.; Arčon, D.; Pregelj, M.; Jagličić, Z.; Niederberger, M. Diluted Magnetic Semiconductors: Mn/Co-Doped ZnO Nanorods as Case Study. *J. Mater. Chem.* **2008**, *18* (43), 5208–5217.

(40)     Ginley, D. S.; Bright, C. Transparent Conducting Oxides. *MRS Bulletin* **2000**, *25* (8), 15–18.

(41)     Agrawal, A.; Cho, S. H.; Zandi, O.; Ghosh, S.; Johns, R. W.; Milliron, D. J. Localized Surface Plasmon Resonance in Semiconductor Nanocrystals. *Chem. Rev.* **2018**, *118* (6), 3121–3207.

(42)     Ellmer, K. Past Achievements and Future Challenges in the Development of Optically Transparent Electrodes. *Nature Photonics* **2012**, *6* (12), 809–817.

(43)     Granqvist, C. G. Transparent Conductors as Solar Energy Materials: A Panoramic Review. *Solar Energy Materials and Solar Cells* **2007**, *91* (17), 1529–1598.

(44)     Kim, B. H.; Staller, C. M.; Cho, S. H.; Heo, S.; Garrison, C. E.; Kim, J.; Milliron, D. J. High Mobility in Nanocrystal-Based Transparent Conducting Oxide Thin Films. *ACS Nano* **2018**, *12* (4), 3200–3208.

(45)     Llordés, A.; Garcia, G.; Gazquez, J.; Milliron, D. J. Tunable Near-Infrared and Visible-Light Transmittance in Nanocrystal-in-Glass Composites. *Nature* **2013**, *500* (7462), 323–326.

(46)     Runnerstrom, E. L.; Bergerud, A.; Agrawal, A.; Johns, R. W.; Dahlman, C. J.; Singh, A.; Selbach, S. M.; Milliron, D. J. Defect Engineering in Plasmonic Metal Oxide Nanocrystals. *Nano Lett.* **2016**, *16* (5), 3390–3398.

(47)     Global Indium Tin Oxide Market 2016-2020 https://www.technavio.com /report/global-metals-and-minerals-global-indium-tin-oxide-market-2016-2020 (accessed Feb 18, 2019).

(48)     ITO alternatives to gain speed in the $2 billion TCF market https://www.idtechex.com/research/articles/ito-alternatives-to-gain-speed-in-the-2-billion-tcf-market-00004561.asp (accessed Feb 18, 2019).

(49)     Shigesato, Y.; Hayashi, Y.; Haranoh, T. Doping Mechanisms of Tin-doped Indium Oxide Films. *Appl. Phys. Lett.* **1992**, *61* (1), 73–75.

(50)     Luo, L.; Bozyigit, D.; Wood, V.; Niederberger, M. High-Quality Transparent Electrodes Spin-Cast from Preformed Antimony-Doped Tin Oxide Nanocrystals for Thin Film Optoelectronics. *Chem. Mater.* **2013**, *25* (24), 4901–4907.

(51)     Ederth, J.; Johnsson, P.; Niklasson, G. A.; Hoel, A.; Hultåker, A.; Heszler, P.; Granqvist, C. G.; van Doorn, A. R.; Jongerius, M. J.; Burgard, D. Electrical and Optical Properties of Thin Films Consisting of Tin-Doped Indium Oxide Nanoparticles. *Phys. Rev. B* **2003**, *68* (15), 155410.

(52)     Song, J.; Kulinich, S. A.; Li, J.; Liu, Y.; Zeng, H. A General One-Pot Strategy for the Synthesis of High-Performance Transparent-Conducting-Oxide Nanocrystal Inks for All-Solution-Processed Devices. *Angew. Chem. Int. Ed. Engl.* **2015**, *54* (2), 462–466.

(53)     Guo, X.; Liu, X.; Lin, F.; Li, H.; Fan, Y.; Zhang, N. Highly Conductive Transparent Organic Electrodes with Multilayer Structures for Rigid and Flexible Optoelectronics. *Scientific Reports* **2015**, *5*, 10569.

(54)     Li, D.; Lai, W.-Y.; Zhang, Y.-Z.; Huang, W. Printable Transparent Conductive Films for Flexible Electronics. *Advanced Materials* **2018**, *30* (10), 1704738.

(55)     Guillén, C.; Herrero, J. TCO/Metal/TCO Structures for Energy and Flexible Electronics. *Thin Solid Films* **2011**, *520* (1), 1–17.

(56)     Lewis, J. Material Challenge for Flexible Organic Devices. *Materials Today* **2006**, *9* (4), 38–45.

(57)     Fu, F.; Feurer, T.; Jäger, T.; Avancini, E.; Bissig, B.; Yoon, S.; Buecheler, S.; Tiwari, A. N. Low-Temperature-Processed Efficient Semi-Transparent Planar Perovskite Solar Cells for Bifacial and Tandem Applications. *Nature Communications* **2015**, *6*, 8932.

(58)     Nie, S.; Emory, S. R. Probing Single Molecules and Single Nanoparticles by Surface-Enhanced Raman Scattering. *Science* **1997**, *275* (5303), 1102–1106.

(59)     Dieringer, J. A.; Wustholz, K. L.; Masiello, D. J.; Camden, J. P.; Klieinman, S. L.; Schatz, G. C.; Van Duyne, R. P. Surface-Enhanced Raman Excitation Spectroscopy of a Single Rhodamine 6G Molecule. *J. Am. Chem. Soc.* **2009**, *131* (2), 849–854.

(60)     Rosman, C.; Prasad, J.; Neiser, A.; Henkel, A.; Edgar, J.; Sönnichsen, C. Multiplexed Plasmon Sensor for Rapid Label-Free Analyte Detection. *Nano Lett.* **2013**, *13* (7), 3243–3247.

(61)     Larsson, E. M.; Langhammer, C.; Zoric, I.; Kasemo, B. Nanoplasmonic Probes of Catalytic Reactions. *Science* **2009**, *20*, 1091–1094.

(62)     Mendelsberg, R. J.; McBride, P. M.; Duong, J. T.; Bailey, M. J.; Llordes, A.; Milliron, D. J.; Helms, B. A. Dispersible Plasmonic Doped Metal Oxide Nanocrystal Sensors That Optically Track Redox Reactions in Aqueous Media with Single-Electron Sensitivity. *Advanced Optical Materials* **2015**, *3* (9), 1293–1300.

(63)     Huang, X.; El-Sayed, I. H.; Qian, W.; El-Sayed, M. A. Cancer Cell Imaging and Photothermal Therapy in the Near-Infrared Region by Using Gold Nanorods. *J. Am. Chem. Soc.* **2006**, *128* (6), 2112–2120.

(64)     Lounis, S. D.; Runnerstrom, E. L.; Bergerud, A.; Nordlund, D.; Milliron, D. J. Influence of Dopant Distribution on the Plasmonic Properties of Indium Tin Oxide Nanocrystals. *J. Am. Chem. Soc.* **2014**, *136* (19), 7110–7116. https://doi.org/10.1021/ja502541z.

## Chapter II

(1)     Levy, R. *Microelectronic Materials and Processes*; Springer Science & Business Media, 2012; Vol. 164.

(2)     Ohno, H. Making Nonmagnetic Semiconductors Ferromagnetic. *Science* **1998**, *281*, 951–956.

(3)     Talapin, D. V.; Lee, J.-S.; Kovalenko, M. V.; Shevchenko, E. V. Prospects of Colloidal Nanocrystals for Electronic and Optoelectronic Applications. *Chem. Rev.* **2010**, *110*, 389–458.

(4)     Kovalenko, M. V.; Manna, L.; Cabot, A.; Hens, Z.; Talapin, D. V.; Kagan, C. R.; Klimov, V. I.; Rogach, A. L.; Reiss, P.; Milliron, D. J.; *et al.* Prospects of Nanoscience with Nanocrystals. *ACS Nano* **2015**, *9*, 1012–1057.

(5)     Liang, X.; Bai, S.; Wang, X.; Dai, X.; Gao, F.; Sun, B.; Ning, Z.; Ye, Z.; Jin, Y. Colloidal Metal Oxide Nanocrystals as Charge Transporting Layers for Solution-Processed Light-Emitting Diodes and Solar Cells. *Chem. Soc. Rev.* **2017**.

(6)     Saleh, N. B.; Milliron, D. J.; Aich, N.; Katz, L. E.; Liljestrand, H. M.; Kirisits, M. J. Importance of Doping, Dopant Distribution, and Defects on Electronic Band Structure Alteration of Metal Oxide Nanoparticles: Implications for Reactive Oxygen Species. *Sci. Total Environ.* **2016**, *568*, 926–932.

(7)     Furdyna, J. K. Diluted Magnetic Semiconductors. *J. Appl. Phys.* **1988**, *64*, R29–R64.

(8)     Ochsenbein, S. T.; Gamelin, D. R. Quantum Oscillations in Magnetically Doped Colloidal Nanocrystals. *Nat Nano* **2011**, *6*, 112–115.

(9)     Ochsenbein, S. T.; Feng, Y.; Whitaker, K. M.; Badaeva, E.; Liu, W. K.; Li, X.; Gamelin, D. R. Charge-Controlled Magnetism in Colloidal Doped Semiconductor Nanocrystals. *Nat Nano* **2009**, *4*, 681–687.

(10)    Liu, W. K.; Whitaker, K. M.; Kittilstved, K. R.; Gamelin, D. R. Stable Photogenerated Carriers in Magnetic Semiconductor Nanocrystals. *J. Am. Chem. Soc.* **2006**, *128*, 3910–3911.

(11)    Stowell, C. A.; Wiacek, R. J.; Saunders, A. E.; Korgel, B. A. Synthesis and Characterization of Dilute Magnetic Semiconductor Manganese-Doped Indium Arsenide Nanocrystals. *Nano Lett.* **2003**, *3*, 1441–1447.

(12)    Somaskandan, K.; Tsoi, G. M.; Wenger, L. E.; Brock, S. L. Isovalent Doping Strategy for Manganese Introduction into III-V Diluted Magnetic Semiconductor Nanoparticles: InP:Mn. *Chem. Mater.* **2005**, *17*, 1190–1198.

(13)    Lin, J.; Hu, D.-D.; Zhang, Q.; Li, D.-S.; Wu, T.; Bu, X.; Feng, P. Improving Photoluminescence Emission Efficiency of Nanocluster-Based Materials by in Situ Doping Synthetic Strategy. *J. Phys. Chem. C* **2016**, *120*, 29390–29396.

(14)     Mocatta, D.; Cohen, G.; Schattner, J.; Millo, O.; Rabani, E.; Banin, U. Heavily Doped Semiconductor Nanocrystal Quantum Dots. *Science* **2011**, *332*, 77–81.

(15)     Pradhan, N.; Goorskey, D.; Thessing, J.; Peng, X. An Alternative of CdSe Nanocrystal Emitters: Pure and Tunable Impurity Emissions in ZnSe Nanocrystals. *J. Am. Chem. Soc.* **2005**, *127*, 17586–17587.

(16)     Pu, C.; Qin, H.; Gao, Y.; Zhou, J.; Wang, P.; Peng, X. Synthetic Control of Exciton Behavior in Colloidal Quantum Dots. *J. Am. Chem. Soc.* **2017**, *139*, 3302–3311.

(17)     Deng, Z.; Tong, L.; Flores, M.; Lin, S.; Cheng, J.-X.; Yan, H.; Liu, Y. High-Quality Manganese-Doped Zinc Sulfide Quantum Rods with Tunable Dual-Color and Multiphoton Emissions. *J. Am. Chem. Soc.* **2011**, *133*, 5389–5396.

(18)     Wu, S.; Han, G.; Milliron, D. J.; Aloni, S.; Altoe, V.; Talapin, D. V.; Cohen, B. E.; Schuck, P. J. Non-Blinking and Photostable Upconverted Luminescence from Single Lanthanide-Doped Nanocrystals. *Proc. Natl. Acad. Sci.* **2009**, *106*, 10917–10921.

(19)     Ostrowski, A. D.; Chan, E. M.; Gargas, D. J.; Katz, E. M.; Han, G.; Schuck, P. J.; Milliron, D. J.; Cohen, B. E. Controlled Synthesis and Single-Particle Imaging of Bright, Sub-10 Nm Lanthanide-Doped Upconverting Nanocrystals. *ACS Nano* **2012**, *6*, 2686–2692.

(20)     Bradshaw, L. R.; Knowles, K. E.; McDowall, S.; Gamelin, D. R. Nanocrystals for Luminescent Solar Concentrators. *Nano Lett.* **2015**, *15*, 1315–1323.

(21)     Knowles, K. E.; Hartstein, K. H.; Kilburn, T. B.; Marchioro, A.; Nelson, H. D.; Whitham, P. J.; Gamelin, D. R. Luminescent Colloidal Semiconductor Nanocrystals Containing Copper: Synthesis, Photophysics, and Applications. *Chem. Rev.* **2016**, *116*, 10820–10851.

(22)     Walter, M. G.; Warren, E. L.; McKone, J. R.; Boettcher, S. W.; Mi, Q.; Santori, E. A.; Lewis, N. S. Solar Water Splitting Cells. *Chem. Rev.* **2010**, *110*, 6446–6473.

(23)     Cong, Y.; Zhang, J.; Chen, F.; Anpo, M.; He, D. Preparation, Photocatalytic Activity, and Mechanism of Nano-$TiO_2$ Co-Doped with Nitrogen and Iron (III). *J. Phys. Chem. C* **2007**, *111*, 10618–10623.

(24)     Xu, A.-W.; Gao, Y.; Liu, H.-Q. The Preparation, Characterization, and Their Photocatalytic Activities of Rare-Earth-Doped $TiO_2$ Nanoparticles. *J. Catal.* **2002**, *207*, 151–157.

(25)     Kriegel, I.; Scotognella, F.; Manna, L. Plasmonic Doped Semiconductor Nanocrystals: Properties, Fabrication, Applications and Perspectives. *Plasmonic Doped Semicond. Nanocrystals Prop. Fabr. Appl. Perspect.* **2017**, *674*, 1–52.

(26)     Comin, A.; Manna, L. New Materials for Tunable Plasmonic Colloidal Nanocrystals. *Chem. Soc. Rev.* **2014**, *43*, 3957–3975.

(27)     Della Gaspera, E.; Chesman, A. S. R.; van Embden, J.; Jasieniak, J. J. Non-Injection Synthesis of Doped Zinc Oxide Plasmonic Nanocrystals. *ACS Nano* **2014**, *8*, 9154–9163.

(28)     Lounis, S. D.; Runnerstrom, E. L.; Llordés, A.; Milliron, D. J. Defect Chemistry and Plasmon Physics of Colloidal Metal Oxide Nanocrystals. *J. Phys. Chem. Lett.* **2014**, *5*, 1564–1574.

(29)     Runnerstrom, E. L.; Bergerud, A.; Agrawal, A.; Johns, R. W.; Dahlman, C. J.; Singh, A.; Selbach, S. M.; Milliron, D. J. Defect Engineering in Plasmonic Metal Oxide Nanocrystals. *Nano Lett.* **2016**, *16*, 3390–3398.

(30)     Schimpf, A. M.; Lounis, S. D.; Runnerstrom, E. L.; Milliron, D. J.; Gamelin, D. R. Redox Chemistries and Plasmon Energies of Photodoped $In_2O_3$ and Sn-Doped $In_2O_3$ (ITO) Nanocrystals. *J. Am. Chem. Soc.* **2015**, *137*, 518–524.

(31)     Agrawal, A.; Johns, R. W.; Milliron, D. J. Control of Localized Surface Plasmon Resonances in Metal Oxide Nanocrystals. *Annu. Rev. Mater. Res.* **2017**, *47*, 1-31.

(32)     Johns, R. W.; Bechtel, H. A.; Runnerstrom, E. L.; Agrawal, A.; Lounis, S. D.; Milliron, D. J. Direct Observation of Narrow Mid-Infrared Plasmon Linewidths of Single Metal Oxide Nanocrystals. *Nat. Commun.* **2016**, *7*, 11583.

(33)     Schimpf, A. M.; Knowles, K. E.; Carroll, G. M.; Gamelin, D. R. Electronic Doping and Redox-Potential Tuning in Colloidal Semiconductor Nanocrystals. *Acc. Chem. Res.* **2015**, *48*, 1929–1937.

(34)     Radovanovic, P. V.; Norberg, N. S.; McNally, K. E.; Gamelin, D. R. Colloidal Transition-Metal-Doped ZnO Quantum Dots. *J. Am. Chem. Soc.* **2002**, *124*, 15192–15193.

(35)     Djerdj, I.; Garnweitner, G.; Arcon, D.; Pregelj, M.; Jaglicic, Z.; Niederberger, M. Diluted Magnetic Semiconductors: Mn/Co-Doped ZnO Nanorods as Case Study. *J. Mater. Chem.* **2008**, *18*, 5208–5217.

(36)     Djerdj, I.; Arčon, D.; Jagličić, Z.; Niederberger, M. Nonaqueous Synthesis of Metal Oxide Nanoparticles: Short Review and Doped Titanium Dioxide as Case Study for the Preparation of Transition Metal-Doped Oxide Nanoparticles. *Solid State Chem. Nanoscale Achiev. Chall. Oppor.* **2008**, *181*, 1571–1581.

(37)     Bilecka, I.; Luo, L.; Djerdj, I.; Rossell, M. D.; Jagodič, M.; Jagličić, Z.; Masubuchi, Y.; Kikkawa, S.; Niederberger, M. Microwave-Assisted Nonaqueous Sol−Gel Chemistry for Highly Concentrated ZnO-Based Magnetic Semiconductor Nanocrystals. *J. Phys. Chem. C* **2011**, *115*, 1484–1495.

(38)     Viswanatha, R.; Sapra, S.; Sen Gupta, S.; Satpati, B.; Satyam, P. V.; Dev, B. N.; Sarma, D. D. Synthesis and Characterization of Mn-Doped ZnO Nanocrystals. *J. Phys. Chem. B* **2004**, *108*, 6303–6310.

(39)     Farvid, S. S.; Ju, L.; Worden, M.; Radovanovic, P. V. Colloidal Chromium-Doped $In_2O_3$ Nanocrystals as Building Blocks for High-TC Ferromagnetic Transparent Conducting Oxide Structures. *J. Phys. Chem. C* **2008**, *112*, 17755–17759.

(40) Liang, X.; Ren, Y.; Bai, S.; Zhang, N.; Dai, X.; Wang, X.; He, H.; Jin, C.; Ye, Z.; Chen, Q.; *et al.* Colloidal Indium-Doped Zinc Oxide Nanocrystals with Tunable Work Function: Rational Synthesis and Optoelectronic Applications. *Chem. Mater.* **2014**, *26*, 5169–5178.

(41) Buonsanti, R.; Llordes, A.; Aloni, S.; Helms, B. A.; Milliron, D. J. Tunable Infrared Absorption and Visible Transparency of Colloidal Aluminum-Doped Zinc Oxide Nanocrystals. *Nano Lett.* **2011**, *11*, 4706–4710.

(42) Gilstrap, R. A.; Capozzi, C. J.; Carson, C. G.; Gerhardt, R. A.; Summers, C. J. Synthesis of a Nonagglomerated Indium Tin Oxide Nanoparticle Dispersion. *Adv. Mater.* **2008**, *20*, 4163–4166.

(43) Choi, S.-I.; Nam, K. M.; Park, B. K.; Seo, W. S.; Park, J. T. Preparation and Optical Properties of Colloidal, Monodisperse, and Highly Crystalline ITO Nanoparticles. *Chem. Mater.* **2008**, *20*, 2609–2611.

(44) Sun, Z.; He, J.; Kumbhar, A.; Fang, J. Nonaqueous Synthesis and Photoluminescence of ITO Nanoparticles. *Langmuir* **2010**, *26*, 4246–4250.

(45) Della Gaspera, E.; Bersani, M.; Cittadini, M.; Guglielmi, M.; Pagani, D.; Noriega, R.; Mehra, S.; Salleo, A.; Martucci, A. Low-Temperature Processed Ga-Doped ZnO Coatings from Colloidal Inks. *J. Am. Chem. Soc.* **2013**, *135*, 3439–3448.

(46) Norris, D. J.; Efros, A. L.; Erwin, S. C. Doped Nanocrystals. *Science* **2008**, *319*, 1776–1779.

(47) Dalpian, G. M.; Chelikowsky, J. R. Self-Purification in Semiconductor Nanocrystals. *Phys. Rev. Lett.* **2006**, *96*, 226802.

(48) Erwin, S. C.; Zu, L.; Haftel, M. I.; Efros, A. L.; Kennedy, T. A.; Norris, D. J. Doping Semiconductor Nanocrystals. *Nature* **2005**, *436*, 91–94.

(49) Galli, G. Solid-State Physics: Doping the Undopable. *Nature* **2005**, *436*, 32–33.

(50) Buonsanti, R.; Milliron, D. J. Chemistry of Doped Colloidal Nanocrystals. *Chem. Mater.* **2013**, *25*, 1305–1317.

(51) Du, M.-H.; Erwin, S. C.; Efros, A. L. Trapped-Dopant Model of Doping in Semiconductor Nanocrystals. *Nano Lett.* **2008**, *8*, 2878–2882.

(52) Lounis, S. D.; Runnerstrom, E. L.; Bergerud, A.; Nordlund, D.; Milliron, D. J. Influence of Dopant Distribution on the Plasmonic Properties of Indium Tin Oxide Nanocrystals. *J. Am. Chem. Soc.* **2014**, *136*, 7110–7116.

(53) Crockett, B. M.; Jansons, A. W.; Koskela, K. M.; Johnson, D. W.; Hutchison, J. E. Radial Dopant Placement for Tuning Plasmonic Properties in Metal Oxide Nanocrystals. *ACS Nano* **2017**, 11, 7719-7728.

(54) Bryan, J. D.; Gamelin, D. R. Doped Semiconductor Nanocrystals: Synthesis, Characterization, Physical Properties, and Applications. In *Progress in Inorganic Chemistry*; John Wiley & Sons, Inc., 2005; pp. 47–126.

(55)     Zhang, N.; Wang, X.; Ye, Z.; Jin, Y. A Quantitative Study of Chemical Kinetics for the Synthesis of Doped Oxide Nanocrystals Using FTIR. *Sci. Rep.* **2014**, *4*, 4353.

(56)     Jansons, A. W.; Hutchison, J. E. Continuous Growth of Metal Oxide Nanocrystals: Enhanced Control of Nanocrystal Size and Radial Dopant Distribution. *ACS Nano* **2016**, *10*, 6942–6951.

(57)     Jansons, A. W.; Plummer, L. K.; Hutchison, J. E. Living Nanocrystals. *Chem. Mater.* **2017**, *29*, 5415–5425.

(58)     Song, J.; Kulinich, S. A.; Li, J.; Liu, Y.; Zeng, H. A General One-Pot Strategy for the Synthesis of High-Performance Transparent-Conducting-Oxide Nanocrystal Inks for All-Solution-Processed Devices. *Angew. Chem. Int. Ed.* **2015**, *54*, 462–466.

(59)     Ito, D.; Yokoyama, S.; Zaikova, T.; Masuko, K.; Hutchison, J. E. Synthesis of Ligand-Stabilized Metal Oxide Nanocrystals and Epitaxial Core/Shell Nanocrystals via a Lower-Temperature Esterification Process. *ACS Nano* **2014**, *8*, 64–75.

(60)     Niederberger, M. Nonaqueous Sol–Gel Routes to Metal Oxide Nanoparticles. *Acc. Chem. Res.* **2007**, *40*, 793–800.

(61)     Frank, G.; Köstlin, H. Electrical Properties and Defect Model of Tin-Doped Indium Oxide Layers. *Appl. Phys. A* **1982**, *27*, 197–206.

(62)     Kanehara, M.; Koike, H.; Yoshinaga, T.; Teranishi, T. Indium Tin Oxide Nanoparticles with Compositionally Tunable Surface Plasmon Resonance Frequencies in the Near-IR Region. *J. Am. Chem. Soc.* **2009**, *131*, 17736–17737.

(63)     Radovanovic, P. V. Defect-Induced Optical and Magnetic Properties of Colloidal Transparent Conducting Oxide Nanocrystals. In *Functional Metal Oxides*; Wiley-VCH Verlag GmbH & Co. KGaA, 2013; pp. 163–194.

(64)     Shannon, R. Revised Effective Ionic Radii and Systematic Studies of Interatomic Distances in Halides and Chalcogenides. *Acta Crystallogr. Sect. A* **1976**, *32*, 751–767.

(65)     Schwartz, D. A.; Norberg, N. S.; Nguyen, Q. P.; Parker, J. M.; Gamelin, D. R. Magnetic Quantum Dots: Synthesis, Spectroscopy, and Magnetism of $Co^{2+}$- and $Ni^{2+}$-Doped ZnO Nanocrystals. *J. Am. Chem. Soc.* **2003**, *125*, 13205–13218.

(66)     van Enckevort, W. J. P.; van der Berg, A. C. J. F.; Kreuwel, K. B. G.; Derksen, A. J.; Couto, M. S. Impurity Blocking of Growth Steps: Experiments and Theory. *Cryst. Growth 1995* **1996**, *166*, 156–161.

(67)     Yang, Y.; Jin, Y.; He, H.; Wang, Q.; Tu, Y.; Lu, H.; Ye, Z. Dopant-Induced Shape Evolution of Colloidal Nanocrystals: The Case of Zinc Oxide. *J. Am. Chem. Soc.* **2010**, *132*, 13381–13394.

(68) Tanuma, S.; Powell, C. J.; Penn, D. R. Calculations of Electron Inelastic Mean Free Paths. V. Data for 14 Organic Compounds over the 50–2000 eV Range. *Surf. Interface Anal.* **1994**, *21*, 165–176.

(69) Farvid, S. S.; Dave, N.; Wang, T.; Radovanovic, P. V. Dopant-Induced Manipulation of the Growth and Structural Metastability of Colloidal Indium Oxide Nanocrystals. *J. Phys. Chem. C* **2009**, *113*, 15928–15933.

(70) Farvid, S. S.; Sabergharesou, T.; Hutfluss, L. N.; Hegde, M.; Prouzet, E.; Radovanovic, P. V. Evidence of Charge-Transfer Ferromagnetism in Transparent Diluted Magnetic Oxide Nanocrystals: Switching the Mechanism of Magnetic Interactions. *J. Am. Chem. Soc.* **2014**, *136*, 7669–7679.

(71) Roisnel, T.; Rodríquez-Carvajal, J. WinPLOTR: A Windows Tool for Powder Diffraction Pattern Analysis. In *Materials Science Forum*; Transtec Publications; 1999, 2001; Vol. 378, pp. 118–123.

(72) Denton, A. R.; Ashcroft, N. W. Vegard's Law. *Phys. Rev. A* **1991**, *43*, 3161–3164.

(73) Perebeinos, V.; Chan, S.-W.; Zhang, F. "Madelung Model" Prediction for Dependence of Lattice Parameter on Nanocrystal Size. *Solid State Commun.* **2002**, *123*, 295–297.

(74) González, G. B.; Cohen, J. B.; Hwang, J.-H.; Mason, T. O.; Hodges, J. P.; Jorgensen, J. D. Neutron Diffraction Study on the Defect Structure of Indium–tin–oxide. *J. Appl. Phys.* **2001**, *89*, 2550–2555.

(75) Stanek, C. R.; McClellan, K. J.; Uberuaga, B. P.; Sickafus, K. E.; Levy, M. R.; Grimes, R. W. Determining the Site Preference of Trivalent Dopants in Bixbyite Sesquioxides by Atomic-Scale Simulations. *Phys. Rev. B* **2007**, *75*, 134101.

(76) Lever, A. B. P. *Inorganic Electronic Spectroscopy*; Elsevier: New York: Amsterdam ; New York, 1984.

(77) Garnet, N. S.; Ghodsi, V.; Hutfluss, L. N.; Yin, P.; Hegde, M.; Radovanovic, P. V. Probing the Role of Dopant Oxidation State in the Magnetism of Diluted Magnetic Oxides Using Fe-Doped $In_2O_3$ and $SnO_2$ Nanocrystals. *J. Phys. Chem. C* **2017**, *121*, 1918–1927.

(78) Singhal, A.; Achary, S. N.; Manjanna, J.; Jayakumar, O. D.; Kadam, R. M.; Tyagi, A. K. Colloidal Fe-Doped Indium Oxide Nanoparticles: Facile Synthesis, Structural, and Magnetic Properties. *J. Phys. Chem. C* **2009**, *113*, 3600–3606.

(79) Hakimi, A. M. H. R.; Blamire, M. G.; Heald, S. M.; Alshammari, M. S.; Alqahtani, M. S.; Score, D. S.; Blythe, H. J.; Fox, A. M.; Gehring, G. A. Donor-Band Ferromagnetism in Cobalt-Doped Indium Oxide. *Phys. Rev. B* **2011**, *84*, 085201.

(80) Liu, D.; Lei, W. W.; Zou, B.; Yu, S. D.; Hao, J.; Wang, K.; Liu, B. B.; Cui, Q. L.; Zou, G. T. High-Pressure X-Ray Diffraction and Raman Spectra Study of Indium Oxide. *J. Appl. Phys.* **2008**, *104*, 083506.

(81)     Tang, L.-M.; Wang, L.-L.; Wang, D.; Liu, J.-Z.; Chen, K.-Q. Donor-Donor Binding in $In_2O_3$: Engineering Shallow Donor Levels. *J. Appl. Phys.* **2010**, *107*, 083704.

(82)     Faucheaux, J. A.; Stanton, A. L. D.; Jain, P. K. Plasmon Resonances of Semiconductor Nanocrystals: Physical Principles and New Opportunities. *J. Phys. Chem. Lett.* **2014**, *5*, 976–985.

(83)     Liu, X.; Swihart, M. T. Heavily-Doped Colloidal Semiconductor and Metal Oxide Nanocrystals: An Emerging New Class of Plasmonic Nanomaterials. *Chem. Soc. Rev.* **2014**, *43*, 3908–3920.

(84)     Luther, J. M.; Jain, P. K.; Ewers, T.; Alivisatos, A. P. Localized Surface Plasmon Resonances Arising from Free Carriers in Doped Quantum Dots. *Nat Mater* **2011**, *10*, 361–366.

(85)     Korotcenkov, G.; Boris, I.; Brinzari, V.; Golovanov, V.; Lychkovsky, Y.; Karkotsky, G.; Cornet, A.; Rossinyol, E.; Rodrigue, J.; Cirera, A. Gas-Sensing Characteristics of One-Electrode Gas Sensors Based on Doped $In_2O_3$ Ceramics. *17th Euopean Conf. Solid-State Transducers Univ. Minho Guimares Port. Sept. 21-24 2003* **2004**, *103*, 13–22.

(86)     Elouali, S.; Bloor, L. G.; Binions, R.; Parkin, I. P.; Carmalt, C. J.; Darr, J. A. Gas Sensing with Nano-Indium Oxides ($In_2O_3$) Prepared via Continuous Hydrothermal Flow Synthesis. *Langmuir* **2012**, *28*, 1879–1885.

(87)     Sysoev, V. V.; Button, B. K.; Wepsiec, K.; Dmitriev, S.; Kolmakov, A. Toward the Nanoscopic "Electronic Nose": Hydrogen vs Carbon Monoxide Discrimination with an Array of Individual Metal Oxide Nano- and Mesowire Sensors. *Nano Lett.* **2006**, *6*, 1584–1588.

(88)     Mani, G. K.; Rayappan, J. B. B. Influence of Copper Doping on Structural, Optical and Sensing Properties of Spray Deposited Zinc Oxide Thin Films. *J. Alloys Compd.* **2014**, *582*, 414–419.

(89)     Klingshirn, C.; Fallert, J.; Zhou, H.; Sartor, J.; Thiele, C.; Maier-Flaig, F.; Schneider, D.; Kalt, H. 65 Years of ZnO Research – Old and Very Recent Results. *Phys. Status Solidi B* **2010**, *247*, 1424–1447.

(90)     Liu, C. M.; Liu, W. L.; Chen, W. J.; Hsieh, S. H.; Tsai, T. K.; Yang, L. C. ITO as a Diffusion Barrier Between Si and Cu. *J. Electrochem. Soc.* **2005**, *152*, G234–G239.

(91)     Prenesti, E.; Daniele, P. G.; Toso, S. Visible Spectrophotometric Determination of Metal Ions: The Influence of Structure on Molar Absorptivity Value of copper(II) Complexes in Aqueous Solution. *Anal. Chim. Acta* **2002**, *459*, 323–336.

(92)     Hathaway, B.; Duggan, M.; Murphy, A.; Mullane, J.; Power, C.; Walsh, A.; Walsh, B. The Stereochemistry and Electronic Properties of Fluxional Six-Coordinate copper(II) Complexes. *Coord. Chem. Rev.* **1981**, *36*, 267–324.

(93)  Wen, S. J.; Couturier, G.; Campet, G.; Portier, J.; Claverie, J. Transport Properties of Copper-Doped Indium Oxide and Indium Tin Oxide Ceramics. *Phys. Status Solidi A* **1992**, *130*, 407–414.

(94)  Ilavsky, J.; Jemian, P. R. Irena: Tool Suite for Modeling and Analysis of Small-Angle Scattering. *J. Appl. Crystallogr.* **2009**, *42*, 347–353.

(95)  Schneider, C. A.; Rasband, W. S.; Eliceiri, K. W. NIH Image to ImageJ: 25 Years of Image Analysis. *Nat Meth* **2012**, *9*, 671–675.

## Chapter III

(1)  Ginley, D. S.; Bright, C. Transparent Conducting Oxides. *MRS Bull.* **2000**, *25*, 15–18.

(2)  Ellmer, K. Past Achievements and Future Challenges in the Development of Optically Transparent Electrodes. *Nat. Photonics* **2012**, *6*, 809–817.

(3)  Granqvist, C. G. Transparent Conductors as Solar Energy Materials: A Panoramic Review. *Sol. Energy Mater. Sol. Cells* **2007**, *91*, 1529–1598.

(4)  Kim, H. B.; Staller, C. M.; Cho, S. H.; Heo, S.; Garrison, C. E.; Kim, J.; Milliron, D. J. High Mobility in Nanocrystal-Based Transparent Conducting Oxide Thin Films. *ACS Nano* **2018**, *12*, 3200–3208.

(5)  Runnerstrom, E. L.; Llordés, A.; Lounis, S. D.; Milliron, D. J. Nanostructured Electrochromic Smart Windows: Traditional Materials and NIR-Selective Plasmonic Nanocrystals. *Chem. Comm.* **2014**, *73*, 10555–10572

(6)  Llordés, A.; Garcia, G.; Gazquez, J.; Milliron, D. J. Tunable Near-Infrared and Visible-Light Transmittance in Nanocrystal-in-Glass Composites. *Nature* **2013**, *500*, 323–326.

(7)  Luo, L.; Bozyigit, D.; Wood, V.; Niederberger, M. High-Quality Transparent Electrodes Spin-Cast from Preformed Antimony-Doped Tin Oxide Nanocrystals for Thin Film Optoelectronics. *Chem. Mater.* **2013**, *25*, 4901–4907.

(8)  Ederth, J.; Johnsson, P.; Niklasson, G. A.; Hoel, A.; Hultåker, A.; Heszler, P.; Granqvist, C. G.; van Doorn, A. R.; Jongerius, M. J.; Burgard, D. Electrical and Optical Properties of Thin Films Consisting of Tin-Doped Indium Oxide Nanoparticles. *Phys. Rev. B* **2003**, *68*, 155410.

(9)  Lee, J.; Petruska, M. A.; Sun, S. Surface Modification and Assembly of Transparent Indium Tin Oxide Nanocrystals for Enhanced Conductivity. *J. Phys. Chem. C* **2014**, *118*, 12017–12021.

(10)     Kulkarni, A. K.; Schulz, K. H.; Lim, T. S.; Khan, M. Dependence of the Sheet Resistance of Indium-Tin-Oxide Thin Films on Grain Size and Grain Orientation Determined from X-Ray Diffraction Techniques. *Thin Solid Films* **1999**, *345*, 273–277.

(11)     Song, J.; Zeng, H. Transparent Electrodes Printed with Nanocrystal Inks for Flexible Smart Devices. *Angew. Chem. Int. Ed.* 2015, *54*, 9760–9774.

(12)     Guo, X.; Liu, X.; Lin, F.; Li, H.; Fan, Y.; Zhang, N. Highly Conductive Transparent Organic Electrodes with Multilayer Structures for Rigid and Flexible Optoelectronics. *Sci. Rep.* **2015**, *5*, 10569.

(13)     Li, D.; Lai, W.-Y.; Zhang, Y.-Z.; Huang, W. Printable Transparent Conductive Films for Flexible Electronics. *Adv. Mater.* **2018**, *30*, 1704738.

(14)     Guillén, C.; Herrero, J. TCO/Metal/TCO Structures for Energy and Flexible Electronics. *Thin Solid Films* **2011**, *520*, 1–17.

(15)     Lewis, J. Material Challenge for Flexible Organic Devices. *Mater. Today* **2006**, *9*, 38–45.

(16)     Fu, F.; Feurer, T.; Jäger, T.; Avancini, E.; Bissig, B.; Yoon, S.; Buecheler, S.; Tiwari, A. N. Low-Temperature-Processed Efficient Semi-Transparent Planar Perovskite Solar Cells for Bifacial and Tandem Applications. *Nat. Commun.* **2015**, *6*, 8932.

(17)     Werner, J.; Dubuis, G.; Walter, A.; Löper, P.; Moon, S.-J.; Nicolay, S.; Morales-Masis, M.; De Wolf, S.; Niesen, B.; Ballif, C. Sputtered Rear Electrode with Broadband Transparency for Perovskite Solar Cells. *Sol. Energy Mater. Sol. Cells* **2015**, *141*, 407–413.

(18)     Lai, W.-C.; Lin, K.-W.; Guo, T.-F.; Chen, P.; Wang, Y.-T. Conversion Efficiency Improvement of Inverted $CH_3NH_3PbI_3$ Perovskite Solar Cells with Room Temperature Sputtered ZnO by Adding the $C_{60}$ Interlayer. *Appl. Phys. Lett.* **2015**, *107*, 253301.

(19)     Xu, W.; Li, H.; Xu, J.-B.; Wang, L. Recent Advances of Solution-Processed Metal Oxide Thin-Film Transistors. *ACS Appl. Mater. Interfaces* **2018**, *10*, 25878–25901.

(20)     Eslamian, M. Inorganic and Organic Solution-Processed Thin Film Devices. *Nano-Micro Lett.* **2016**, *9*, 3.

(21)     Kim, M.-G.; Kanatzidis, M. G.; Facchetti, A.; Marks, T. J. Low-Temperature Fabrication of High-Performance Metal Oxide Thin-Film Electronics via Combustion Processing. *Nat. Mater.* **2011**, *10*, 382–388.

(22)     Varol, S. F.; Babür, G.; Çankaya, G.; Kölemen, U. Synthesis of Sol–Gel Derived Nano-Crystalline ZnO Thin Films as TCO Window Layer: Effect of Sol Aging and Boron. *RSC Adv.* **2014**, *4*, 56645–56653.

(23)     Kurz, A.; Brakecha, K.; Puetz, J.; Aegerter, M. A. Strategies for Novel Transparent Conducting Sol–Gel Oxide Coatings. *Thin Solid Films* **2006**, *502*, 212–218.

(24)     Winer, I.; Shter, G. E.; Mann-Lahav, M.; Grader, G. S. Effect of Solvents and Stabilizers on Sol–Gel Deposition of Ga-Doped Zinc Oxide TCO Films. *J. Mater. Res.* **2011**, *26*, 1309–1315.

(25)     Koebel, M. M.; Nadargi, D. Y.; Jimenez-Cadena, G.; Romanyuk, Y. E. Transparent, Conducting ATO Thin Films by Epoxide-Initiated Sol–Gel Chemistry: A Highly Versatile Route to Mixed-Metal Oxide Films. *ACS Appl. Mater. Interfaces* **2012**, *4*, 2464–2473.

(26)     Nadarajah, A.; Carnes, M. E.; Kast, M. G.; Johnson, D. W.; Boettcher, S. W. Aqueous Solution Processing of F-Doped $SnO_2$ Transparent Conducting Oxide Films Using a Reactive Tin(II) Hydroxide Nitrate Nanoscale Cluster. *Chem. Mater.* **2013**, *25*, 4080–4087.

(27)     Carnes, M. E.; Knutson, C. C.; Nadarajah, A.; Jackson, M. N.; Oliveri, A. F.; Norelli, K. M.; Crockett, B. M.; Bauers, S. R.; Moreno-Luna, H. A.; Taber, B. N.; et al. Electrochemical Synthesis of Flat-$[Ga_{13-x}In_x(M_3\text{-}OH)_6(\mu\text{-}OH)_{18}(H2O)_{24}(NO3)_{15}]$ Clusters as Aqueous Precursors for Solution-Processed Semiconductors. *J. Mater. Chem. C* **2014**, *2*, 8492–8496.

(28)     Song, J.; Kulinich, S. A.; Li, J.; Liu, Y.; Zeng, H. A General One-Pot Strategy for the Synthesis of High-Performance Transparent-Conducting-Oxide Nanocrystal Inks for All-Solution-Processed Devices. *Angew. Chem. Int. Ed Engl.* **2015**, *54*, 462–466.

(29)     Staller, C. M.; Robinson, Z. L.; Agrawal, A.; Gibbs, S. L.; Greenberg, B. L.; Lounis, S. D.; Kortshagen, U. R.; Milliron, D. J. Tuning Nanocrystal Surface Depletion by Controlling Dopant Distribution as a Route Toward Enhanced Film Conductivity. *Nano Lett.* **2018**, *18*, 2870–2878.

(30)     Hoertz, P. G.; Chen, Z.; Kent, C. A.; Meyer, T. J. Application of High Surface Area Tin-Doped Indium Oxide Nanoparticle Films as Transparent Conducting Electrodes. *Inorg. Chem.* **2010**, *49*, 8179–8181.

(31)     Pham, H. T.; Jeong, H.-D. Non-Monotonic Size Dependence of Electron Mobility in Indium Oxide Nanocrystals Thin Film Transistor. *Bull. Korean Chem. Soc.* **2014**, *35*, 2505–2511.

(32)     Samadi Khoshkhoo, M.; Maiti, S.; Schreiber, F.; Chassé, T.; Scheele, M. Surface Functionalization with Copper Tetraaminophthalocyanine Enables Efficient Charge Transport in Indium Tin Oxide Nanocrystal Thin Films. *ACS Appl. Mater. Interfaces* **2017**, *9*, 14197–14206.

(33)     Yazdani, N.; Bozyigit, D.; Yarema, O.; Yarema, M.; Wood, V. Hole Mobility in Nanocrystal Solids as a Function of Constituent Nanocrystal Size. *J. Phys. Chem. Lett.* **2014**, *5*, 3522–3527.

(34) Scheele, M.; Engel, J. H.; Ferry, V. E.; Hanifi, D.; Liu, Y.; Alivisatos, A. P. Nonmonotonic Size Dependence in the Hole Mobility of Methoxide-Stabilized PbSe Quantum Dot Solids. *ACS Nano* **2013**, *7*, 6774–6781.

(35) Kang, M. S.; Sahu, A.; Norris, D. J.; Frisbie, C. D. Size-Dependent Electrical Transport in CdSe Nanocrystal Thin Films. *Nano Lett.* **2010**, *10*, 3727–3732.

(36) Kang, M. S.; Sahu, A.; Norris, D. J.; Frisbie, C. D. Size- and Temperature-Dependent Charge Transport in PbSe Nanocrystal Thin Films. *Nano Lett.* **2011**, *11*, 3887–3892.

(37) Liu, Y.; Gibbs, M.; Puthussery, J.; Gaik, S.; Ihly, R.; Hillhouse, H. W.; Law, M. Dependence of Carrier Mobility on Nanocrystal Size and Ligand Length in PbSe Nanocrystal Solids. *Nano Lett.* **2010**, *10*, 1960–1969.

(38) Guyot-Sionnest, P. Electrical Transport in Colloidal Quantum Dot Films. *J. Phys. Chem. Lett.* **2012**, *3*, 1169–1175.

(39) Ephraim, J.; Lanigan, D.; Staller, C.; Milliron, D. J.; Thimsen, E. Transparent Conductive Oxide Nanocrystals Coated with Insulators by Atomic Layer Deposition. *Chem. Mater.* **2016**, *28*, 5549–5553.

(40) Chen, Z.; Qin, X.; Zhou, T.; Wu, X.; Shao, S.; Xie, M.; Cui, Z. Ethanolamine-Assisted Synthesis of Size-Controlled Indium Tin Oxide Nanoinks for Low Temperature Solution Deposited Transparent Conductive Films. *J. Mater. Chem. C* **2015**, *3*, 11464–11470.

(41) Garcia, G.; Buonsanti, R.; Runnerstrom, E. L.; Mendelsberg, R. J.; Llordes, A.; Anders, A.; Richardson, T. J.; Milliron, D. J. Dynamically Modulating the Surface Plasmon Resonance of Doped Semiconductor Nanocrystals. *Nano Lett.* **2011**, *11*, 4415–4420.

(42) Lee, J.; Lee, S.; Li, G.; Petruska, M. A.; Paine, D. C.; Sun, S. A Facile Solution-Phase Approach to Transparent and Conducting ITO Nanocrystal Assemblies. *J. Am. Chem. Soc.* **2012**, *134*, 13410–13414.

(43) Ito, D.; Masuko, K.; Weintraub, B. A.; McKenzie, L. C.; Hutchison, J. E. Convenient Preparation of ITO Nanoparticles Inks for Transparent Conductive Thin Films. *J. Nanoparticle Res.* **2012**, *14*, 1274.

(44) Lounis, S. D.; Runnerstrom, E. L.; Bergerud, A.; Nordlund, D.; Milliron, D. J. Influence of Dopant Distribution on the Plasmonic Properties of Indium Tin Oxide Nanocrystals. *J. Am. Chem. Soc.* **2014**, *136*, 7110–7116.

(45) Ba, J.; Fattakhova Rohlfing, D.; Feldhoff, A.; Brezesinski, T.; Djerdj, I.; Wark, M.; Niederberger, M. Nonaqueous Synthesis of Uniform Indium Tin Oxide Nanocrystals and Their Electrical Conductivity in Dependence of the Tin Oxide Concentration. *Chem. Mater.* **2006**, *18*, 2848–2854.

(46) Diroll, B. T.; Gordon, T. R.; Gaulding, E. A.; Klein, D. R.; Paik, T.; Yun, H. J.; Goodwin, E. D.; Damodhar, D.; Kagan, C. R.; Murray, C. B. Synthesis of N-Type Plasmonic Oxide Nanocrystals and the Optical and Electrical Characterization of Their Transparent Conducting Films. *Chem. Mater.* **2014**, *26*, 4579–4588.

(47) Bühler, G.; Thölmann, D.; Feldmann, C. One-Pot Synthesis of Highly Conductive Indium Tin Oxide Nanocrystals. *Adv. Mater.* **2007**, *19*, 2224–2227.

(48) Yarema, M.; Pichler, S.; Kriegner, D.; Stangl, J.; Yarema, O.; Kirchschlager, R.; Tollabimazraehno, S.; Humer, M.; Häringer, D.; Kohl, M.; et al. From Highly Monodisperse Indium and Indium Tin Colloidal Nanocrystals to Self-Assembled Indium Tin Oxide Nanoelectrodes. *ACS Nano* **2012**, *6*, 4113–4121.

(49) Crockett, B. M.; Jansons, A. W.; Koskela, K. M.; Johnson, D. W.; Hutchison, J. E. Radial Dopant Placement for Tuning Plasmonic Properties in Metal Oxide Nanocrystals. *ACS Nano* **2017**, *11*, 7719–7728.

(50) Tandon, B.; Yadav, A.; Khurana, D.; Reddy, P.; Santra, P. K.; Nag, A. Size-Induced Enhancement of Carrier Density, LSPR Quality Factor, and Carrier Mobility in Cr–Sn Doped $In_2O_3$ Nanocrystals. *Chem. Mater.* **2017**, *29*, 9360–9368.

(51) Zhou, D.; Wang, P.; Roy, C. R.; Barnes, M. D.; Kittilstved, K. R. Direct Evidence of Surface Charges in N-Type Al-Doped ZnO. *J. Phys. Chem. C* **2018**, *122*, 18596–18602.

(52) Matsui, H.; Hasebe, T.; Hasuike, N.; Tabata, H. Plasmonic Heat Shielding in the Infrared Range Using Oxide Semiconductor Nanoparticles Based on Sn-Doped In2O3: Effect of Size and Interparticle Gap. *ACS Appl. Nano Mater.* **2018**, *1*, 1853–1862.

(53) Runnerstrom, E. L.; Bergerud, A.; Agrawal, A.; Johns, R. W.; Dahlman, C. J.; Singh, A.; Selbach, S. M.; Milliron, D. J. Defect Engineering in Plasmonic Metal Oxide Nanocrystals. *Nano Lett.* **2016**, *16*, 3390–3398.

(54) Mehra, S.; Bergerud, A.; Milliron, D. J.; Chan, E. M.; Salleo, A. Core/Shell Approach to Dopant Incorporation and Shape Control in Colloidal Zinc Oxide Nanorods. *Chem. Mater.* **2016**, *28*, 3454–3461.

(55) Agrawal, A.; Singh, A.; Yazdi, S.; Singh, A.; Ong, G. K.; Bustillo, K.; Johns, R. W.; Ringe, E.; Milliron, D. J. Resonant Coupling between Molecular Vibrations and Localized Surface Plasmon Resonance of Faceted Metal Oxide Nanocrystals. *Nano Lett.* **2017**, *17*, 2611–2620.

(56) Jansons, A. W.; Hutchison, J. E. Continuous Growth of Metal Oxide Nanocrystals: Enhanced Control of Nanocrystal Size and Radial Dopant Distribution. *ACS Nano*, **2016**, *10*, 6942–6951.

(57)     Ito, D.; Yokohama, S.; Zaikova, T.; Masuko, K.; Hutchison, J. E. Synthesis of Ligand-Stabilized Metal Oxide Nanocrystals and Epitaxial Core/Shell Nanocrystals via a Lower-Temperature Esterification Process. *ACS Nano*, **2014**, *8*, 64–75.

(58)     Kanehara, M.; Koike, H.; Yoshinaga, T.; Teranishi, T. Indium Tin Oxide Nanoparticles with Compositionally Tunable Surface Plasmon Resonance Frequencies in the Near-IR Region. *J. Am. Chem. Soc.* **2009**, *131*, 17736–17737.

(59)     Choi, S.-I.; Nam, K. M.; Park, B. K.; Seo, W. S.; Park, J. T. Preparation and Optical Properties of Colloidal, Monodisperse, and Highly Crystalline ITO Nanoparticles. *Chem. Mater.* **2008**, *20*, 2609–2611.

(60)     Gilstrap, R. A.; Capozzi, C. J.; Carson, C. G.; Gerhardt, R. A.; Summers, C. J. Synthesis of a Nonagglomerated Indium Tin Oxide Nanoparticle Dispersion. *Adv. Mater.* **2008**, *20*, 4163–4166.

(61)     Cooper, S. R.; Plummer, L. K.; Cosby, A. G.; Lenox, P.; Jander, A.; Dhagat, P.; Hutchison, J. E. Insights into the Magnetic Properties of Sub-10 Nm Iron Oxide Nanocrystals through the Use of a Continuous Growth Synthesis. *Chem. Mater.* **2018**, *30*, 6053–6062.

(62)     Jansons, A. W.; Plummer, L. K.; Hutchison, J. E. Living Nanocrystals. *Chem. Mater.* **2017**, *29*, 5415–5425.

(63)     Zandi, O.; Agrawal, A.; Shearer, A. B.; Reimnitz, L. C.; Dahlman, C. J.; Staller, C. M.; Milliron, D. J. Impacts of Surface Depletion on the Plasmonic Properties of Doped Semiconductor Nanocrystals. *Nat. Mater.* **2018**, *17*, 710.

(64)     Agrawal, A.; Johns, R. W.; Milliron, D. J. Control of Localized Surface Plasmon Resonances in Metal Oxide Nanocrystals. *Annu. Rev. Mater. Res.* **2017**, *47*, 1–31.

(65)     Kriegel, I.; Scotognella, F.; Manna, L. Plasmonic Doped Semiconductor Nanocrystals: Properties, Fabrication, Applications and Perspectives. *Phys. Rep.* **2017**, *674*, 1–52.

(66)     Agrawal, A.; Cho, S. H.; Zandi, O.; Ghosh, S.; Johns, R. W.; Milliron, D. J. Localized Surface Plasmon Resonance in Semiconductor Nanocrystals. *Chem. Rev.* **2018**, *118*, 3121–3207.

(67)     Zarghami, M. H.; Liu, Y.; Gibbs, M.; Gebremichael, E.; Webster, C.; Law, M. P-Type PbSe and PbS Quantum Dot Solids Prepared with Short-Chain Acids and Diacids. *ACS Nano* **2010**, *4*, 2475–2485.

(68)     Kim, J.-Y.; Kotov, N. A. Charge Transport Dilemma of Solution-Processed Nanomaterials. *Chem. Mater.* **2014**, *26*, 134–152.

(69)     Beloborodov, I. S.; Lopatin, A. V.; Vinokur, V. M.; Efetov, K. B. Granular Electronic Systems. *Rev. Mod. Phys.* **2007**, *79*, 469–518.

(70)   Grisolia, J.; Decorde, N.; Gauvin, M.; Sangeetha, N. M.; Viallet, B.; Ressier, L. Electron Transport within Transparent Assemblies of Tin-Doped Indium Oxide Colloidal Nanocrystals. *Nanotechnology* **2015**, *26*, 335702.

(71)   Terril, R. H.; Postlethwaite, T. A.; Chen, C.; Poon, C.; Terzis, A.; Chen, A.; Hutchison, J. E.; Clark, M. R.; Wignal, G.; Londono, J. D.; Superfine, R.; Falvo, M.; Johnson Jr., C. S.; Samulski, E. T.; Murray, R. W. Monolayers in Three Dimensions: NMR, SAXS, Thermal, and Electron Hopping Studies of Alkanethiol Stabilized Gold Clusters. *J. Am. Chem. Soc.* **1995**, *117*, 12537–12548.

(72)   Moreira, H.; Yu, Q.; Nadal, B.; Bresson, B.; Rosticher, M.; Lequeux, N.; Zimmers, A.; Aubin, H. Electron Cotunneling Transport in Gold Nanocrystal Arrays. *Phys. Rev. Lett.* **2011**, *107*, 176803.

(73)   Wu, W.; Brongersma, S. H.; Van Hove, M.; Maex, K. Influence of Surface and Grain-Boundary Scattering on the Resistivity of Copper in Reduced Dimensions. *Appl. Phys. Lett.* **2004**, *84*, 2838–2840.

(74)   Ghosh, S.; Sarkar, A.; Chaudhuri, S.; Pal, A. K. Grain Boundary Scattering in Aluminium-Doped ZnO Films. *Thin Solid Films* **1991**, *205*, 64–68..

(75)   Mayadas, A. F.; Shatzkes, M. Electrical-Resistivity Model for Polycrystalline Films: The Case of Arbitrary Reflection at External Surfaces. *Phys. Rev. B* **1970**, *1*, 1382–1389.

(76)   Deschacht, D.; Boyer, A.; Groubert, E. Effect of Grain Boundary Scattering on the Electrical Conductivity of Antimony Films. *Thin Solid Films* **1980**, *70*, 311–317.

(77)   Torquato, S.; Truskett, T. M.; Debenedetti, P. G. Is Random Close Packing of Spheres Well Defined? *Phys. Rev. Lett.* **2000**, *84*, 2064–2067.

(78)   Yang, A.; Miller, C. T.; Turcoliver, L. D. Simulation of Correlated and Uncorrelated Packing of Random Size Spheres. *Phys. Rev. E* **1996**, *53*, 1516–1524.

(79)   Bezrukov, A.; Bargieł, M.; Stoyan, D. Statistical Analysis of Simulated Random Packings of Spheres. *Part. Part. Syst. Charact.* **2002**, *19*, 111–118.

(80)   Scott, G. D.; Kilgour, D. M. The Density of Random Close Packing of Spheres. *J. Phys. Appl. Phys.* **1969**, *2*, 863–866.

(81)   Lee, Y.; Noh, S.; Kim, M.-S.; Kong, H. J.; Im, K.; Kwon, O. S.; Kim, S.; Yoon, H. The Effect of Nanoparticle Packing on Capacitive Electrode Performance. *Nanoscale* **2016**, *8*, 11940–11948.

(82)   Illavsky, J.; Jemian, P. R. Irena: tool suite for modeling and analysis of small-angle scattering. *J. Appl. Cryst.* **2009**, *42*, 347–353

## Chapter IV

(1)     Dieringer, J. A.; Wustholz, K. L.; Masiello, D. J.; Camden, J. P.; Kleinman, S. L.; Schatz, G. C.; Van Duyne, R. P. Surface-Enhanced Raman Excitation Spectroscopy of a Single Rhodamine 6G Molecule. *J. Am. Chem. Soc.* **2009**, *131*, 849–854.

(2)     Nie, S.; Emory, S. R. Probing Single Molecules and Single Nanoparticles by Surface-Enhanced Raman Scattering. *Science* **1997**, *275*, 1102–1106.

(3)     Rosman, C.; Prasad, J.; Neiser, A.; Henkel, A.; Edgar, J.; Sönnichsen, C. Multiplexed Plasmon Sensor for Rapid Label-Free Analyte Detection. *Nano Lett.* **2013**, *13*, 3243–3247.

(4)     Larsson, E. M.; Langhammer, C.; Zorić, I.; Kasemo, B. Nanoplasmonic Probes of Catalytic Reactions. *Science* **2009**, *326*, 1091–1094.

(5)     Mendelsberg, R. J.; McBride, P. M.; Duong, J. T.; Bailey, M. J.; Llordes, A.; Milliron, D. J.; Helms, B. A. Dispersible Plasmonic Doped Metal Oxide Nanocrystal Sensors That Optically Track Redox Reactions in Aqueous Media with Single-Electron Sensitivity. *Adv. Opt. Mater.* **2015**, *3*, 1293–1300.

(6)     Diroll, B. T.; Gordon, T. R.; Gaulding, E. A.; Klein, D. R.; Paik, T.; Yun, H. J.; Goodwin, E. D.; Damodhar, D.; Kagan, C. R.; Murray, C. B. Synthesis of N-Type Plasmonic Oxide Nanocrystals and the Optical and Electrical Characterization of Their Transparent Conducting Films. *Chem. Mater.* **2014**, *26*, 4579–4588.

(7)     Ito, D.; Masuko, K.; Weintraub, B. A.; McKenzie, L. C.; Hutchison, J. E. Convenient Preparation of ITO Nanoparticles Inks for Transparent Conductive Thin Films. *J. Nanoparticle Res.* **2012**, *14*, 1–7.

(8)     Loo, C.; Lowery, A.; Halas, N.; West, J.; Drezek, R. Immunotargeted Nanoshells for Integrated Cancer Imaging and Therapy. *Nano Lett.* **2005**, *5*, 709–711.

(9)     Huang, X.; El-Sayed, I. H.; Qian, W.; El-Sayed, M. A. Cancer Cell Imaging and Photothermal Therapy in the Near-Infrared Region by Using Gold Nanorods. *J. Am. Chem. Soc.* **2006**, *128*, 2115–2120.

(10)    Kumar, A.; Kim, S.; Nam, J.-M. Plasmonically Engineered Nanoprobes for Biomedical Applications. *J. Am. Chem. Soc.* **2016**, *138*, 14509–14525.

(11)    Kovalenko, M. V.; Manna, L.; Cabot, A.; Hens, Z.; Talapin, D. V.; Kagan, C. R.; Klimov, V. I.; Rogach, A. L.; Reiss, P.; Milliron, D. J. Guyot-Sionnnest, P.; Konstantanos, G.; Parak, W. J.; Hyeon, T.; Korgel, B. A.; Murray, B. M.; Heiss, W. Prospects of Nanoscience with Nanocrystals. *ACS Nano* **2015**, *9*, 1012–1057.

(12)    Faucheaux, J. A.; Stanton, A. L. D.; Jain, P. K. Plasmon Resonances of Semiconductor Nanocrystals: Physical Principles and New Opportunities. *J. Phys. Chem. Lett.* **2014**, *5*, 976–985.

(13)     Lounis, S. D.; Runnerstrom, E. L.; Llordés, A.; Milliron, D. J. Defect Chemistry and Plasmon Physics of Colloidal Metal Oxide Nanocrystals. *J. Phys. Chem. Lett.* **2014**, *5*, 1564–1574.

(14)     Agrawal, A.; Johns, R. W.; Milliron, D. J. Control of Localized Surface Plasmon Resonances in Metal Oxide Nanocrystals. *Annu. Rev. Mater. Res.* **2017**, *47*, in press.

(15)     Kriegel, I.; Scotognella, F.; Manna, L. Plasmonic Doped Semiconductor Nanocrystals: Properties, Fabrication, Applications and Perspectives. *Plasmonic Doped Semicond. Nanocrystals Prop. Fabr. Appl. Perspect.* **2017**, *674*, 1–52.

(16)     Kanehara, M.; Koike, H.; Yoshinaga, T.; Teranishi, T. Indium Tin Oxide Nanoparticles with Compositionally Tunable Surface Plasmon Resonance Frequencies in the Near-IR Region. *J. Am. Chem. Soc.* **2009**, *131*, 17736–17737.

(17)     Gilstrap, R. A.; Capozzi, C. J.; Carson, C. G.; Gerhardt, R. A.; Summers, C. J. Synthesis of a Nonagglomerated Indium Tin Oxide Nanoparticle Dispersion. *Adv. Mater.* **2008**, *20*, 4163–4166.

(18)     Choi, S.-I.; Nam, K. M.; Park, B. K.; Seo, W. S.; Park, J. T. Preparation and Optical Properties of Colloidal, Monodisperse, and Highly Crystalline ITO Nanoparticles. *Chem. Mater.* **2008**, *20*, 2609–2611.

(19)     Farvid, S. S.; Dave, N.; Wang, T.; Radovanovic, P. V. Dopant-Induced Manipulation of the Growth and Structural Metastability of Colloidal Indium Oxide Nanocrystals. *J. Phys. Chem. C* **2009**, *113*, 15928–15933.

(20)     Lee, J.; Lee, S.; Li, G.; Petruska, M. A.; Paine, D. C.; Sun, S. A Facile Solution-Phase Approach to Transparent and Conducting ITO Nanocrystal Assemblies. *J. Am. Chem. Soc.* **2012**, *134*, 13410–13414.

(21)     Runnerstrom, E. L.; Bergerud, A.; Agrawal, A.; Johns, R. W.; Dahlman, C. J.; Singh, A.; Selbach, S. M.; Milliron, D. J. Defect Engineering in Plasmonic Metal Oxide Nanocrystals. *Nano Lett.* **2016**, *16*, 3390–3398.

(22)     Mehra, S.; Bergerud, A.; Milliron, D. J.; Chan, E. M.; Salleo, A. Core/Shell Approach to Dopant Incorporation and Shape Control in Colloidal Zinc Oxide Nanorods. *Chem. Mater.* **2016**, *28*, 3454–3461.

(23)     Garcia, G.; Buonsanti, R.; Runnerstrom, E. L.; Mendelsberg, R. J.; Llordes, A.; Anders, A.; Richardson, T. J.; Milliron, D. J. Dynamically Modulating the Surface Plasmon Resonance of Doped Semiconductor Nanocrystals. *Nano Lett.* **2011**, *11*, 4415–4420.

(24)     Della Gaspera, E.; Chesman, A. S. R.; van Embden, J.; Jasieniak, J. J. Non-Injection Synthesis of Doped Zinc Oxide Plasmonic Nanocrystals. *ACS Nano* **2014**, *8*, 9154–9163.

(25)  Gordon, T. R.; Paik, T.; Klein, D. R.; Naik, G. V.; Caglayan, H.; Boltasseva, A.; Murray, C. B. Shape-Dependent Plasmonic Response and Directed Self-Assembly in a New Semiconductor Building Block, Indium-Doped Cadmium Oxide (ICO). *Nano Lett.* **2013**, *13*, 2857–2863.

(26)  Ye, X.; Reifsnyder Hickey, D.; Fei, J.; Diroll, B. T.; Paik, T.; Chen, J.; Murray, C. B. Seeded Growth of Metal-Doped Plasmonic Oxide Heterodimer Nanocrystals and Their Chemical Transformation. *J. Am. Chem. Soc.* **2014**, *136*, 5106–5115.

(27)  De Trizio, L.; Buonsanti, R.; Schimpf, A. M.; Llordes, A.; Gamelin, D. R.; Simonutti, R.; Milliron, D. J. Nb-Doped Colloidal $TiO_2$ Nanocrystals with Tunable Infrared Absorption. *Chem. Mater.* **2013**, *25*, 3383–3390.

(28)  Fang, H.; Hegde, M.; Yin, P.; Radovanovic, P. V. Tuning Plasmon Resonance of $In_2O_3$ Nanocrystals throughout the Mid-Infrared Region by Competition between Electron Activation and Trapping. *Chem. Mater.* **2017**, *29*, 4970-4979.

(29)  Buonsanti, R.; Milliron, D. J. Chemistry of Doped Colloidal Nanocrystals. *Chem. Mater.* **2013**, *25*, 1305–1317.

(30)  Johns, R. W.; Bechtel, H. A.; Runnerstrom, E. L.; Agrawal, A.; Lounis, S. D.; Milliron, D. J. Direct Observation of Narrow Mid-Infrared Plasmon Linewidths of Single Metal Oxide Nanocrystals. *Nat. Commun.* **2016**, *7*, 11583.

(31)  Lounis, S. D.; Runnerstrom, E. L.; Bergerud, A.; Nordlund, D.; Milliron, D. J. Influence of Dopant Distribution on the Plasmonic Properties of Indium Tin Oxide Nanocrystals. *J. Am. Chem. Soc.* **2014**, *136*, 7110–7116.

(32)  Ito, D.; Yokoyama, S.; Zaikova, T.; Masuko, K.; Hutchison, J. E. Synthesis of Ligand-Stabilized Metal Oxide Nanocrystals and Epitaxial Core/Shell Nanocrystals *via* a Lower-Temperature Esterification Process. *ACS Nano* **2014**, *8*, 64–75.

(33)  Jansons, A. W.; Hutchison, J. E. Continuous Growth of Metal Oxide Nanocrystals: Enhanced Control of Nanocrystal Size and Radial Dopant Distribution. *ACS Nano* **2016**, *10*, 6942–6951.

(34)  Jansons, A. W.; Plummer, L. K.; Hutchison, J. E. Living Nanocrystals. *Chem. Mater.* **2017**, *29* (13), 5415–5425.

(35)  Tanuma, S.; Powell, C. J.; Penn, D. R. Calculations of Electron Inelastic Mean Free Paths. V. Data for 14 Organic Compounds over the 50–2000 eV Range. *Surf. Interface Anal.* **1994**, *21*, 165–176.

(36)  Veamatahau, A.; Jiang, B.; Seifert, T.; Makuta, S.; Latham, K.; Kanehara, M.; Teranishi, T.; Tachibana, Y. Origin of Surface Trap States in CdS Quantum Dots: Relationship between Size Dependent Photoluminescence and Sulfur Vacancy Trap States. *Phys. Chem. Chem. Phys.* **2015**, *17*, 2850–2858.

(37)     Oh, S. J.; Straus, D. B.; Zhao, T.; Choi, J.-H.; Lee, S.-W.; Gaulding, E. A.; Murray, C. B.; Kagan, C. R. Engineering the Surface Chemistry of Lead Chalcogenide Nanocrystal Solids to Enhance Carrier Mobility and Lifetime in Optoelectronic Devices. *Chem. Commun.* **2017**, *53*, 728–731.

(38)     Houtepen, A. J.; Hens, Z.; Owen, J. S.; Infante, I. On the Origin of Surface Traps in Colloidal II–VI Semiconductor Nanocrystals. *Chem. Mater.* **2017**, *29*, 752–761.

(39)     Boles, M. A.; Ling, D.; Hyeon, T.; Talapin, D. V. The Surface Science of Nanocrystals. *Nat Mater* **2016**, *15*, 141–153.

(40)     Scotognella, F.; Della Valle, G.; Srimath Kandada, A. R.; Dorfs, D.; Zavelani-Rossi, M.; Conforti, M.; Miszta, K.; Comin, A.; Korobchevskaya, K.; Lanzani, G.; Manna, L.; Tassone, F. Plasmon Dynamics in Colloidal $Cu_2$–xSe Nanocrystals. *Nano Lett.* **2011**, *11*, 4711–4717.

(41)     Dorfs, D.; Härtling, T.; Miszta, K.; Bigall, N. C.; Kim, M. R.; Genovese, A.; Falqui, A.; Povia, M.; Manna, L. Reversible Tunability of the Near-Infrared Valence Band Plasmon Resonance in $Cu_2$–xSe Nanocrystals. *J. Am. Chem. Soc.* **2011**, *133*, 11175–11180.

(42)     Manthiram, K.; Alivisatos, A. P. Tunable Localized Surface Plasmon Resonances in Tungsten Oxide Nanocrystals. *J. Am. Chem. Soc.* **2012**, *134*, 3995–3998.

(43)     Hamberg, I.; Granqvist, C. G. Evaporated Sn-doped $In_2O_3$ Films: Basic Optical Properties and Applications to Energy-efficient Windows. *J. Appl. Phys.* **1986**, *60*, R123–R160.

(44)     Hamberg, I.; Granqvist, C. G. Optical Properties of Transparent and Heat-reflecting Indium Tin Oxide Films: The Role of Ionized Impurity Scattering. *Appl. Phys. Lett.* **1984**, *44*, 721–723.

(45)     Agrawal, A.; Singh, A.; Yazdi, S.; Singh, A.; Ong, G. K.; Bustillo, K.; Johns, R. W.; Ringe, E.; Milliron, D. J. Resonant Coupling between Molecular Vibrations and Localized Surface Plasmon Resonance of Faceted Metal Oxide Nanocrystals. *Nano Lett.* **2017**, *17*, 2611–2620.

(46)     Link, S.; El-Sayed, M. A. Spectral Properties and Relaxation Dynamics of Surface Plasmon Electronic Oscillations in Gold and Silver Nanodots and Nanorods. *J. Phys. Chem. B* **1999**, *103*, 8410–8426.

(47)     Fan, J. C. C.; Goodenough, J. B. X-ray Photoemission Spectroscopy Studies of Sn-doped Indium-oxide Films. *J. Appl. Phys.* **1977**, *48*, 3524–3531.

(48)     Frank, G.; Köstlin, H. Electrical Properties and Defect Model of Tin-Doped Indium Oxide Layers. *Appl. Phys. A* **1982**, *27*, 197–206.

(49)     Cox, P. A.; Flavell, W. R.; Egdell, R. G. Solid-State and Surface Chemistry of Sn-Doped $In_2O_3$ Ceramics. *J. Solid State Chem.* **1987**, *68*, 340–350.

(50)     Gassenbauer, Y.; Schafranek, R.; Klein, A.; Zafeiratos, S.; Hävecker, M.; Knop-Gericke, A.; Schlögl, R. Surface States, Surface Potentials, and Segregation at Surfaces of Tin-Doped $In_2O_3$. *Phys. Rev. B* **2006**, *73*, 245312.

(51)     Liu, N.; Tang, M. L.; Hentschel, M.; Giessen, H.; Alivisatos, A. P. Nanoantenna-Enhanced Gas Sensing in a Single Tailored Nanofocus. *Nat Mater* **2011**, *10*, 631–636.

(52)     Willets, K. A.; Duyne, R. P. V. Localized Surface Plasmon Resonance Spectroscopy and Sensing. *Annu. Rev. Phys. Chem.* **2007**, *58*, 267–297.

(53)     Elghanian, R.; Storhoff, J. J.; Mucic, R. C.; Letsinger, R. L.; Mirkin, C. A. Selective Colorimetric Detection of Polynucleotides Based on the Distance-Dependent Optical Properties of Gold Nanoparticles. *Science* **1997**, *277*, 1078–1081.

(54)     Llordes, A.; Garcia, G.; Gazquez, J.; Milliron, D. J. Tunable near-Infrared and Visible-Light Transmittance in Nanocrystal-in-Glass Composites. *Nature* **2013**, *500*, 323–326.

(55)     Llordes, A.; Wang, Y.; Fernandez-Martinez, A.; Xiao, P.; Lee, T.; Poulain, A.; Zandi, O.; Saez Cabezas, C. A.; Henkelman, G.; Milliron, D. J. Linear Topology in Amorphous Metal Oxide Electrochromic Networks Obtained *via* Low-Temperature Solution Processing. *Nat Mater* **2016**, *15*, 1267–1273.

(56)     Garcia, G.; Buonsanti, R.; Llordes, A.; Runnerstrom, E. L.; Bergerud, A.; Milliron, D. J. Near-Infrared Spectrally Selective Plasmonic Electrochromic Thin Films. *Adv. Opt. Mater.* **2013**, *1*, 215–220.

(57)     Ilavsky, J.; Jemian, P. R. Irena: Tool Suite for Modeling and Analysis of Small-Angle Scattering. *J. Appl. Crystallogr.* **2009**, *42*, 347–353.